# STUDY OF THE FERMI SURFACE OF ALKALI-METAL GRAPHITE INTERCALATION COMPOUNDS USING THE SHUBNIKOV-DE HAAS MEASUREMENTS

by

Mansour Shayegan

S.B., MASSACHUSETTS INSTITUTE OF TECHNOLOGY
(1979)

SUBMITTED IN PARTIAL FULFILLMENT OF THE
REQUIREMENTS FOR THE DEGREES OF
MASTER OF SCIENCE AND ELECTRICAL ENGINEER

at the

MASSACHUSETTS INSTITUTE OF TECHNOLOGY

June, 1981



Signature redacted

Signature of Author _____
Department of Electrical Engineering and Computer Science, May 8, 1981



Signature redacted

Certified by _____
Professor Mildred S. Dresselhaus, Thesis Supervisor

Signature redacted

Accepted by _____
Chairman, Departmental Committee on Graduate Students

# STUDY OF THE FERMI SURFACE OF ALKALI-METAL GRAPHITE INTERCALATION COMPOUNDS USING THE SHUBNIKOV-DE HAAS MEASUREMENTS

by

MANSOUR SHAYEGAN

Submitted to the Department of Electrical Engineering and Computer Science on May 8, 1981 in partial fulfillment of the requirements for the Degrees of Master of Science and Electrical Engineer

## ABSTRACT

Measurements of the electrical resistivity $\rho$ as a function of the magnetic field $\vec{H}$ (up to $\sim$15 Tesla) have been carried out on well-characterized (single stage) encapsulated potassium and rubidium graphite intercalation compounds. From the periodic oscillatory behavior of $\rho$ vs $H^{-1}$ (the Shubnikov-de Haas (SdH) effect), the extremal cross-sectional areas of the Fermi surface (FS) perpendicular to $\vec{H}$ have been determined for these materials.

Possible shapes of the FS are inferred from the dependence of the FS cross sections (SdH frequencies) on the angle between the c-axis of the sample and $\vec{H}$. The temperature dependence ($1.4 \lesssim T \lesssim 25°K$) of the amplitudes of the SdH oscillations has been studied to find cyclotron effective masses for specific FS cross sections.

The stage- and intercalant-dependent experimental results are interpreted in terms of two simple phenomenological energy band models based on the $\pi$-bands of pristine graphite and the c-axis zone folding technique. The good agreement between the experimental and predicted effective masses and the FS cross sections is an indication of the validity of the models.

Thesis Supervisor: Professor Mildred S. Dresselhaus

Title: Abby Rockefeller Mauzé Professor of Electrical Engineering and Director of the Center for Material Science and Engineering

## Acknowledgements

I wish to thank my thesis supervisors, Dr. Gene Dresselhaus and Professor Mildred S. Dresselhaus, for their invaluable guidance and encouragement in all phases of this project and the preparation of the thesis report. Their devoted interest in the physical and emotional, as well as the intellectual well being of their students, makes working with them an unforgettably enjoyable experience.

It has been a great joy for me to work with and have the friendship of Dr. Steve Y. Leung; he has been my great teacher as well as my close friend.

I am indebted to Dr. C. Underhill for his extensive help and guidance in the preparation of the samples. My special thanks are due to N. Kambe and F. Hakimi for their help in familiarizing me with the Magnet Lab and their assistance during the initial experimental runs.

The technical assistance provided by Dr. Bruce Brandt and Dr. Larry Rubin of the National Magnet Laboratory is greatly appreciated. I am also specially thankful to Don Nelson for his invaluable instruction in using the computer facilities at the Magnet Lab. He has always been my great savior in dealing with computer problems. Paul Dresselhaus' assistance in the course of the magnet runs and data analyses has been very useful.

Acknowledgements, continued

I am grateful to all the members of our research group, especially B. Elman, H. Mazurel, T. Krapchev, C. Lowe, I Howard, and T. Chieu; their discussions and friendliness were most beneficial to me.

All my love and respect is for my family and Anna, for their understanding and encouragement during the many frustrating moments of this project.

# TABLE OF CONTENTS

## LIST OF FIGURES

List of Figures (continued)

List of Figures (continued)

List of Figures (continued)



List of Tables

List of Tables, continued

# I. INTRODUCTION

Graphite intercalation compounds (GIC) have been the subject of much current research and interest. These compounds are formed by the insertion of atomic or molecular layers of certain chemical species (the intercalant) between the layers of the host graphite and forming an ordered structure. The staging phenomenon which refers to the periodicity in the stacking of the graphite and the intercalate layers is the most important and interesting structural feature of the GIC. The stage index n denotes the number of contiguous graphitic layers between two nearest intercalant layers. Among the very interesting and curious properties of the GIC, in addition to their highly ordered structure, are: (1) the large number ( > 100 ) and variety of the reagents that react with graphite and form the intercalation compounds, and (2) the high degree of anisotropy in their structural and electronic properties [1,2] (also see Chapter II).

A great deal of work has been done on the structural and electronic properties of GIC [1,2]. Among the many techniques used to study these compounds are: (1) X-ray, electron-, and neutron-diffraction techniques for the staging and in-plane ordering, (2) Raman and infrared spectroscopy in addition to inelastic neutron scattering experiments for the lattice mode properties, and (3) a vast number of experiments such as conductivity, Hall effect, magnetoresistance, electron spectroscopy, magnetooptical and quantum oscillatory measurements to investigate their electronic properties.

The aim of this thesis project was to obtain accurate and reliable information about the electronic structure of these materials using the Shubnikov-de Haas technique, and to use the available energy band models to

interpret the experimental data. Needless to say, once reliable experimental data are available, they can be used to evaluate, contrast and improve the theoretical energy-band models.

A very important piece of information about a solid, and one which relates directly to its energy-band structure, is its Fermi surface (FS). The experimental techniques which provide information about the FS most directly are those which are based on the quantum oscillatory (QO) phenomena and on the oscillatory behavior in reciprocal magnetic field of several properties of the solid. These oscillatory phenomena are normally observed at high magnetic fields and low temperatures, and are closely related to the FS. The QO effects can be observed in the magnetic susceptibility (de Haas-van Alphen or dHvA effect), the electrical conductivity (Shubnikov-de Haas or SdH effect), the temperature of an isolated sample under adiabatic conditions (magnetothermal effect), and several other properties of a solid (with metallic properties).

The frequency(ies) of the periodic oscillations (as a function of inverse magnetic field) in the above properties is/are directly related to the extremal cross-sectional area(s) of the FS (perpendicular to the direction of the applied field; see Section 2.5 for a discussion of the SdH effect.) These frequencies will be referred to as the "SdH frequencies" in this thesis report. The SdH effect was chosen in this project as the means to study the FS of GIC, since it requires the simplest experimental setup. The high field facilities available at the Francis Bitter National Magnet Laboratory, however, were essential for the performance of our experiments and our measurements were carried out to $\sim$15T.

At the time this project was started, there were very few materials

on which the FS experiments had been performed. The first report on the observation of QO effects on GIC was made by Bender and Young in 1971 [3,4]. They performed the SdH experiment on dilute graphite-$Br_2$ samples that were not carefully characterized. Not much work was done in this field until 1978. From that date until now, experiments based on QO phenomena have been performed on a great number of graphite compounds of different intercalants and stages. Some of this work has been done on well characterized samples. Among the intercalants on which the QO measurements have been performed are: K [5-8], Rb [8], $FeCl_3$ and $PdCl_2$ [9], $SbCl_5$ [10], $AsF_5$ [11,1]], $HNO_3$ [13], and $Br_2$ [3-5, 14]. In most of these reports the number of observed SdH frequencies (FS cross sections) and also their magnitudes are considerably greater than for pristine graphite. The large increase in the FS cross sections is generally attributed to the transfer of charge (electrons/holes for donor/acceptor compounds) from the intercalant to the graphite layers , thus swelling the FS (electron/hole pockets). The number of the SdH (or dHvA) frequencies and their stage dependence has been a matter of controversy, and still is.

The reports that indicate a stage dependence of the FS [5-8,11-13] also report that there are a small number of SdH frequencies for low-stage compounds ($n$ = 1,2) and that this number increases as the stage index is increased. On the other hand, there have been reports indicating stage-independent SdH frequencies. Such reports have been made especially for the acceptor compounds [3,9,14]. A large number of SdH frequencies have also been found by these authors, although in this case, many of the observed frequencies are identified as harmonics, or are associated with magentic breakdown phenomena.

In this thesis project, the SdH experiment was performed on alkali metal GIC. Despite their instability in the presence of air and moisture, these materials were chosen because they are structurally among the simplest and best known of GIC, and because it is possible to grow well characterized and single-stage samples of K and Rb-graphite over a large range of stage index [15]. The K-GIC (of low stage) are also the compounds for which first principles band calculations have been performed [16-18]. Our experiments were carried out on single-stage samples of K-GIC (stages 4,5,8) and Rb-GIC (stages 2,3,5,8) and some other nearly single-stage K and Rb samples. These compounds were chosen so that our experiment complements the work of other authors [5-7] who have done the SdH experiment on K-GIC of stages 1,3,4. Our results for the K-stage-4 compound are in fair agreement with results reported by Tanuma et al [5] (Chapter V, Table 5.4). Both our results and those of References 5-7 support a stage-dependent FS. These results will be interpreted in Chapter VI by using two phenomenological energy-band models (explained in Chapter II) which do predict stage-dependent Fermi surfaces.

The actual procedure in carrying out this study followed closely the order in which the chapters (III-VI) are presented. The work done included sample preparation and characterization (Chapter III), sample handling and the SdH experiments (Chapter IV), data analysis (Chapters IV and V) and finally the interpretation of the FS results (Chapter VI). The emphasis in this work was not on performing the SdH experiment on a large number of samples (although to ensure reliability and consistency, a fair number of samples was studied), but rather on studying one compound thoroughly (K-stage-5). Much attention was paid to the quality of the

samples studied and their stage fidelity (using X-ray techniques) before and after the SdH experiment. Encapsulation was used to protect the samples from air and moisture. In subsequent chapters, different stages of the project will be discussed in detail. Here in Fig. 1.1, a flow chart illustrating the highlights of each step of the project is presented.

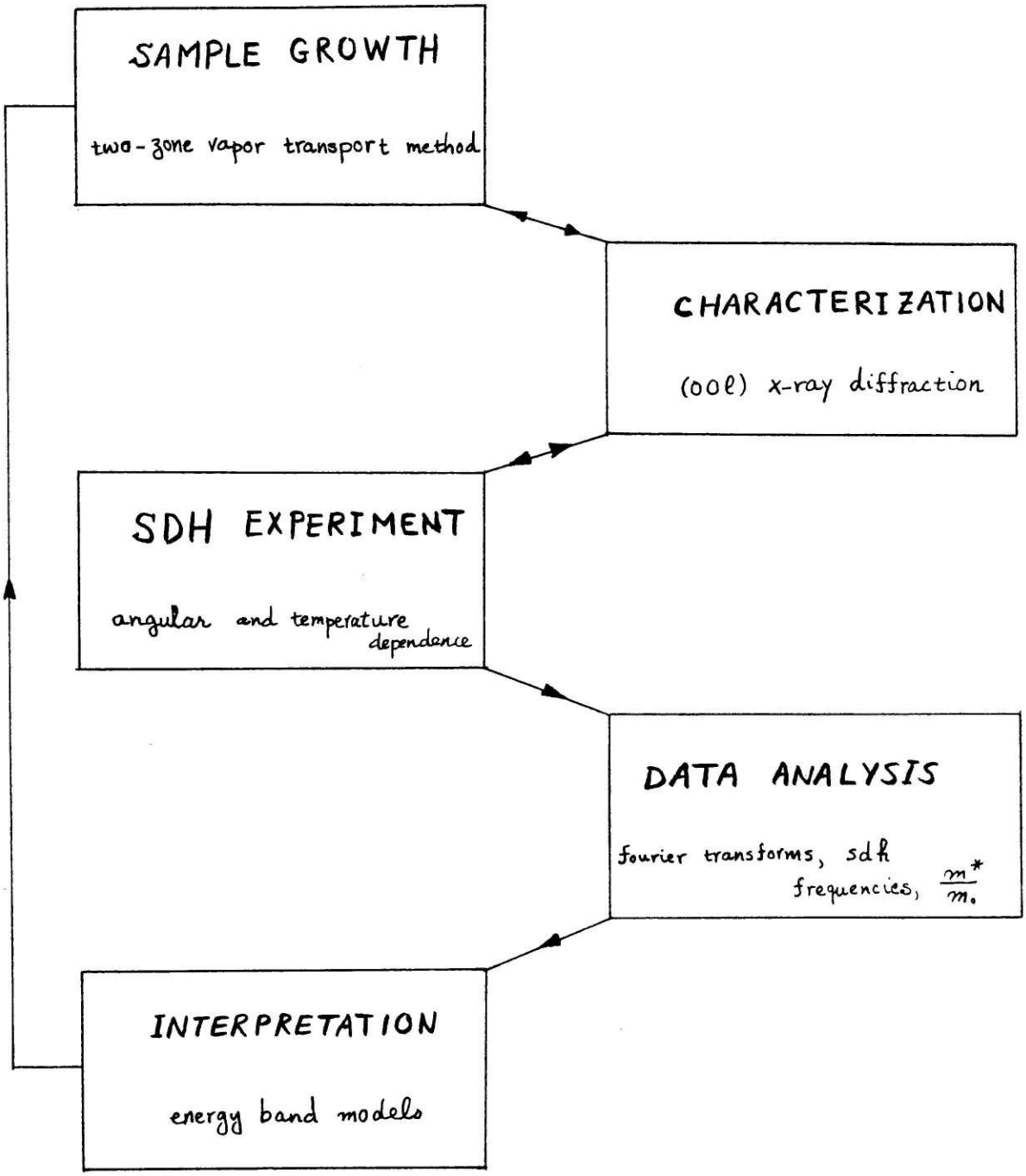


Figure 1.1
Flow chart summarizing the work done during this thesis project

# II. BACKGROUND

In section 2.1 of this chapter, the crystal structure of graphite and graphite intercalation compounds (GIC) as well as some of their interesting properties will be presented. Section 2.2 reviews the graphite energy-band structure as described by the Slonczewski-Weiss-McClure (SWMcC) model [19-21]. A brief discussion of the effect of intercalation on the energy-band structure of graphite and the Fermi Surface is given in section 2.3.

Section 2.4 deals with the two models used for the interpretation of the experimental results. The first model is based on the $k_z$-axis zone-folding of pristine graphite bands, while the other is a phenomenological model developed by Dresselhaus and Leung [22] based on the $k_z$-axis zone-folded Hamiltonian of pristine graphite with an empty intercalate layer. Finally, the last section (2.5) deals with some theoretical background about the Shubnikov-de Haas (SdH) effect. In this thesis, SdH measurements were used as the experimental tool to study the Fermi Surface of the compounds.

## II-1. Graphite, GIC, and Some of Their Properties

Graphite intercalation compounds (GIC) have been known for many years. Schafhautl was the first to observe a directional "swelling" of graphite when immersed in a mixture of sulfuric and nitric acids in 1841 [23]. The nature of this swelling was not known until diffraction techniques became a common tool for studying the structure of solids. Since then a great deal of work has been done on GIC to understand their very interesting structural and electronic properties. We now know that this swelling is

due to the insertion of the layers of some parent material between the graphitic layers; this process is called "intercalation".

Ths structure of pristine graphite plays a key role in the formation and properties of these lamellar compounds. The graphite structure belongs to a hexagonal system. The carbon atoms are arranged in a hexagonal layer network with strong in-plane covalent $sp^2$ bonds (see Fig. 2.1). The interatomic distance is small, the nearest-neighbor atoms being separated by only 1.42Å. Along the c-direction, the direction normal to the plane of this honeycomb network, the layers are stacked such that the open center of each hexagon is sandwiched between two carbon atomes from neighboring layers. This stacking sequence, called the ... ABAB... stacking, results in a c-axis parameter of twice the interlayer spacing (2 x 3.35 = 6.70Å). The interaction between atoms in the c-direction is of the weak van der Waals (dipole-dipole interaction) nature. The weakness of this bonding has interesting consequences. It causes graphite to be a highly anisotropic material. The most direct evidence for this fact is the very ease with which the graphite layers are cleaved. The electronic properties of graphite are also affected by this anisotropy; while a poor conductor in a-plane, graphite is practically an insulator along the c-axis ($\sigma_a/\sigma_c \simeq 10^4$ at room temperature).

This anisotropy enables us to neglect the interaction between the layers and hence theories and calculations for a quasi-two-dimensional system of atoms can be applied and tested. Hence, graphite and its intercalation compounds are also interesting from a theoretical point of view.

Graphite becomes the host to many materials such as alkali-metals, halogens and metal-halides, and it forms lamellar compounds. The term

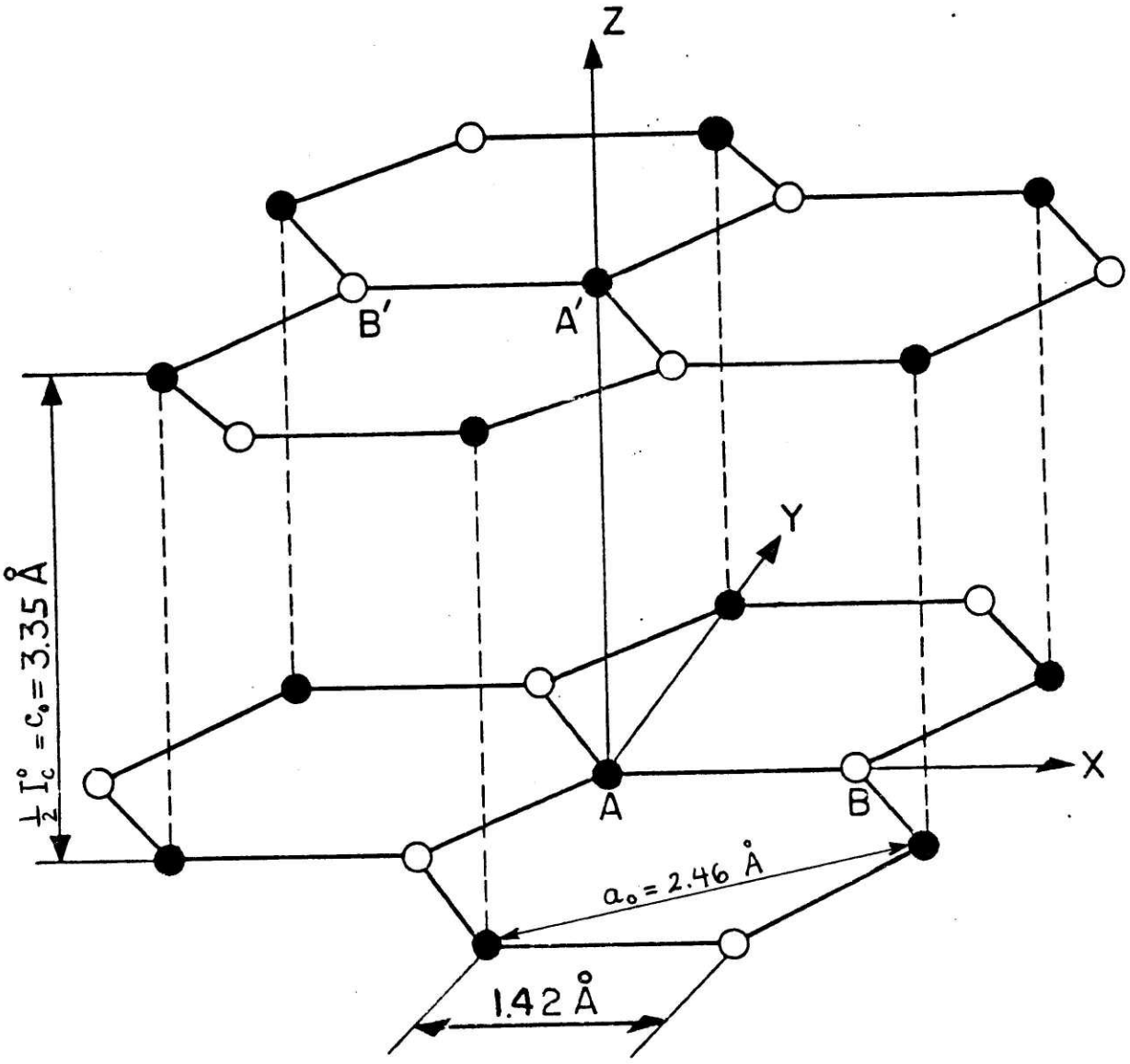


Figure 2.1. Crystal structure of graphite showing the four atoms per unit cell labeled A, A', B and B'.

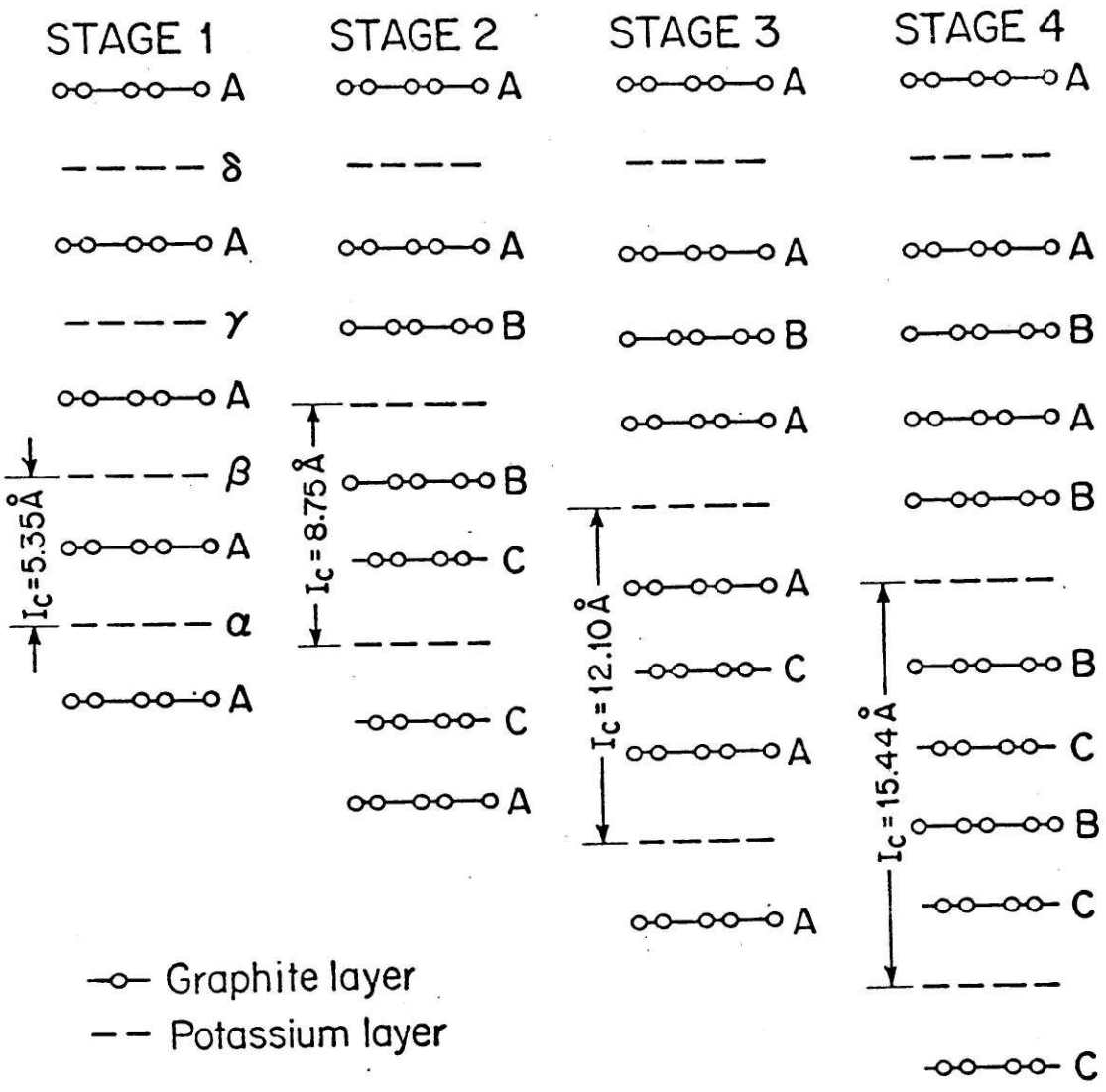


Figure 2.2

Schematic diagram showing the staging phenomenon in graphite - potassium compounds for stages $1 \leq n \leq 4$. Potassium layers are represented by dashed lines and the graphite layers by solid lines connecting the open circles. The open circles indicate a projection of the carbon atom positions and illustrate the stacking ordering for the compounds. The distance between adjacent intercalate layers, $I_c$, is shown for different stages.

"lamellar" is generally used to denote compounds which are formed by stacking layers of species on top of each other. In our case, several graphitic layers sandwich one intercalate layer repeatedly and form the GIC, with stage index n denoting the number of contiguous graphitic layers between two nearest intercalate layers. These compounds show interesting properties similar to those of graphite. The degree of anisotropy usually changes, depending on the intercalate species, while the in-plane properties change from those of pure graphite, too.

The interlayer and intralayer interactions between graphite and intercalate have dramatic effects: in some acceptor GIC, the $\sigma_a/\sigma_c$ ratio is enhanced by two orders of magnitude ($\sigma_a/\sigma_c \sim 10^6$) and some compounds ($C_{16}AsF_5$)exhibit a conductance along the a-plane diretions comparable to that of copper [24]. Some alkali-metal-GIC become superconducting at low temperatures, while neither the alkali-metal nor the host graphite is a superconductor [25]. Also, some GIC are used as catalysts for organic chemical reactions [1].

The above characteristics, together with the aforementioned interest in two-dimensional physics, make the graphite lamellar compounds the focus of much recent attention.

## II-2. Features of the Graphite and GIC Structures

For future reference, a summary of the graphite structure follows [26]. The material is:

Hexagonal (see Fig. 2.1) with lattice constants:

$$a_o = 2.46\text{Å}$$
$$I_c^o = 6.70\text{Å} \quad .$$

The interplanar distance is usually denoted by $c_o$ ($= \frac{1}{2} I_c^o = 3.35\mathring{A}$) . There are four atoms in the basis and these are located at:

$$(0,0,0);\quad \left(\frac{1}{3},\frac{1}{3},0\right);\quad \left(\frac{2}{3},\frac{2}{3},\frac{1}{2}\right);\quad \left(0,0,\frac{1}{2}\right) \quad .$$

The primitive lattice vectors are:

$$\begin{aligned} \vec{a} &= a_o \hat{x} \\ \vec{b} &= a_o\left(\frac{1}{2}\hat{x} + \frac{\sqrt{3}}{2}\hat{y}\right) \\ \vec{c} &= 2c_o \hat{z} \end{aligned} \qquad (2.1)$$

and the reciprocal lattice vectors are:

$$\begin{aligned} \vec{a}^* &= \frac{2\pi}{a_o}\left(\hat{x} - \frac{\sqrt{3}}{3}\hat{y}\right) \\ \vec{b}^* &= \frac{2\pi}{a_o}\ \frac{2\sqrt{3}}{3}\hat{y} \\ \vec{c}^* &= \frac{2\pi}{2c_o}\left(\hat{z}\right) \quad . \end{aligned} \qquad (2.2)$$

Note that the reciprocal lattice represents a hexagonal system, too. (See Fig. 2.3.)

The type of graphite used in these experiments was highly oriented pyrolytic graphic (HOPG) [27] . The c-axis in HOPG is aligned to better than 1°. The a-axes are aligned within domains that are $\sim$ 1 micron in diameter in the a-plane.

There are some aspects which are crucial in understanding the structure of the GIC. These are presented briefly below.

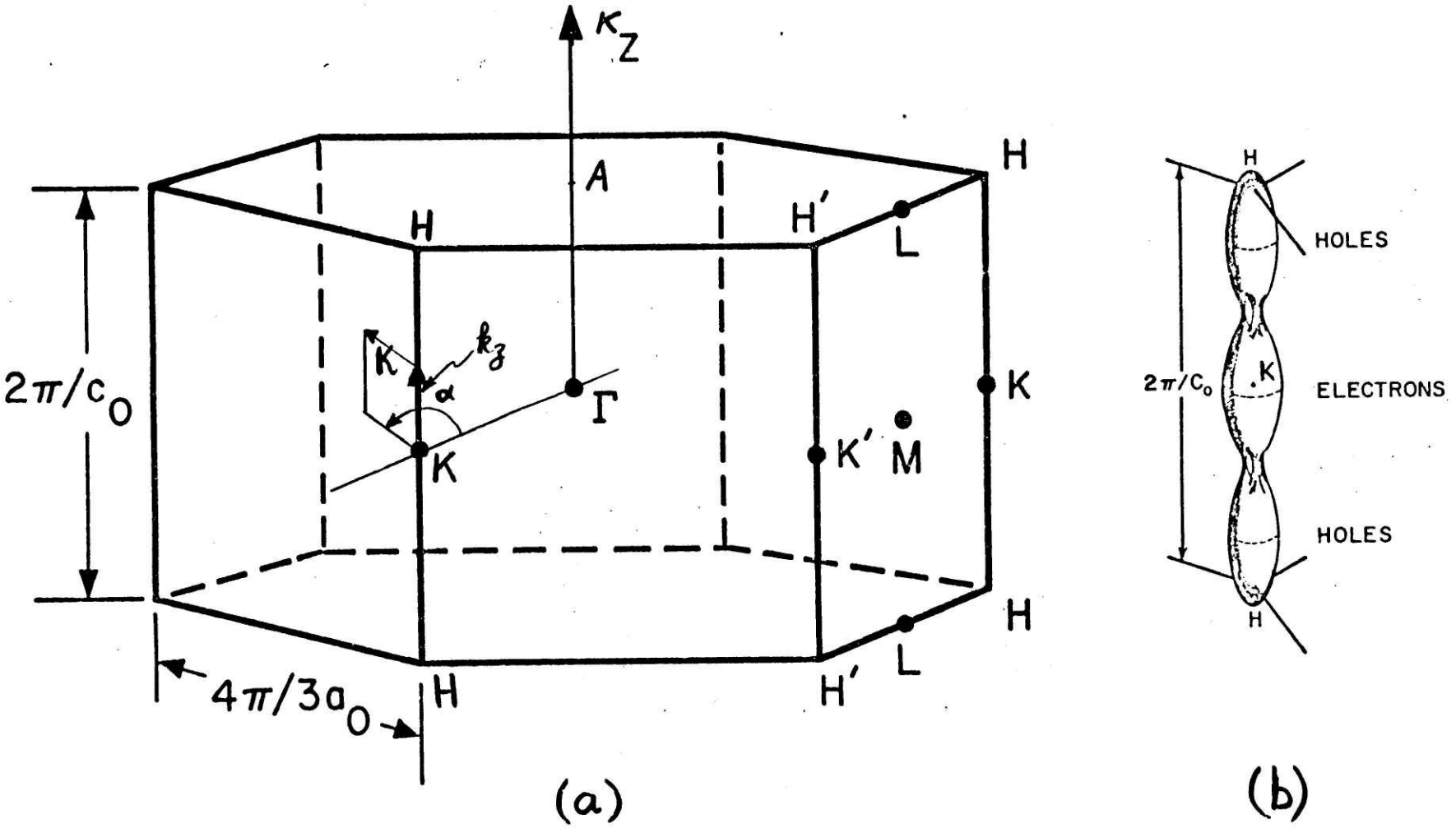


Figure 2.3

(a) Hexagonal Brillouin zone with those high symmetry points labeled that are of particular interest for graphite

(b) The Fermi surface of graphite determined by SWMcC model (with $\gamma_3 = 0$).

Six of such surfaces are located at the six zone edges.

1. Stage Ordering. This is the most important feature of the GIC. Along the c-direction, the layers of the intercalate are separated by n layers of graphite, where n denotes the "stage" of the compound and assumes integer values (see Fig. 2.2). Stage zero (n = 0) refers to the pure parent (intercalate) material and stage infinity (n = $\infty$) is for pure graphite.

2. Graphitic Intraplanar Ordering. The in-plane ordering in graphite planes (open hexagons with carbon atoms at the corners) is retained in the lamellar compounds. The a-lattice constant of graphite shows little or no change relative to that of pristine graphite ($a_{o_{gr}} = 2.46\mathring{A}$).

3. Graphite Interplanar Ordering. There exists a stacking order for graphitic layers (not necessarily that of pure graphite) in the compounds. For instance, the ... AXAXAXA... or ... ABXBAXABX... structures are commonly observed for stages 1 and 2 compounds. Or, we can have ABXBCXCA..., etc. Here, A,B denote graphite layers and X denotes the intercalate layer (see Fig. 2.2).

4. Intercalate Intraplanar Ordering. The intercalate species in a layer exhibit an ordered arrangement. This arrangement is usually similar to the network which intercalate species have in a cross section of the intercalate material. This site ordering may or may not be commensurate with the graphite site ordering.

5. Intercalate Interplanar Ordering. The intercalate layers may have a stacking order. For example, in stage 1 $C_8K$, alternate intercalate layers are seen to have the ... $A\alpha A\beta A\gamma A\delta A$ ...

ordering [28], where $\alpha$, $\beta$, $\gamma$,$\delta$ sites are assumed by the intercalate atoms on sequential layers.

6. Correlated Intercalate-Graphite Site Ordering. For commensurate structures, the site orderings in the graphitic layer and adjacent intercalate layers are correlated.

## II-3. Electronic Energy Band Structure of Graphite.

It was mentioned in previous sections that the interlayer interaction is very weak in graphite. Because of this large anisotropy of the crystal structure, the simplest models for the graphite energy bands are the two-dimensional models [29-31]. In these models the $2s$,$2p_x$ and $2p_y$ atomic wave functions interact to form the strongly coupled bonding and antibonding trigonal orbitals ($\sigma$-bands). The $p_z$ atomic wave functions give rise to the two valence and conduction $\pi$-bands, which are degenerate by symmetry at the six corners of the two-dimensional hexagonal Brillouin zone (BZ). The Fermi energy lies between the two $\pi$-bands and thus the two-dimensional graphite is essentially a zero-gap semiconductor. Graphite, however, is a three-dimensional solid; and the interlayer interaction, although small, has profound effects on the energy band structure of graphite, especially near the six vertical zone edges where the bandwidth is small.

As shown in Fig. 2.1, the AB stacking of the graphite layers gives rise to four carbon atoms per unit cell. Thus, there are four $\pi$-bands near the Brillouin zone edges and it is the overlap between these $\pi$-bands that is responsible for the semimetallic properties of graphite (Fig. 2.3). A number of first principles band calculations have been

carried out, some based on a two-dimensional model and others including three-dimensional interactions [29-32]. These models are especially useful in discussing the electronic structure away from the Fermi level ($E_F$) but are generally not sufficiently accurate to interpret experimental data providing detailed information within a few hundred millivolts of $E_F$.

The most successful and widely used three-dimensional model for the dispersion relations for the four $\pi$-bands near the Fermi level was developed by Slonczewski and Weiss [19] and by McClure [21, 21]. The Slonczewski-Weiss-McClure (SWMcC) model is especially successful for describing the behavior of the $\pi$-bands near the zone edge and has been used extensively to explain the various observed transport, optical, quantum oscillatory and magneto-optical properties which depend on electronic structure near the Fermi level. This phenomenological model is based on developing a Hamiltonian of the most general form consistent with the crystal symmetry of graphite. Perturbation theory is used to obtain $E(\vec{k})$ in the vicinity of the HKH axis of the BZ. Along the $k_z$ direction, a Fourier expansion with rapid convergence (because of the weak interlayer binding) is made. Since the extent of the Fermi surface from the zone edge is small compared with the BZ dimensions ( $< 0.01$), a $\vec{k}\cdot\vec{p}$ expansion is made to obtain the form of the Hamiltonian perpendicular to the HKH axis. In this model, the Hamiltonian for the $\pi$-bands is a 4 x 4 matrix of the form:

$$H = \begin{vmatrix} E_1 & 0 & H_{13} & H_{13}^* \\ 0 & E_2 & H_{23} & -H_{23}^* \\ H_{13}^* & H_{23}^* & E_3 & H_{33} \\ H_{13} & -H_{23} & H_{33}^* & E_3 \end{vmatrix} \qquad (2.3)$$

where the energies at the band edge are given by:

$$E_1 = \Delta + \gamma_1 \Gamma + \frac{1}{2}\gamma_5 \Gamma^2 \tag{2.4}$$

$$E_2 = \Delta - \gamma_1 \Gamma + \frac{1}{2}\gamma_5 \Gamma^2 \tag{2.5}$$

$$E_3 = \frac{1}{2}\gamma_2 \Gamma^2 \tag{2.6}$$

and the interaction terms are:

$$H_{13} = 2^{-1/2}(-\gamma_0 + \gamma_4 \Gamma)\sigma \exp(i\alpha) \tag{2.7}$$

$$H_{23} = 2^{-1/2}(\gamma_0 + \gamma_4 \Gamma)\sigma \exp(i\alpha) \tag{2.8}$$

$$H_{33} = \gamma_3 \Gamma \sigma \exp(i\alpha) \tag{2.9}$$

with

$$\Gamma = 2 \cos \pi\xi \tag{2.10}$$

$$\xi = k_z c_0/\pi \tag{2.11}$$

$$\sigma = \frac{1}{2}\sqrt{3} a_0 \kappa \tag{2.12}$$

In the above, $\sigma$ is the dimensionless distance from the zone edge ($\kappa$ is the in-plane wavevector measured from the zone edge), $\alpha$ is the polar angle about the zone edge, as shown in Fig. 2.3(a), $a_0 = 2.46\text{Å}$, and $c_0 = 3.35\text{Å}$. The values of the seven expansion parameters $\gamma_0, \gamma_1 \ldots \gamma_5, \Delta$ and their physical significance are listed in Table 2.1 [2]. The eigenvalues of the SWMcC Hamiltonian [Eq. 2.3] give the energy dispersion relations. These energy bands are schematically illustrated in Fig. 2.4. Note the previously mentioned band overlap in the $E_3$ band, which is responsible for the semimetallic properties of graphite. Using

Table 2.1 Slonczewski-Weiss-McClure Band Parameters for Graphite - Their Magnitudes and Physical Significance [27]

| Band Parameter | Order of Magnitude (eV) | Physical Origin |
|---|---|---|
| $\gamma_0$ | 3.16 ± 0.05 | Overlap of neighboring atoms in a single layer plane. |
| $\gamma_1$ | 0.39 ± 0.01 | Overlap of orbitals associated with carbon atoms located one above the other in adjacent layer planes. Width of $\pi$-bands at point K is $4\gamma_1$ . |
| $\gamma_2$ | - 0.020 ± 0.002 | Interactions between atoms in next-nearest layers and from coupling between $\pi$ and $\sigma$ bands. Band overlap is $2\gamma_2$ . Majority de Haas-van Alphen frequencies determined by $\gamma_2$. |
| $\gamma_3$ | 0.315 ± 0.015 | Coupling of the two $E_3$ bands by a momentum matrix element. Trigonal warping of Fermi surface is determined by $\gamma_3$. |
| $\gamma_4$ | ~ 0.044 ± 0.024 | Coupling of $E_3$ bands to $E_1$ and $E_2$ bands by a momentum matrix element. Determines inequality of K-point effective masses in valence and conduction bands. |
| $\gamma_5$ | 0.038 ± 0.005 | Interactions between second nearest layer planes. Introduced in $E_1$ and $E_2$ to be consistent with $E_3$ in the order of the Fourier expansion. |
| $\Delta$ | - 0.008 ± 0.002 | Difference in crystalline fields experienced by inequivalent carbon sites in layer planes. Volume of minority hole-carrier pocket sensitive to $\Delta$. |
| $E_F$ | - 0.024 ± 0.002 | The Fermi level is measured with respect to the H-point extremum (see Fig. 2.4 ) and is fixed by the condition that the electron density = hole density. |

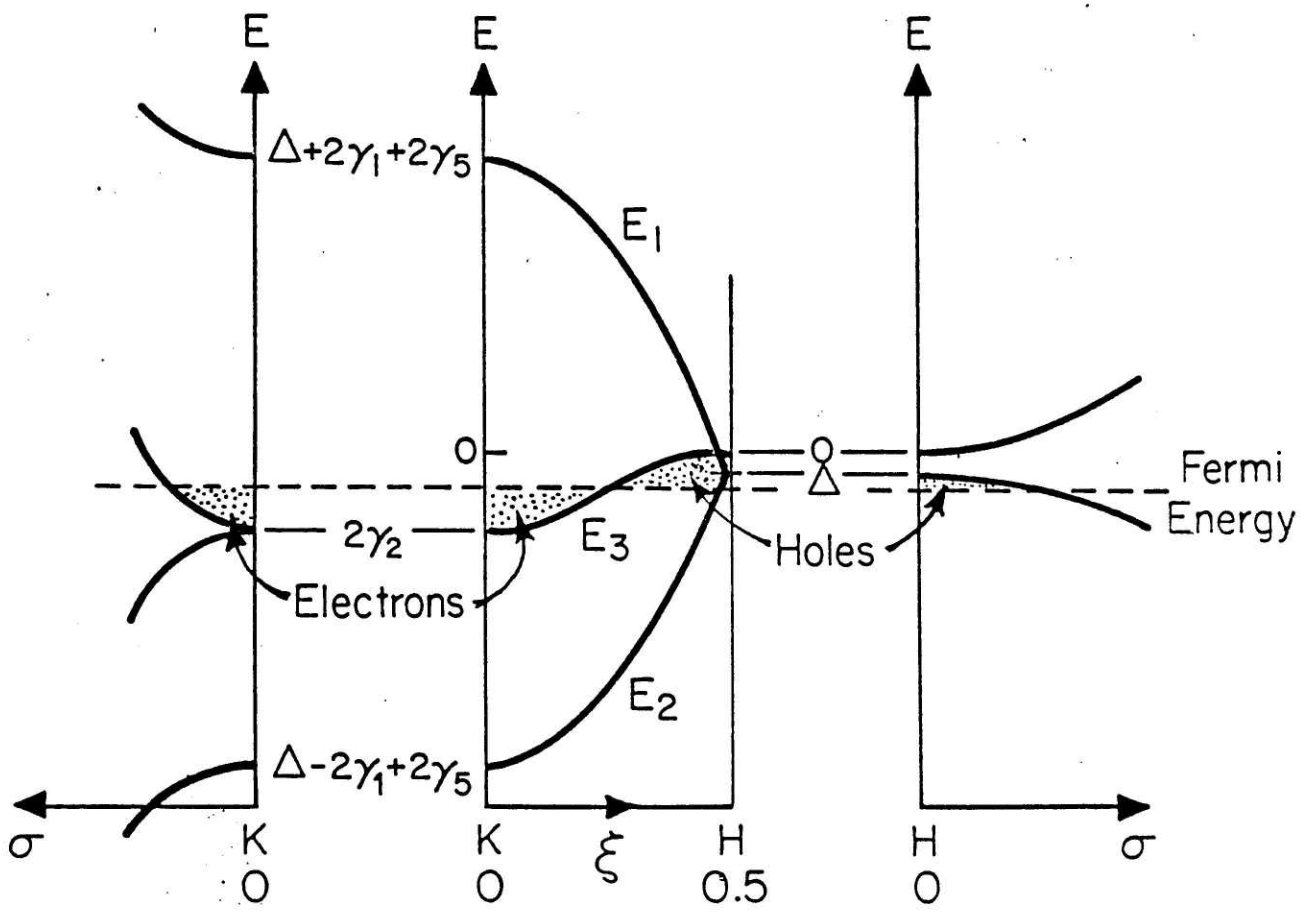


Figure 2.4

Electronic energy bands near the Brillouin zone edge (HKH axis) for three-dimensional graphite obtained from the SWMcC model.

the above model, good agreement is obtained for the effective masses, carrier concentration, magnetoreflection results, and the Fermi surface topology. The Fermi surface for pristine graphite is shown in Figs. 2.3(b) and 2.5. The location of hole and electron pockets is emphasized in Fig. 2.3, while Fig. 2.5 shows the trigonal warping present in the Fermi surface because $\gamma_3 \neq 0$. An extension of the SWMcC model has been made by Dresselhaus and Dresselhaus to include the spin-orbit effect [33] .

The Fermi surface of the GIC extends to a much larger volume of the BZ than in Pristine graphite (next section). Also, the optical properties of graphite include contributions from the energy bands throughout the BZ; therefore, of particular interest is the extension of the SWMcC model developed by Johnson and Dresselhaus [34,35], which yileds the dispersion relations for the $\pi$-bands throughout the BZ. This extension is based on using the symmetry properties of the Hamiltonian and developing a three-dimensional Fourier expansion for the basis functions. Appropriate band parameters are evaluated for this model by considering the Fermi surface data near the zone edge, the optical data below 6eV, and the requirement that the dispersion relations reduce to the SWMcC form in the vicinity of the zone edge HKH. The above extension has been further developed by Dresselhaus and Leung to obtain dispersion relations for the graphite intercalation compounds. This will be explained in more detail in section 2.4.2 as one of the models used to interpret the experimental results.

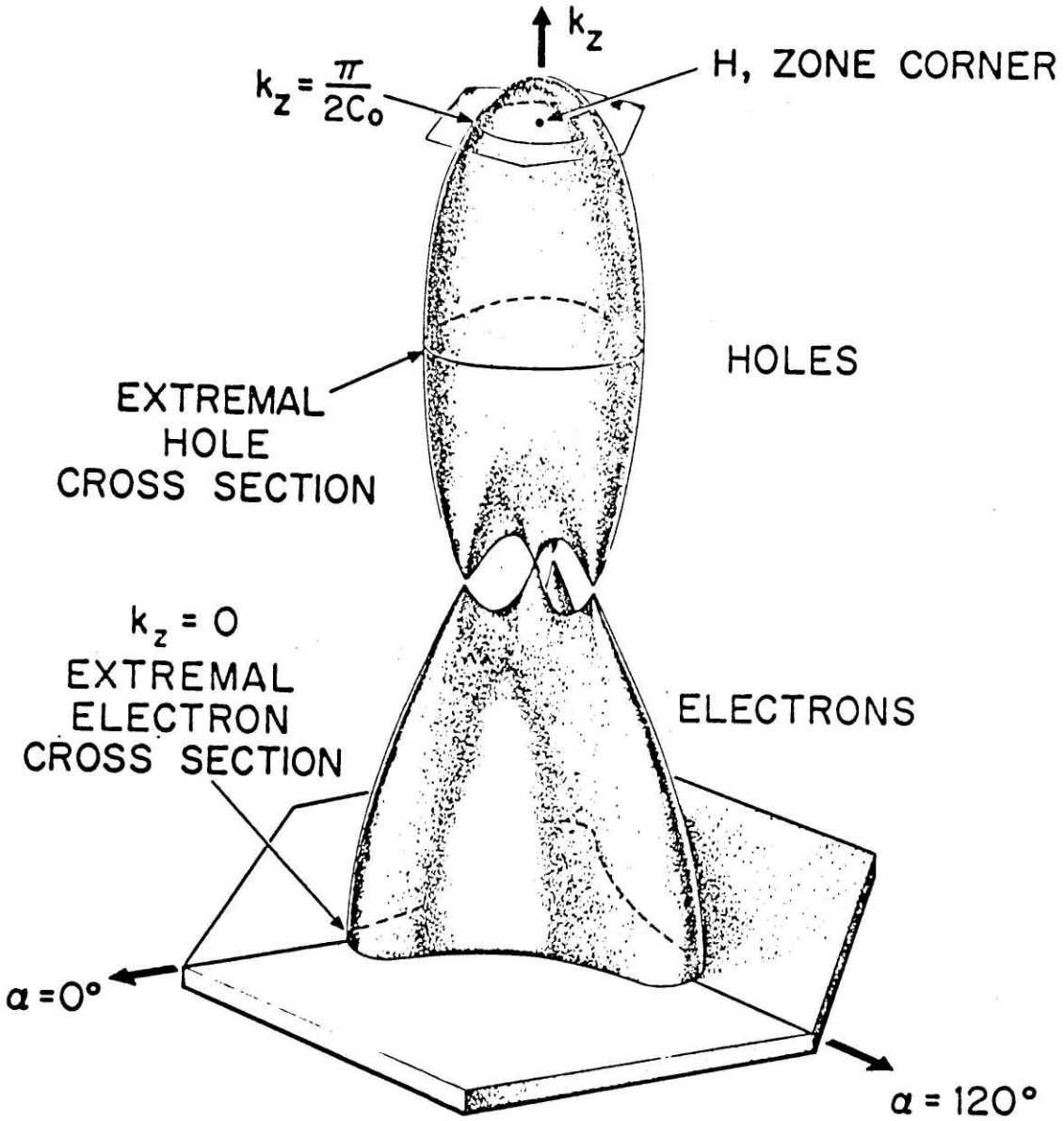


Figure 2.5

Fermi surface of graphite showing the trigonally warped feature of the electron and hole surfaces. The extremal cross sections ($_{\perp}k_z$) observable by the SdH experiment are illustrated. The "cap" at the H-point ( $k_z = \pi/c_o$) is also indicated.

## II-4. Effect of Intercalation on the Energy Band Structure and the Models for the Fermi Surface of GIC

In treating the properties of the graphite intercalation compounds, a strong similarity between the structural and electronic properties of the GIC and the parent materials (graphite and intercalant) is recognized [2]. The physical basis for this relation is clear: in both graphite and the intercalant, the intralayer bonding is strong, while the interlayer bonding between graphite-graphite and intercalate-graphite layers is much weaker. In the case of dilute (high-stage) compounds, where there are several graphite layers for one layer of intercalant, the electronic structure can be expected to be dominated by that of pristine graphite. In fact, even for the most concentrated (stage one) compounds of lithium and potassium, the first-principle calculations indicate a structure closely related to the graphite $\pi$-bands [16-18]. The experimental results on the electronic properties of GIC also support the idea that the graphite $\pi$-bands play a dominant role in the electronic structure of the intercalation compounds [5-7,36].

The above introduction illustrates the importance of the pristine graphite electronic structure for an understanding of the electronic properties of the intercalation compounds. In sections 2.4.1 and 2.4.2 two models which are closely based on the graphite energy bands, are presented. These models are used in Chapter VI to interpret the experimental data.

### 2.4.1 The Dilute-Limit Model

The dilute-limit model, which is based on the SWMcC graphite $\pi$-bands, was originally proposed by McClure [21] to account for the electronic properties of the graphite-bromine compounds. In this model,

the basic structure of the $\pi$-bands is preserved and the effect of intercalation is treated mainly in terms of a shift in the Fermi level. In the case of donor intercalants (such as alkali-metals), the Fermi level is raised to accommodate the additional electrons, while for acceptor compounds, such as halogens and metal-halides, the Fermi level is lowered to accommodate extra holes. The basic assumption made in this model is that the electronic interaction between the intercalate monolayers and the two adjacent graphite bounding layers is limited to interactions within this sandwich. In other words, the intercalate layer is effectively screened by the two graphite bounding layers, and hence the electronic structure of the interior layers is basically graphitic. This assumption implies that the validity of the dilute-limit model is restricted to the intercalation compounds with stage index $\gtrsim$ 4 or 5, and applies to the graphite interior layers. The SWMcC band parameters(Table 2.1) can be modified in this model for the intercalation compounds. However, the magnetoreflection experiments [36] have shown that very small modifications are needed and that the band parameters remain basically graphitic.

In the dilute-limit model, the simplification $\gamma_3 = 0$ can be made in the SWMcC Hamiltonian to obtain simple analytic forms for the energy bands. Setting $\gamma_3$ equal to zero changes the topology of the Fermi surface and the trigonal warping vanishes. The cross-sectional areas of the Fermi surface, however, are approximately unchanged [37] and thus Eq. 2.15 (below) is a good approximation for the actual cross-sectional area which includes trigonal warping. With $\gamma_3 = 0$, the eigenvalues for the Hamiltonian, Eq. 2.3, are the four solutions:

$$E = \frac{1}{2}(E_1 + E_3) \pm [\frac{1}{4}(E_1 - E_3)^2 + (\gamma_o - \gamma_4 \Gamma^2)\sigma^2]^{1/2} \qquad (2.13)$$

$$E = \frac{1}{2}(E_2 + E_3) \pm [\frac{1}{4}(E_2 - E_3)^2 + (\gamma_o + \gamma_4 \Gamma)^2 \sigma^2]^{1/2} \qquad (2.14)$$

The cross-sectional area for the Fermi surface (area perpendicular to $k_z$-direction) for electrons can be obtained from Eq. 2.13 by setting $E = E_F$. The result is given by

$$A_e(\xi) = \frac{4\pi}{3a_o^2\gamma_o^2} \frac{(E_2 - E_F)(E_3 - E_F)}{(1 + \nu)^2} \qquad (2.15)$$

in which $\nu = 2(\gamma_4/\gamma_o)\cos \pi\xi$. To obtain the electron carrier density $n_e(E_F)$, the above $A_e(\xi)$ can be integrated along $k_z$:

$$n_e(E_F) = \frac{1}{\pi c_o} \int_{-1/2}^{+1/2} A_e(\xi)\, d\xi \qquad (2.16)$$

A similar expression can be found for the cross-sectional area of the hole surface for acceptor compounds using Eq. 2.14 under the substitution $E_2 \rightarrow E_1$, $(1+\nu)^2 \rightarrow (1-\nu)^2$. Dresselhaus et al [38] have used the above expressions to plot the dependence of the extremal cross-sectional areas of the electron and hole surfaces at K and H points and the carrier concentration as a function of the Fermi level (see Figs 2.6 and 2.7). Once the position of the Fermi level (relative to the K-point band edge) is found experimentally, from magnetoreflection or Shubnikov-de Haas (SdH) experiments, for instance, then the above dependences can be applied to the electronic properties.

The first model used in this thesis to interpret the SdH results is based on Fig. 2.7, and the zone-folding effect due to the superlattice

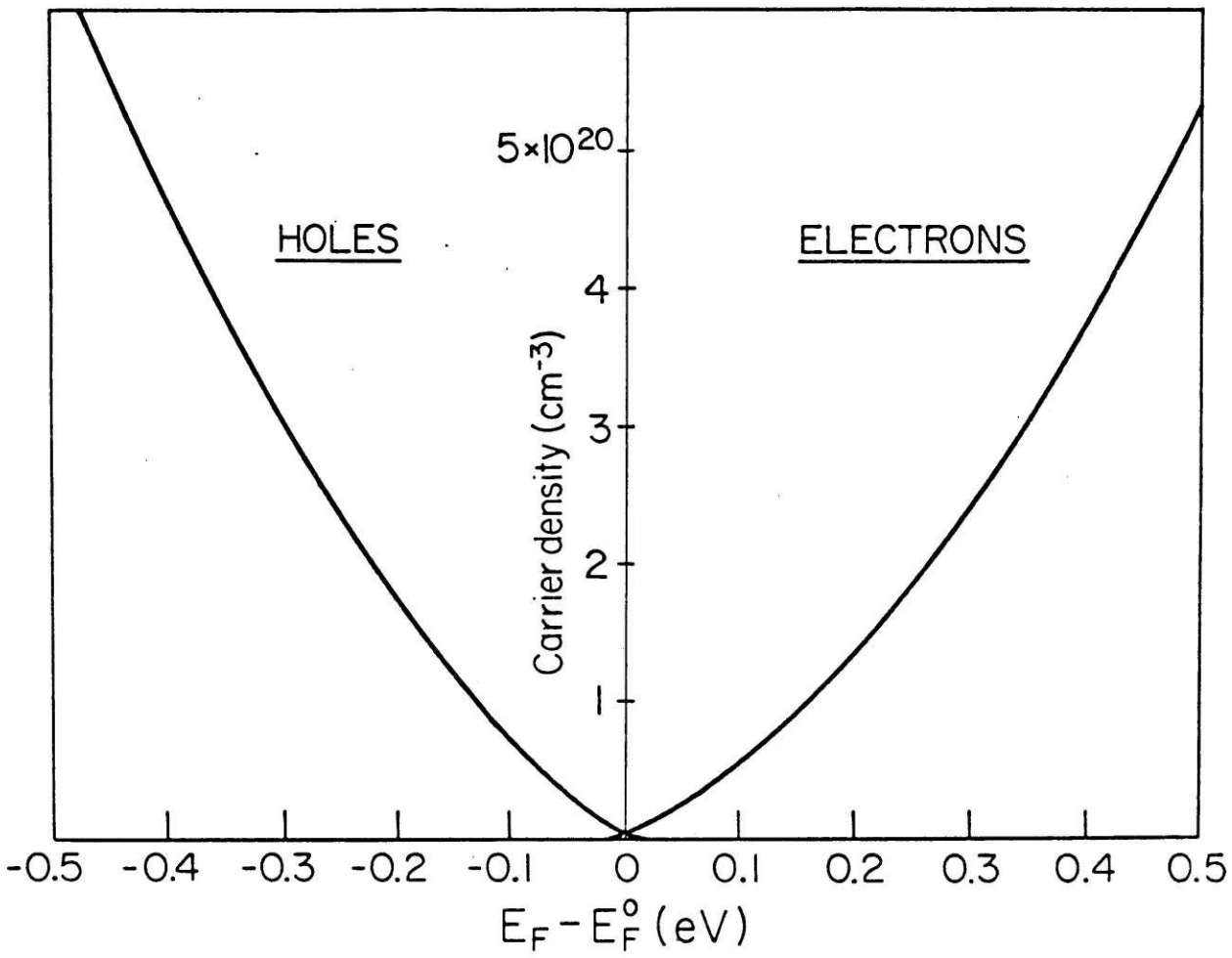


Fig. 2.6 [38]

Based on the SWMcC graphite rigid-band model, the carrier density is plotted as a function of the Fermi level shifts relative to the graphite Fermi level $E_F$ where the electron and hold carrier densities are equal.

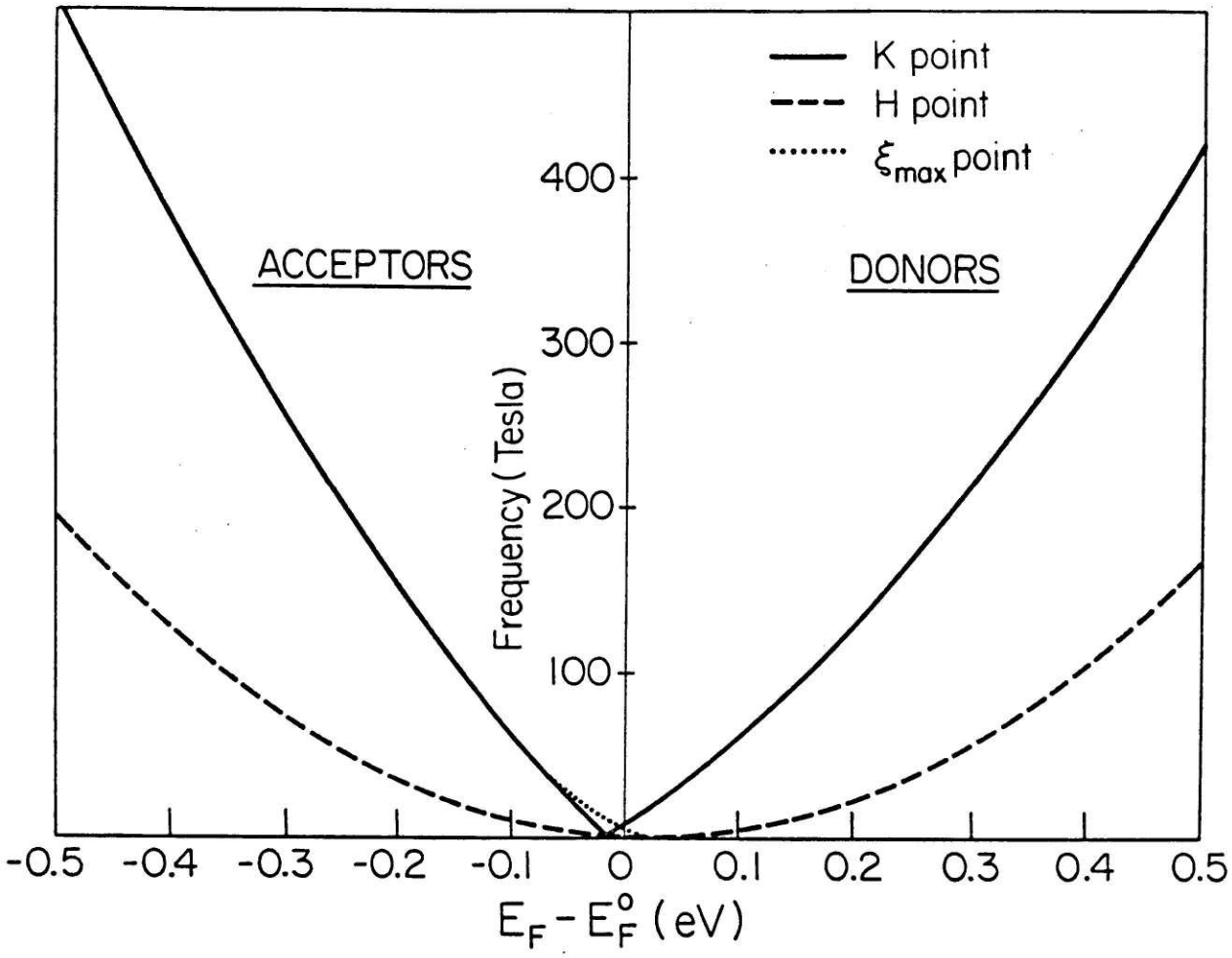


Fig. 2.7 [38]

Shubnikov-de Haas frequencies (in Tesla) obtained from the SWMcC model as a function of the Fermi level shift. These SdH frequencies correspond to the extremal cross sections of the Fermi surface around the K and H-points. For a small range of $(E_F - E_F^o)$, extremal Fermi surface cross sections (dotted line) exist between K- and H-points $(0 < \xi < 0.5)$

structure of the intercalation compounds (Chpater VI). Zone-folding is a common technique applicable to crystals with a superlattice periodicity. In zone-folding the dispersion relation E(k) for the host material is folded into a Brillouin zone compatible with the crystal symmetry of the superlattice solid. Perturbation theory can then be applied to account for the effect of the periodic potential. In applying the zone-folding technique to the graphite intercalation compounds, the symmetry of pristine graphite structure is used as the approximate symmetry for the intercalation compounds, while the additional superlattice periodicity due to the intercalant is treated as a perturbation. In the case of graphite compounds, both the in-plane superlattice and superlattice structure along the $k_z$ direction can be present and should be considered.

In the dilute-limit model, the zone-folding along the $k_z$-direction is used to treat the effect of staging (superlattice structure along the c-direction due to the intercalant). An example of such zone-folding for a stage-4 compound [5] is shown in Fig. 2.8. The cross section of the Fermi surface resulting from the graphite bands is sketched in Fig. 2.8(a). The distance $\overline{HH} = \frac{2\pi}{I_c} = \frac{2\pi}{2c_o}$ is the height of the Brillouin Zone (see Fig. 2.3). Here $I_c^o$ = 6.70Å is the graphite lattice constant along the z-direction (see Fig. 2.1). The new zone boundaries indicated by $\tilde{H}$ are the result of the larger lattice constant $I_c$ for a stage- 4 compound ($\tilde{\overline{HH}} = \frac{2\pi}{I_c}$). For simplicity, it is assumed in this figure that there is no stacking periodicity and that $I_c = n * c_o = 4*3.35 =$ 13.40Å. In actuality, $I_c$ is intercalant-dependent and is not equal to n * c. (See Fig. 2.2 for potassium compounds.)†

† In the analyses presented in Chap. VI the measured $I_c$ values are used. (See Chap. III for determination of $I_c$.)

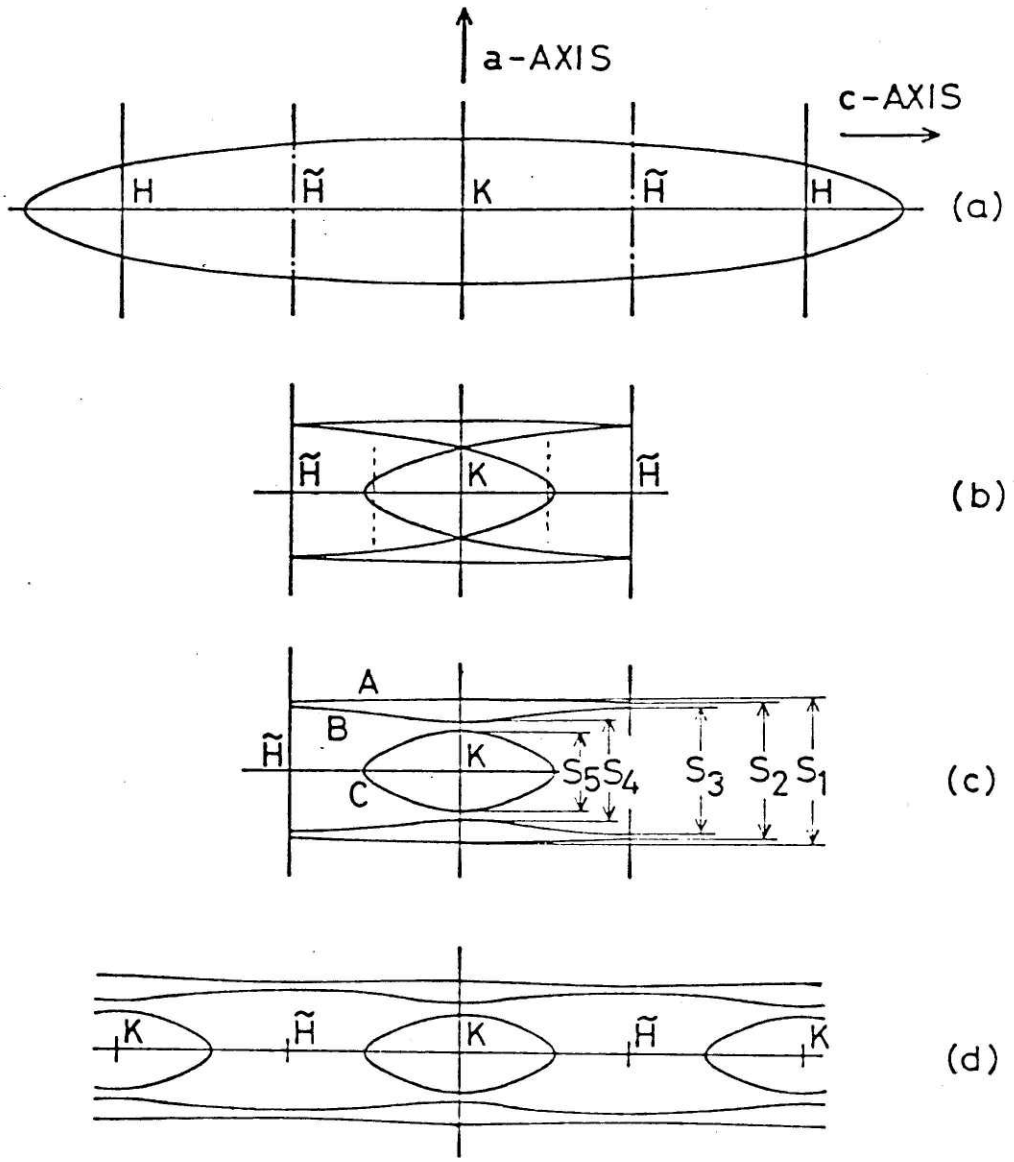


Figure 2.8 [5]

Construction of the Fermi surfaces [5] for a stage-4 compound using the dilute-limit model and zone-folding.

a) Cross section of the Fermi surface is shown assuming the graphite rigid-band model and a shifted Fermi level to accommodate the additional electrons (or holes).
b) Zone-folding along the c-direction is performed to account for the superlattice periodicity in this direction.
c) Schematic Fermi surfaces are deduced from (b) by introducing splittings at the new zone boundaries due to the periodic potential of the superlattice.
d) Fermi surfaces as constructed in (c) are shown in the extended zone scheme.

In Fig. 2.8(b), the folding of the Fermi surface on to the reduced-zone scheme is shown. The effect of the periodic potential due to the superlattice is shown in Figs. 2.8(c) and 2.8(d) for the reduced and extended zone schemes. The gaps that open up at the superlattice zone boundaries as a result of the periodic potential modify the Fermi surface as shown in Figs. 2.8 (c) and (d). The resulting Fermi surface indicates that there are five extremum cross-sectional areas perpendicular to the c-axis (denoted by $S_1$ through $S_5$) which should be observable in the SdH experiment. This model was used by Tanuma et al [5] to interpret the SdH results for a K-stage-4 compound and in Chapter VI Tanuma's results will be discussed together with our results when use of the model is made.

2.4.2. A Phenomenological Band Model for GIC

Although there are several first-principles band calculations available for the graphite intercalations compounds, they all focus on stage 1 compounds [16-18]. These stage-1 models have been applied to predict the Fermi surface for these compounds; good agreement is obtained for $C_8K$[5]. The calculations focus on stage 1 mainly, because of the complexity of the calculations, due to the large unit cell and the large number of orbitals that are involved in the high stage compounds. As a result, no first-principles calculations for high stage ($n > 2$) compounds have yet been carried out. However, some phenomenological models have been developed [17,19,39] that do treat high-stage compounds. The model, developed by Dresselhaus and Leung,[22] has the advantage that it can be applied

to any stage and intercalant, and therefore is especially useful for the interpretation of experimental results. This model will be used in Chapter VI to discuss the experimental SdH data.

A detailed presentation of this model is given by Leung [40], and here only a brief summary of the model is presented. As mentioned before, this model is also directly based on the graphite $\pi$-bands. It uses the previously discussed three-dimensional Fourier expansion of the graphite $\pi$-bands [35] and is thus valid throughout the Brillouin zone. The matrix elements of the Hamiltonian in the Fourier expansion representation are chosen so that the Hamiltonian is consistent with the restrictions imposed by the crystal symmetry, and also that it reduces to SWMcC at the zone edge. This Hamiltonian for the $\pi$-bands has the form:

$$H_o(\vec{K}_s) = \begin{vmatrix} H_{AA} & H_{AB} & H_{AB'} & H_{AA'} \\ H^*_{AB} & H_{BB} & H_{BB'} & H_{AB'} \\ H^*_{AB'} & H^*_{BB'} & H_{BB} & H_{AB} \\ H^*_{AA'} & H^*_{AB'} & H^*_{AB} & H_{AA} \end{vmatrix} \qquad (2.17)$$

where the matrix elements are given in references [34] and [40].

To incorporate the effect of staging (superlattice along the z-direction), zone-folding is used. The repeat distance along the c-axis, assuming for the moment that the intercalate layer is indistinguishable from graphite, is given by $I_c = n_* c$, where $c_o = 3.35\text{Å}$. The zone-folded Hamiltonian is therefore [22]:

$$H_{folded}(\vec{k}_s) = \begin{vmatrix} H_o(\vec{k}_s) & 0 & \cdots & \\ 0 & H_o(\vec{k}_s + \frac{\pi}{\ell c_o}\hat{z}) & & \\ \vdots & & \ddots & \\ & & & H_o(k_s + \frac{\ell-1}{\ell}\frac{\pi}{c_o}\hat{z}) \end{vmatrix} \quad (2.18)$$

where $\ell = (n+1)/2$ for odd stages and $(n+1)$ for even stages (stage = n), and each of the $H_o$ blocks is a 4x4 SWMcC Hamiltonian given in Eq. 2.17. The zone-folded Hamiltonian (Eq. 2.18) is transformed to a layer representation by a unitary transformation:

$$H_{layer}(\vec{k}_s) = U\, H_{folded}(\vec{k}_s) U^{-1} \quad (2.19)$$

so that the effect of intercalation can be considered explicitly. The resulting Hamiltonian in the layer representation is written as

$$H_{layer}(\vec{k}_s) = \begin{vmatrix} H_{A_oA_o} & H_{A_oB_o} & \cdots & \\ H_{A_oB_o} & H_{B_oB_o} & H_{B_oA_1} & \\ \vdots & H_{B_oA_1} & H_{A_1A_1} & \\ & & & \ddots\ H_{B_{\ell-1}B_{\ell-1}} \end{vmatrix} \quad (2.20)$$

where the blocks $H_{A_iA_j}$, $H_{A_iB_j}$, $H_{B_iB_j}$ ... are 2x2 matrices and $A_i$, $B_i$ are layer subscripts. Note that, since the unitary transformation does not change the eigenvalues of the Hamiltonian, the energy bands obtained from Eq. 2.20 are identical to the SWMcC bands. The advantage of having a layer Hamiltonian such as Eq. 2.20 is that the effect of

intercalation can easily be incorporated by substituting matrix blocks specific to the intercalant species in place of every $(n+1)^{st}$ graphite layer. The resulting Hamiltonian for odd stage n is:

$$H_{GIC}^{(n)} = \begin{vmatrix} H_{XX} & H_{XB_o} & H_{XA_1} \cdots & H_{XB_\lambda} \\ H_{XB_o}^{\dagger} & H_{B_oB_o} & H_{B_oA_1} & \\ H_{XA_1}^{\dagger} & H_{B_oA_1}^{\dagger} & H_{A_1A_1} & \\ \vdots & & \ddots & \\ H_{XB_\lambda}^{\dagger} & & & H_{B_\lambda B_\lambda} \end{vmatrix} \qquad (2.21)$$

where $\lambda = (n-1)/2$ and X denotes an intercalate layer. For the even stage compounds, the Hamiltonian is:

$$H_{GIC}^{(n)} = \begin{vmatrix} H_{XX} & H_{XB_o} & \cdots & & H_{XB_n} \\ H_{XB_o} & H_{B_oB_o} & \ddots & & \\ \vdots & & H_{A_\mu A_\mu} & H_{A_\mu X} & \\ & & H_{A_\mu X}^{\dagger} & H_{XX} & H_{XA_\nu} \\ & & & H_{XA_\nu}^{\dagger} & H_{A_\nu A_\nu} \\ & & & & \ddots \\ H_{XB_n}^{\dagger} & & & & H_{B_nB_n} \end{vmatrix} \qquad (2.22)$$

where $\mu = n/2$ and $\nu = (n/2) + 1$.

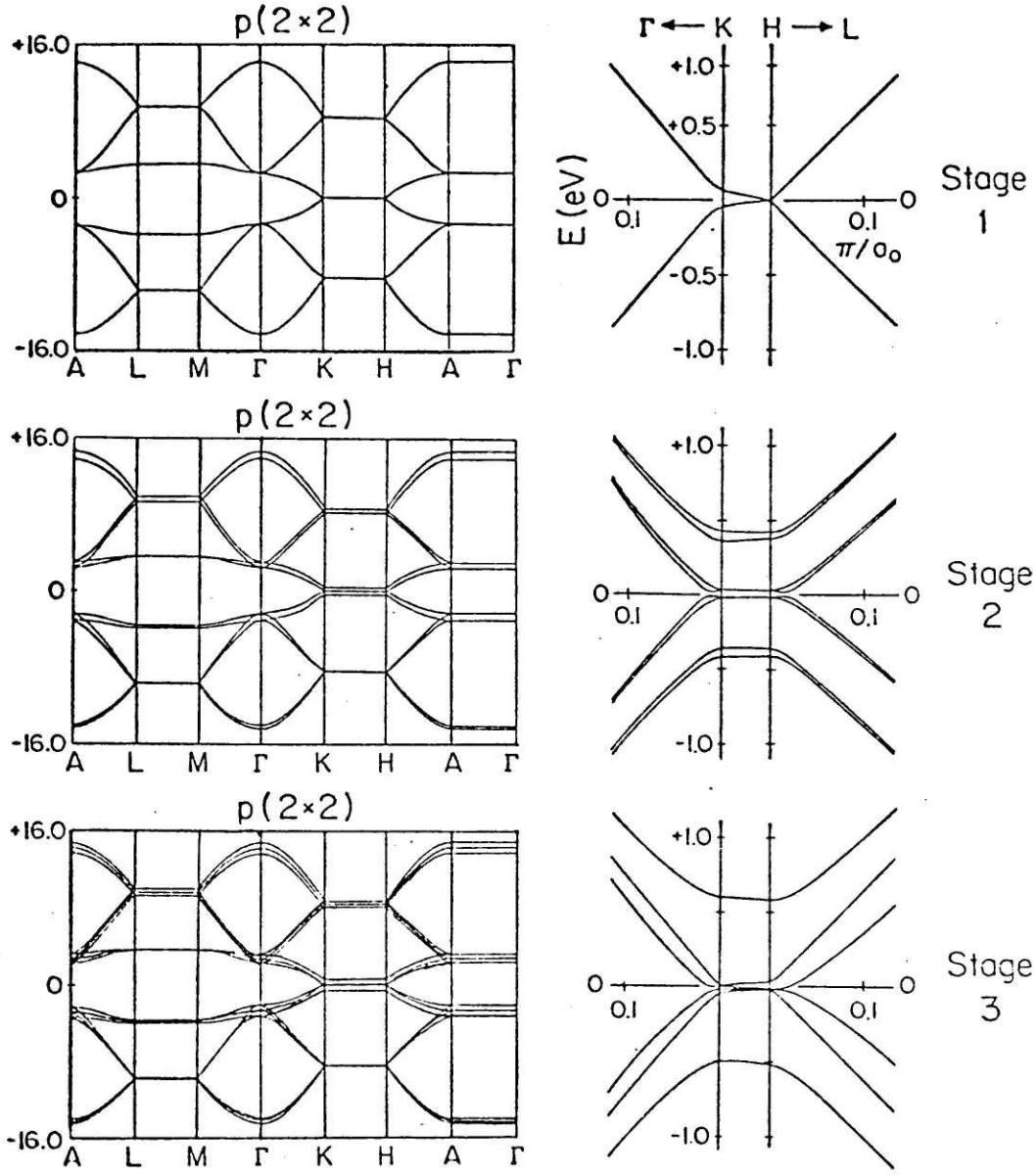


Figure 2.9 [40]

Electronic energy levels derived by $k_z$-axis zone-folding of the three-dimensional Fourier expansion of the pristine graphite $\pi$-band Hamiltonian for a primitive (2 x 2) superlattice. An empty intercalate layer is assumed and the expansion parameters are based on the SWMcC parameters along the HK axis. On the right, an expanded scale is used to plot the levels on and near the HK axis.

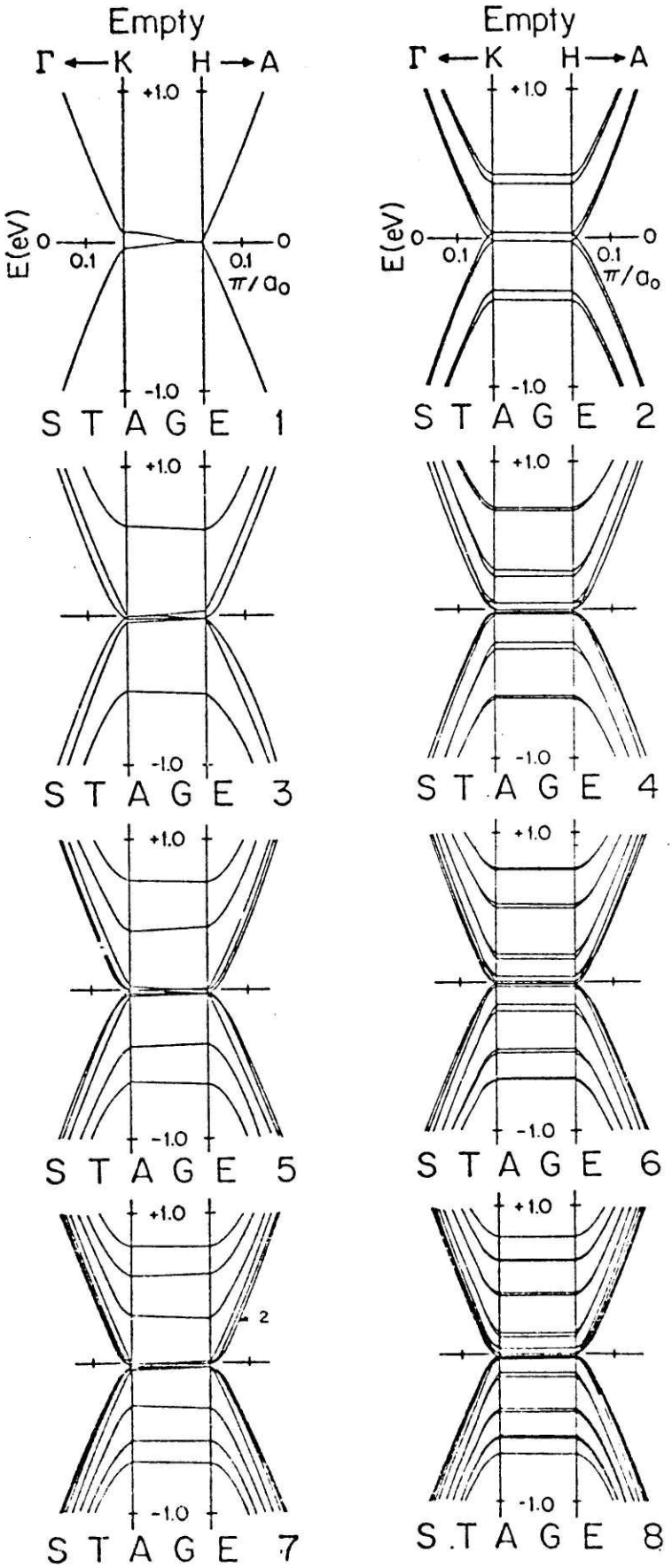


Figure 2.10 [40]

$E(\vec{k})$ for graphite intercalation compounds along and near the edge of the Brillouin zone. Bands are for the "empty" intercalate layer model with no graphite-intercalate interaction.

For donor compounds, $E_F > 0$ and there are up to n (for odd stage) or 2n (for even stage) electron pockets.

An explicit diagonalization of matrices (2.21) and (2.22) can be made to obtain the k-dependence of the energies (eigenvalues). For the simplest case, called the "empty intercalate layer model", the intercalate layer is assumed to be "vacuum" -- i.e., $H_{XX} = H_{XA_i} = H_{XB_j} \equiv 0$. To distinguish between donor and acceptor compounds, interaction terms may be introduced so that the intercalate layer is allowed to interact with the graphite bounding layers. Plots of E(k) for different stage compounds based on the empty intercalate layer model are shown in Figs. 2.9 and 2.10 [40]. Figure 2.9 considers explicitly the effect of an in-plane superlattice and calculations for several different in-plane superlattices show that the effect of the in-plane superlattice on $E(\vec{k})$ within $\pm$ 1 eV is very small and can be neglected. Figure 2.10 considers $E(\vec{k})$ for a larger number of stages, but assumes no in-plane superlattice structure. Once such plots are available, the determination of the Fermi surface is dependent only on one additional parameter, namely, the Fermi level $E_F$. The Fermi level can be determined either from an assumed charge distribution in the graphite layers or from experiments such as magnetoreflection, or -- if we are to fit SdH data -- we can set $E_F$ such that the resulting Fermi surface cross sections match the experimentally observed frequencies. The Fermi level is determined from SdH data in this study (chapter VI).

For the donor compounds, $E_F$ is positive and there are electron pockets. Note from Fig. 2.10, and also from Eqs. 2.21 and 2.22, that there are 2n bands for odd stage and 4n bands for even-stage compounds.*

* The larger number of bands for even stages stems from the fact that, because of the AB stacking (Fig. 2.2) present in even stage compounds, the unit cell is twice as large as the one without AB stacking. Note also, however, that the bands for even stage compounds are nearly degenerate in pairs (Fig. 2.10).

For donor compounds, half of these bands are completely occupied and the other half may or may not be partially occupied. Thus, depending on the position of $E_F$, we can have up to n (for odd stage) and 2n (for even stage) electron pockets, assuming one pocket per band. Since Landau level extrema may occur at both the H and K points, additional carrier pockets or Fermi surface extrema may occur. As will be further discussed in Chapter VI, these numerous carrier pockets give rise to a great number of Fermi surface cross sections (for high-stage compounds), which is consistent with the many frequencies that are observed experimentally.

## II-5. Shubnikov-de Haas (SdH) Effect

The Shubnikov-de Haas (SdH) effect refers to the periodic oscillatory behavior of the electrical resistivity as a function of $H^{-1}$ (H is the magnetic field strength). The quantization of the electronic energy levels in the presence of a magnetic field results in magnetic-field dependent oscillations in the density of states at the Fermi level. These oscillations are responsible for the oscillatory magnetoresistance as well as other quantum oscillatory phenomena such as the de Haas-van Alphen effect (oscillations of the magnetic susceptibility $\chi$ as a function of H). The oscillations are periodic in inverse field $H^{-1}$, at least in the high quantum number limit. The experiments based on these effects are among the most useful tools for probing the energy band structure at the Fermi level of solids. They especially provide information about the Fermi surface of metals, doped semiconductors, and semimetals.

The quantum oscilatory phenomena for most materials are fairly complicated if all details of the band structure are taken into account [41-47]. However, starting with the simplest case of a free-electron gas in a magnetic field, much insight can be acquired into the nature of the phenomena, especially the origin of the periodicity of the oscillations in $H^{-1}$. The energy eigenvalues (Landau levels) for an electron exposed to a magnetic field H along the z-direction are given by [41,46]:

$$E_n = (n + \tfrac{1}{2})\hbar\omega_o + (\hbar^2 k_z^2/2m^*) \pm \tfrac{1}{2} g \mu_B H, \qquad n=0,1,2,... \qquad (2.23)$$

where $m^*$ is the isotropic effective mass, $\omega_o = eH/m^*c$ is the cyclotron frequency, $k_z$ is the wave vector in the z-direction, g is the spectroscopic splitting factor, and $\mu_B$ is the Bohr magneton. According to Eq. (2.23), as a result of the magnetic field, the electronic energy levels are split into magnetic subbands separated by the amount $\hbar\omega_o$. In order to observe the discrete nature of the Landau levels, their separation $\hbar\omega_o$ must be larger than $k_B T$ ($\hbar\omega_o >> k_B T$). Also, if the electronis are to exhibit quantum effects, they must complete orbits in k-space (in a plane perpendicular to the H field) before they are scattered. This requirement can be fulfilled by the condition $\omega_o \tau >> 1$ where $\tau$ is the relaxation time. The density of states per unit energy and unit volume (neglecting spin) is found to be [41]:

$$g(E) = \frac{1}{2}\left(\frac{1}{2\pi}\right)^2 \left(\frac{2m^*}{\hbar^2}\right)^{3/2} \sum_{n=0}^{n_{max}} \frac{\hbar\omega}{[E - (n+\frac{1}{2})\hbar\omega_o]^{1/2}} \qquad (2.24)$$

where $n_{max}$ is the quantum number for the highest occupied state. Equation 2.24 implies that the density of states diverges whenever the energy is equal to that of a Landau level. This divergence, which is due to neglecting the finite width of the Landau levels, vanishes if the effects of collision broadening are included [41, 45, 46]. If $\omega_o\tau$ is large ($1 << \omega_o\tau < \infty$), then oscillations in the density of states as a function of the magnetic field result. These oscillations have profound effects on the scattering rate of electrons, and hence on the transport properties. The physical origins of the oscillatory behavior may also be grasped by the following considerations.

Suppose a solid with electronic energy levels filled up to the Fermi level $E_F$ is placed in a varying magnetic field. As the magnetic field is increased, the separation $\omega_o = e\hbar H/m^*c$ between the Landau levels is also increased. In Fig. 2.11, the Landau levels corresponding to two different magnetic field values H and H' are schematically represented by n and n' with H' > H. We note that as the magnetic field is changed from H to H', the Landau level n = 3 which was fully occupied (because its energy is below $E_F$), is raised to n' = 3, which lies above $E_F$ and thus cannot be occupied. Hence, the electrons occupying the level n = 3 will have to redistribute themselves in the levels below $E_F$. This emptying of electrons from high magnetic subbands into lower ones is not a linear function of H and is particularly rapid when a Landau level passes through the Fermi level. As a result, there are resonances in the electronic (and magnetic) properties, such as maxima in resistivity, whenever the magnetic field values are such that $E_F$

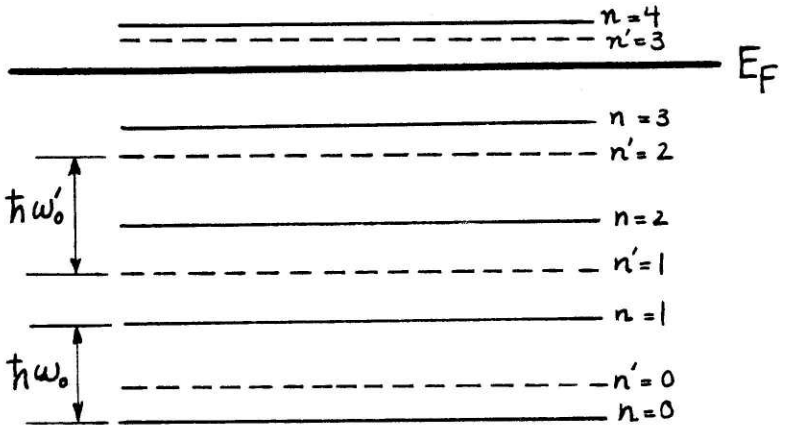


Figure 2.11

Schematic representation of the Landau levels and the Fermi level $E_F$. As the magnetic field H is increased, the separation between Landau levels $\hbar\omega_0 = e\hbar H/m^*c$ increases also. The passage of the Landau level n = 3 through $E_F$ causes redistribution of the occupied states, and hence resonances in the electronic properties.

coincides with one of the Landau level extrema. If the field is swept continuously then these extrema correspond to oscillations which are periodic in $H^{-1}$, with the period of oscillations given by:

$$\Delta\left(\frac{1}{H}\right) = \frac{\hbar e}{m^* c}\,\frac{1}{E_F} = \frac{\hbar e}{m^* c}\,\frac{1}{(\hbar^2 k_F^2/2m^*)} = \frac{2\pi e}{\hbar c}\,\frac{1}{\pi k_F^2} \quad \frac{2\pi e}{\hbar c}\,\frac{1}{A} \tag{2.25}$$

In this expression, substitutions $E_F = \hbar k_F^2/2m^*$ and $A = \pi k_F^2$ are made for the simplest model of a solid. A is the maximum cross-sectional of the (spherical) Fermi surface. For a Fermi surface of general shape, the above result has been generalized [47]. In fact, in the case of an arbitrarily shaped Fermi surface, only the extremal cross sections contribute to observable quantum oscillations and the effects of other parts of the Fermi surface interfere destructively. Equation 2.25 can therefore be written more generally as:

$$\Delta\left(\frac{1}{H}\right) = \frac{2\pi e}{\hbar e}\,\frac{1}{A_{extr.}} \tag{2.26}$$

where $A_{extr.}$ is the extremal cross-sectional area of the Fermi surface perpendicular to the magnetic field.

Relation 2.26 can also be obtained by quantitative and rigorous calculations [41,45]. The result of such calculations for conductivity in thd presence of a magnetic field can be summarized as [45,46]:

$$\sigma(H) = \sigma_{bgnd.} + \sigma^{(1)}_{oscil.} + \sigma^{(2)}_{oscil.} \tag{2.27}$$

where $\sigma_{bgnd.}$ is the background magnetoconductivity which is proportional

to $H^{-2}$, and $\sigma^{(i)}_{oscil.}$ are given by:

$$\frac{\sigma^{(1)}_{oscil.}}{\sigma_{bgnd.}} \propto \left(\frac{\hbar\omega_o}{E_F}\right)^{1/2} \sum_r \frac{(-1)^r (2\pi^2 r k_B T/\hbar\omega_o)}{(2\pi r)^{1/2} \sinh(2\pi^2 r k_B T/\hbar\omega_o)} \exp\left(\frac{-2\pi}{\omega_o \tau_c}\right) \cos\left(\frac{2\pi r E_F}{\hbar\omega_o} - \frac{\pi}{4}\right) \tag{2.28}$$

$$\frac{\sigma^{(2)}_{oscil.}}{\sigma_{bgnd.}} \propto \left(\frac{\hbar\omega_o}{E_F}\right) \sum_r \frac{(-1)^r (2\pi^2 r k_B T/\hbar\omega_o)}{\sinh(2\pi^2 r k_B T/\hbar\omega_o)} \exp\left(\frac{-2\pi}{\omega_o \tau_c}\right) \cos\left(\frac{2\pi r E_F}{\hbar\omega_o} - \frac{\pi}{2}\right) \tag{2.29}$$

The symbols in the above expressions are as referred to previously. The collision time $\tau_c$ is in general different from the relaxation time [45]. We see that there are oscillations in conductivity as a function of H-field ( $\omega_o = eH/m^*c$) due to the cosine terms, while their amplitudes are exponentially damped by the sinh terms. The oscillations have harmonics ($r > 1$), but the amplitudes of the harmonics are also damped exponentially. The period of oscillations (for the $r^{th}$ harmonic) can be deduced from the argument of the cosine term as:

$$\text{Period} = \frac{(e\hbar/m^*c)}{E_F} = \frac{2\pi e}{\hbar c} \frac{1}{r} \frac{1}{A} \tag{2.30}$$

which is in agreement with the result previously obtained from qualitative arguments --- see Eq. 2.25.

In Eqs. 2.28 and 2.29 the effect of collision broadening at the finite (non-zero) temperature T is taken into account by the exponential damping factor. The collision time $\tau_c$ may also be written as $(\hbar/\pi k_B T_D)$, where $T_D$ is called the "Dingle temperature". From the field dependence of the amplitude of the oscillations, $T_D$ (or $\tau_c$) can be measured experimentally. Note that in order to observe the oscillatory terms in the

conductivity, the damping terms must be reasonably small -- i.e., $k_B T << \hbar\omega_o$ and $\omega_o \tau_c >> 1$, as mentioned previously. In order to appreciate the magnitude of field intensity and temperature required to satisfy these requirements, consider the following:

$$\text{At:} \left\{ \begin{array}{l} H = 10 \text{ Tesla} \\ T = 1^\circ K \end{array} \right\} \Rightarrow \quad \frac{\hbar e H}{m^* c} \qquad\qquad k_B T$$

$$\downarrow \qquad\qquad \downarrow$$

$$\sim (m_o/m^*) \times 3 \times 10^{-3} \text{ eV} \qquad \sim 10^{-3} \text{ eV}$$

Thus, we see that high magnetic field, low temperature are necessary and small effective masses are advantageous for the observation of oscillatory magnetoresistance.

To summarize, in the Shubnikov-de Haas experiment, the resistivity of the material is measured at low temperature as a function of high magnetic field, H. One can then relate the frequency(ies), or period(s) of the oscillations (which are periodic in $H^{-1}$) to the extremal cross sections of the Fermi surface perpendicular to H through:

$$A^{(i)}_{extr.} = \frac{2\pi e}{\hbar c} \nu^{(i)}_{SdH} = 0.9546 \times 10^{12} \nu^{(i)}_{SdH} \qquad (2.31)$$

where $A^{(i)}_{extr.}$ has units of $cm^{-2}$ if $\nu^{(i)}_{SdH}$ is expressed in Tesla.

Further information about the Fermi surface can be obtained by studying the angular and temperature dependence of the SdH results. By changing the direction of the field relative to the crystalline axes, it is possible to map the shape of the Fermi surface. Figure 2.12 illustrates this point schematically. The temperature-dependent SdH measurements are used to obtain the effective masses of the carriers at the

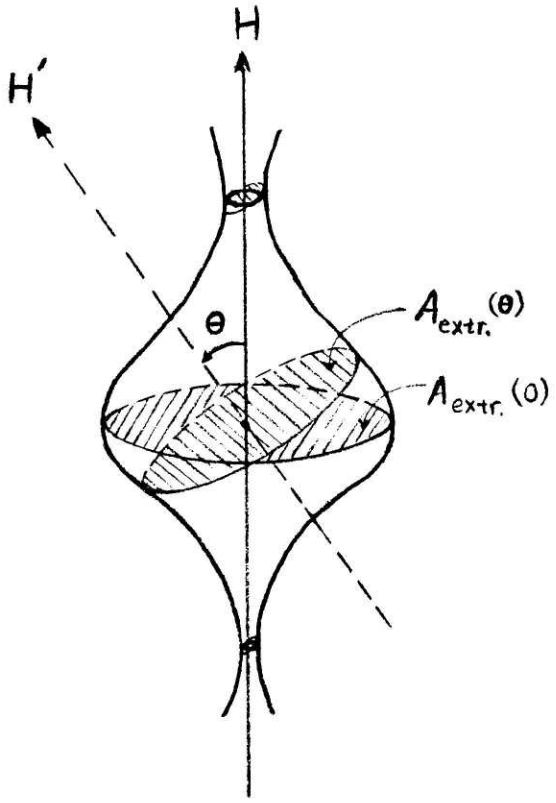


Figure 2.12

A sketch of a hypothetical Fermi surface is shown, with its extremal cross-sectional areas (shaded areas) perpendicular to the direction of the magnetic field, H. By performing the SdH experiment on the sample as the angle $\theta$ is varied, and relating the frequency(ies) of oscillation to the cross-sectional areas $A^{(i)}_{extr.}$ (see Eq. 2.31), one can study the topology of the Fermi surface.

Fermi surface. To see this, consider the temperature-dependent terms in Eqs. 2.28 and 2.29. Note that the amplitude of the oscillations depends on temperature. For r = 1 (main frequency) the amplitude goes as:

$$\mathcal{A} \propto T \exp(2\pi^2 k_B T/\hbar\omega_o) = T \exp(2\pi^2 k_B T m^* c/\hbar e H) \qquad (2.32)$$

Based on Eq. 2.32, a common way to extract the effective mass m* is to plot $\ell n\,(\mathcal{A}/T)$ as a function of temperature. Here, the amplitude $\mathcal{A}$ must be measured at some fixed value of the field $H_o$ for several temperatures. According to Eq. 2.32, the resulting plot is a straight line with the effective mass being inversely proportional to its slope:

$$\frac{m^*}{m_o} = \frac{\ell n(\mathcal{A}/T)}{T} \quad \frac{\hbar e}{2\pi^2 k_B m_o c} H_o = \frac{|S|}{14.694} H_o \qquad (2.33)$$

where $m_o$ is the electron rest mass and S is the slope ($\mathcal{A}$ is measured in arbitrary units, while S is in $^\circ K^{-1}$ and $H_o$ is in Tesla).

The above analysis leading to Eq. 2.33 assumes that the amplitude $\mathcal{A}$ corresponds to oscillations of a certain single frequency. If oscillations of more than one frequency are present, then the above analysis should be done cautiously, since the measured amplitude is a result of the interference of the oscillations of two or more frequencies. These different frequencies correspond to different cross sections of the Fermi surface and are likely to have different effective masses.

This point will be discussed further in Chapter V, where the analysis of data is presented.

# III. SAMPLE PREPARATION

The starting point for these measurements was the growth and characterization of the alkali-metal graphite intercalation compounds (GIC). In section 3.1 of this chapter, details of the two-zone growth process are discussed, while section 3.2 deals with the X-ray characterization ($\theta$ - $2\theta$ diffractometer scans) of the intercalated samples.

## III-1. Sample Growth

The samples used in this study were all grown using highly oriented pyrolytic graphite (HOPG) as the host crystal. Blocks of HOPG were cut (parallel to the c-axis) to the desired size [see Fig. 3.1(a)] using a string saw. Once cut to the right a-plane dimensions, the blocks were cleaved perpendicular to the c-axis to obtain thin ($\sim$ 1mm thick) samples. They could then be made even thinner by peeling them using Scotch Tape [Fig. 3.1(b)]. This peeling is essential when samples of high (a-palne) resistance are needed. The thin and long samples [type B in Fig. 3.1(b)] were particularly grown to improve the SdH magnetoresistance signal-to-noise ratio (Chap. IV) and are recommended for these measurements.

The two-zone vapor transport method [48-51] was used to grow the samples. In this method, the intercalant and the graphite crystal are heated in an evacuated ampoule to two different temperatures ($T_g > T_i$) while they are separated in distance. In this study, one or more of the host HOPG crystals was placed at one end of a prepared reaction vessel containing the alkali-metal in a sealed ampoule [Fig. 3.2(a)].

The vessel is then vacuum-pumped to $\sim$ 10 millitorr and sealed at the open end [Fig. 3.2(b)]. The break seal shown in Fig. 3.2(a) is then broken, using a steel hammer. The reaction vessel thus prepared is put in the furnace (Lindberg ). A coil ($R \sim 100\,\Omega$) powered by a variac

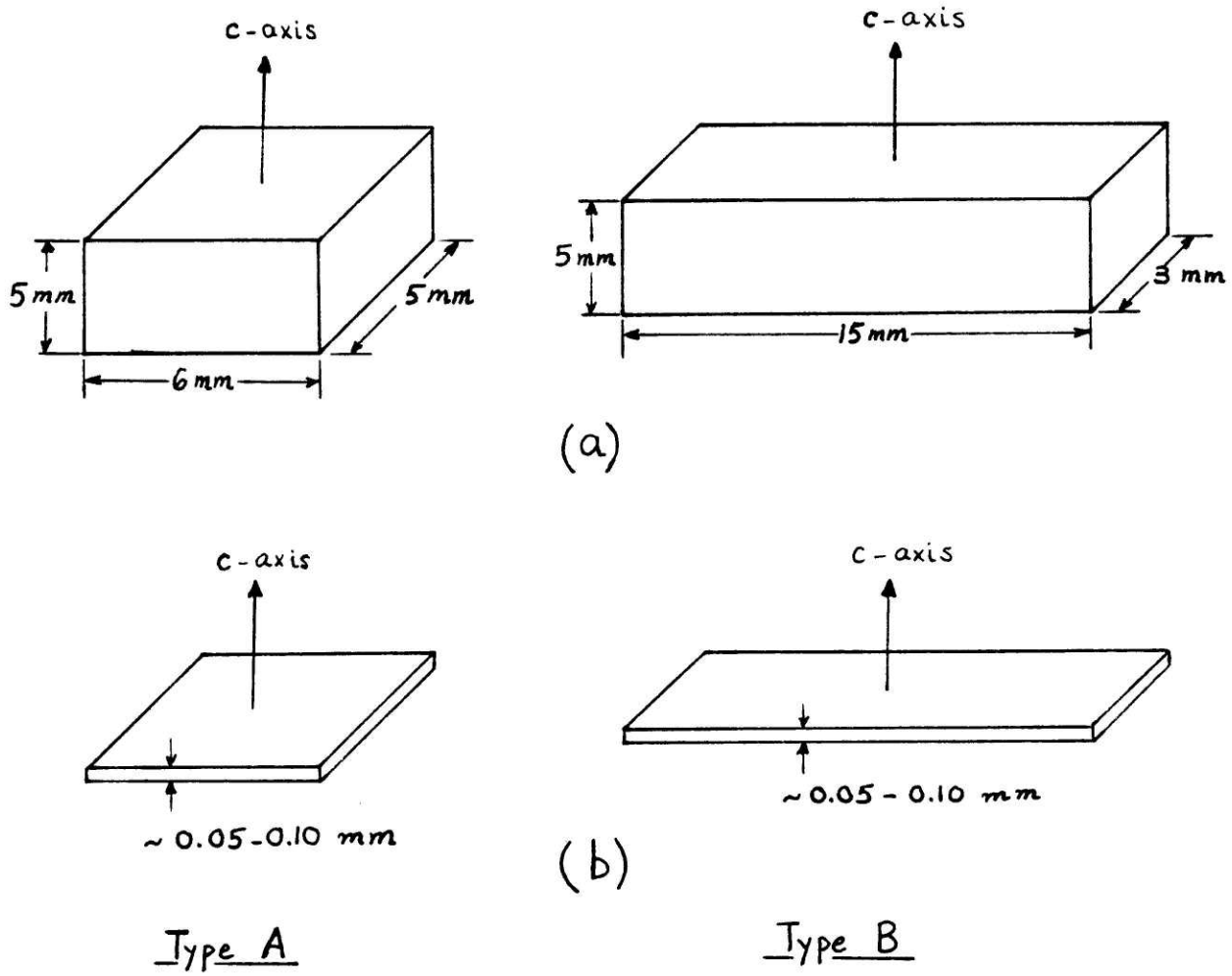


Figure 3.1

HOPG blocks cut parallel to c-axis, using a string saw, are shown in (a). These blocks were then cleaved perpendicular to the c-axis and peeled to obtain very thin ($\sim$ 0.05mm thick) samples (b). Type A and type B samples, which are referred to in the text, are shown in (b).

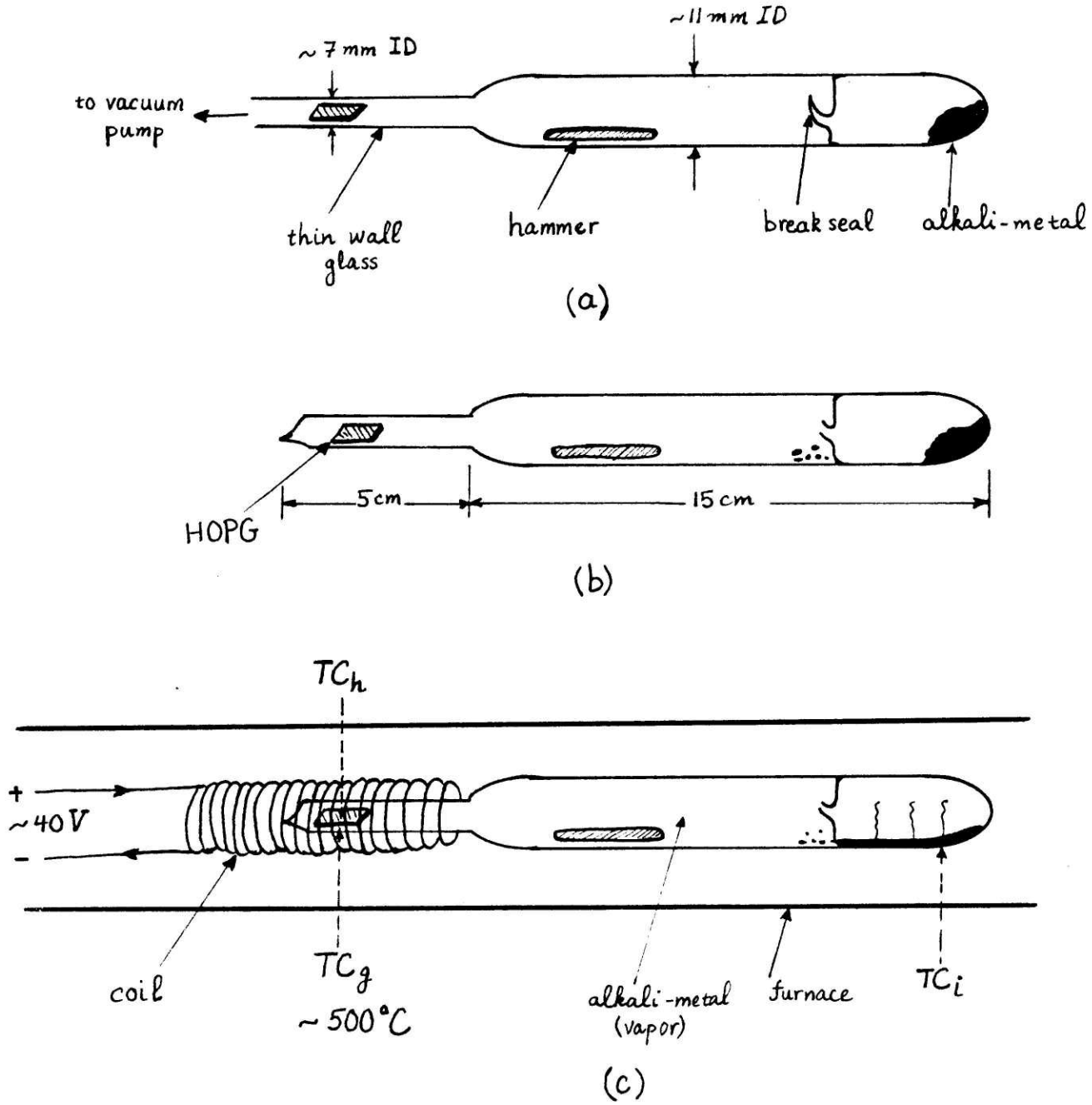


Figure 3.2

Schematic diagram of the system used for the preparation of alkali-metal GIC.

a) The reaction vessel containing the alkali-metal at a sealed end.
b) The break seal is broken using the glass-encapsulated steel hammer after the reaction vessel is evacuated.
c) Position of the reaction vessel in the furnace.

is used as the hot zone ( $\sim$ 500°C), while the main furnace is set for $\sim$220-320°C depending on the stage of the sample. The position of the ampoule in the furnace is shown in Fig. 3.2(c). Three thermocouples are used: $TC_g$ adn $TC_i$ monitor the temperatures of the graphite host crystal $T_g$, and the intercalant metal, $T_i$, respectively. The third thermocouple $TC_h$ also reads the hot-zone temperature, and together with a temperature controller (Omega) work as the feedback to the variac.

The samples were prepared by keeping $T_g$ constant ( $\sim$ 500°C) and varying $T_i$ for different stages. Over 20 samples (K and Rb) were made ($2 \leq n \leq 8$) using this method. The main parameter which determines the stage is the temperature difference $\Delta T = T_g - T_i$, with larger $\Delta T$ resulting in higher stage. Other important parameters are ampoule and sample shape and size, while less important is the amount of alkali-metal in the ampoule (as long as this amount is larger than the minimum amount needed for a desired stage.*) The time needed for the intercalation process is only a few hours; however, as a matter of convenience, samples were usually left in the furnace overnight, hence the times used were 12-24 hours. In Table 3.1, the growth parameters for some of the typical samples are given. It must be emphasized that these parameters should be used only as guidelines in growing samples. During this study, in numerous cases when the right $\Delta T$ for a given stage n was used, the sample turned out to be a stage n sample mixed with either stage n-1 or n+1. In such cases, it is possible to put the reaction vessel back in the furnace and raise (when mixed with n-1) or lower (when mixed with n+1) $\Delta T$, to obtain a single stage sample. A

---

* Since alkali-metals, especially potassium, attack glass when in the vapor phase, it is necessary to start with more alkali-metal than needed. In this study $\sim$.1 gram was used for each ampoule, which was sufficient for intercalating up to 3 samples of mentioned sizes ($n \geq 2$).

| Sample | Type | Intercalant | $T_g$(°C) | $T_i$(°C) | $\Delta T$(°C) | Time(hrs.) | Stage |
|---|---|---|---|---|---|---|---|
| K02.Y10 | A | K | 469 | 319 | 150 | 18 | 2 |
| K02.Y13 | A | K | 510 | 339 | 171 | 12 | 2 |
| K02.W14 | B | K | 488 | 323 | 165 | 18 | 2 |
| K02.Y14 | B | K | 500 | 305 | 195 | 48 | 2 |
| K02.Y15 | B | K | 486 | 300 | 186 | 48 | 2 |
| K03.Y05 | A | K | 493 | 277 | 216 | 19 | 3 |
| K03.W15 | B | K | 502 | 271 | 231 | 48 | 3 |
| K03.Y16 | B | K | 494 | 262 | 232 | 18 | 3 |
| K04.W04 | A | K | 466 | 235 | 231 | 18 | 4 |
| K04.W16 | B | K | 486 | 247 | 239 | 17 | 4 |
| K05.Y03 | A | K | 481 | 230 | 251 | 16 | 5 |
| K05.W17 | B | K | 475 | 234 | 241 | 17 | 5 |
| R02.W08 | A | Rb | 450 | 261 | 189 | 36 | 2 |
| R04.W09 | A | Rb | 476 | 225 | 251 | 24 | 4* |
| R05.W09 | A | Rb | 470 | 200 | 270 | 1 | 5 |
| R08.Y01 | A | Rb | 505 | 140 | 365 | 24 | 8 |

*Same sample put back in the furnace.

Table 3.1

Reaction times and temperatures used for growing various compounds. Types A and B refer to the dimensions shown in Fig. 3.1(b).

detailed example of such a process is shown in Fig. 3.8.

Figures 3.3 and 3.4 summarize the temperature differences used to grow samples with different stages. Included in these figures are the data of D. E. Nixon [48] and C. Underhill [51] who used a similar method. The lines through the experimental points indicate that a given stage (especially $n < 5$) can be prepared for a range of $\Delta T$ values. Figure 3.3 also indicates that, for a given stage, $\Delta T$ is larger for type B samples.

One general comment about sample growth is that, since growing single-stage samples is a time-consuming process, it is useful to start with two or three host crystals in the reaction vessel. This was done, especially in the case of type B samples, and proved to be very efficient.

III-2. Sample Characterization

In order to characterize the graphite intercalation compounds, several techniques, such as weight uptake, visual inspection, chemical analysis, X-ray diffraction and electron microscopy are used. For qualitative information, sample color (observed by visual inspection) and weight uptake (change in the weight of graphite crystal upon intercalation) can be used. In the case of alkali-metal GIC's, a yellow or gold color is characteristic of stage 1, steel blue for stage 2, dark blue for stage 3, and graphite metallic for higher stages [49, 52]. Visual inspection, however, is not capable of identifying mixed-stage samples and samples of stages higher than 3. The weight uptake measurement provides information about the sample stage if a chemical formula is

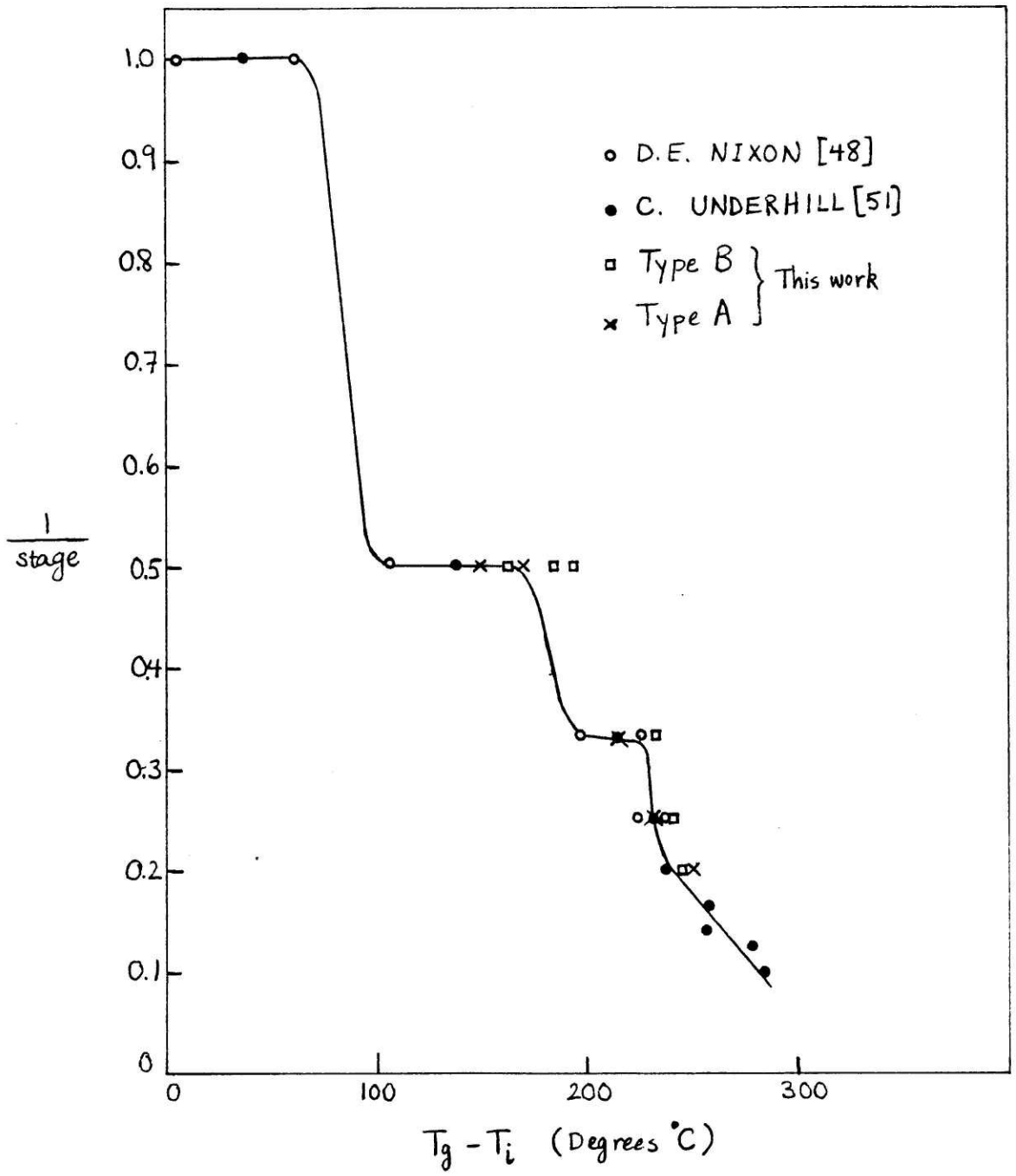


Figure 3.3

Isobar diagram showing 1/stage versus temperature difference between sample ($T_g$) and intercalant ($T_i$) for graphite-potassium compounds.

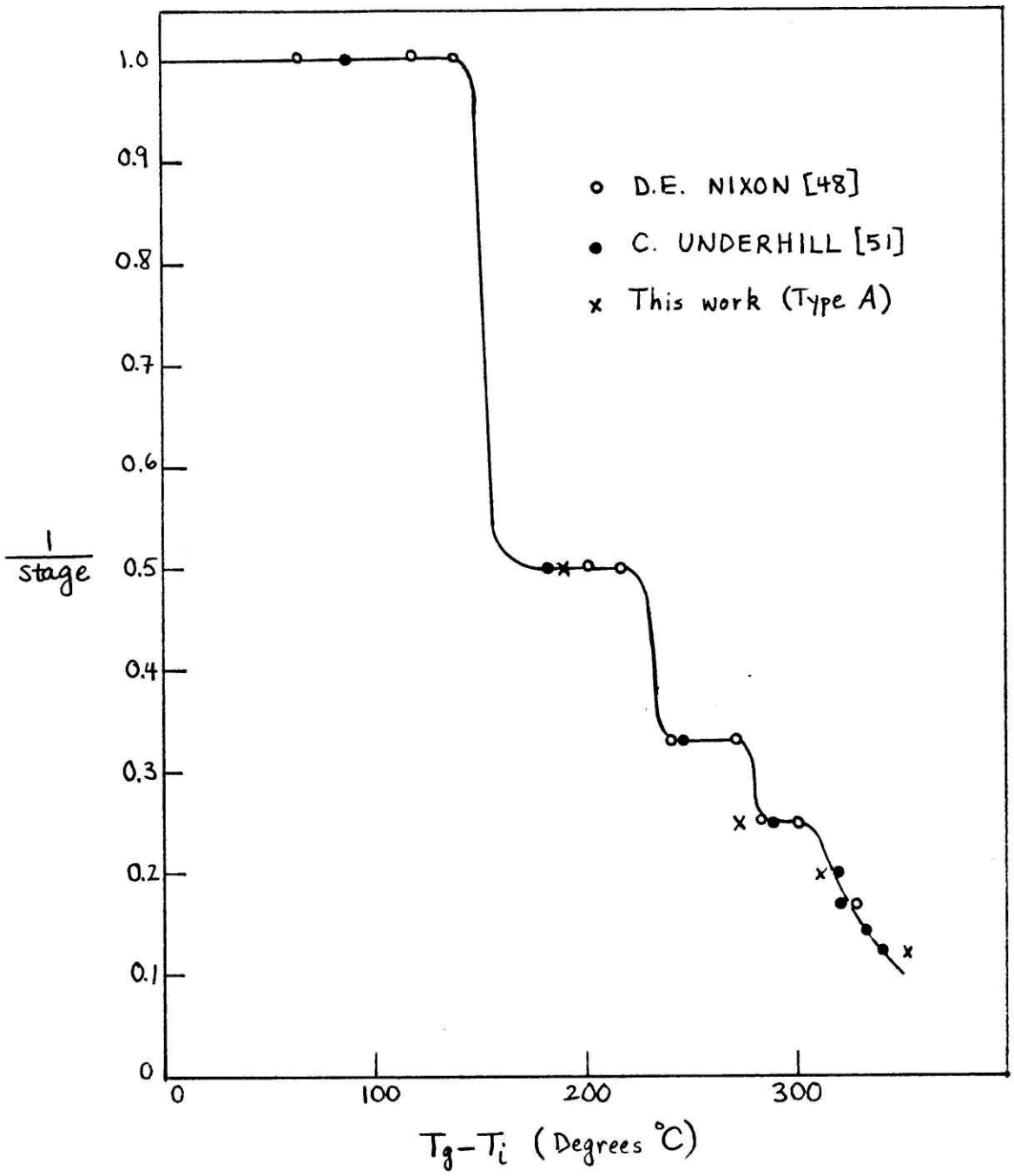


Figure 3.4

Isobar diagram showing 1/stage versus temperature difference between sample ($T_g$) and intercalant ($T_i$) for graphite-rubidium compounds.

known for the compound. However, because of sample inhomogeneity and the presence of intercalate vacancies/accumulations in preferred crystal defect sites, this information is only qualitative. X-ray diffraction measurements, on the other hand, give quantitative information about the stage as well as the in-plane structure of the compounds.

Since the reported results on the Fermi surface of Potassium-GIC [5] indicated a significant stage-dependence for the Fermi surface, it was necessary to grow and preserve single-stage samples for these measurements. Hence, X-ray diffraction using (00$\ell$) reflections was used for accurate determination of the stage of the samples.

Figure 3.5 shows the system used in this study for the X-ray measurements. The position of the sample in the X-ray beam is shown more clearly in Fig. 3.6. The incoming X-ray beam makes an angle ($\theta$) with the c-face of the sample. The detector is rotated in such a way that it always makes angle $2\theta$ with the incoming beam ($\theta$-$2\theta$ diffractometer). The X-ray diffractogram is obtained by scanning angle $\theta$ (usually from 1° to $\sim$40°) and recording the output of the detector. The stage index can be found from $I_c$, the intercalate (c-axis) repeat distance (see Fig. 2.2), which is itself determined from the diffraction angles $\theta_\ell$ for the (00$\ell$) diffraction peaks. The angles $\theta_\ell$ are given by Bragg's law:

$$\ell\lambda = 2I_c \sin\theta_\ell \quad ,$$

where $\ell$ takes positive integer values and $\lambda$ is the wavelength of the X-ray beam. Molybdenum-K$\alpha$ radiation was used so that the X-ray absorption by the glass encapsulating the samples is minimized. As shown in Fig. 3.5(b), the Si(Li) detector is sensitive to the continuum

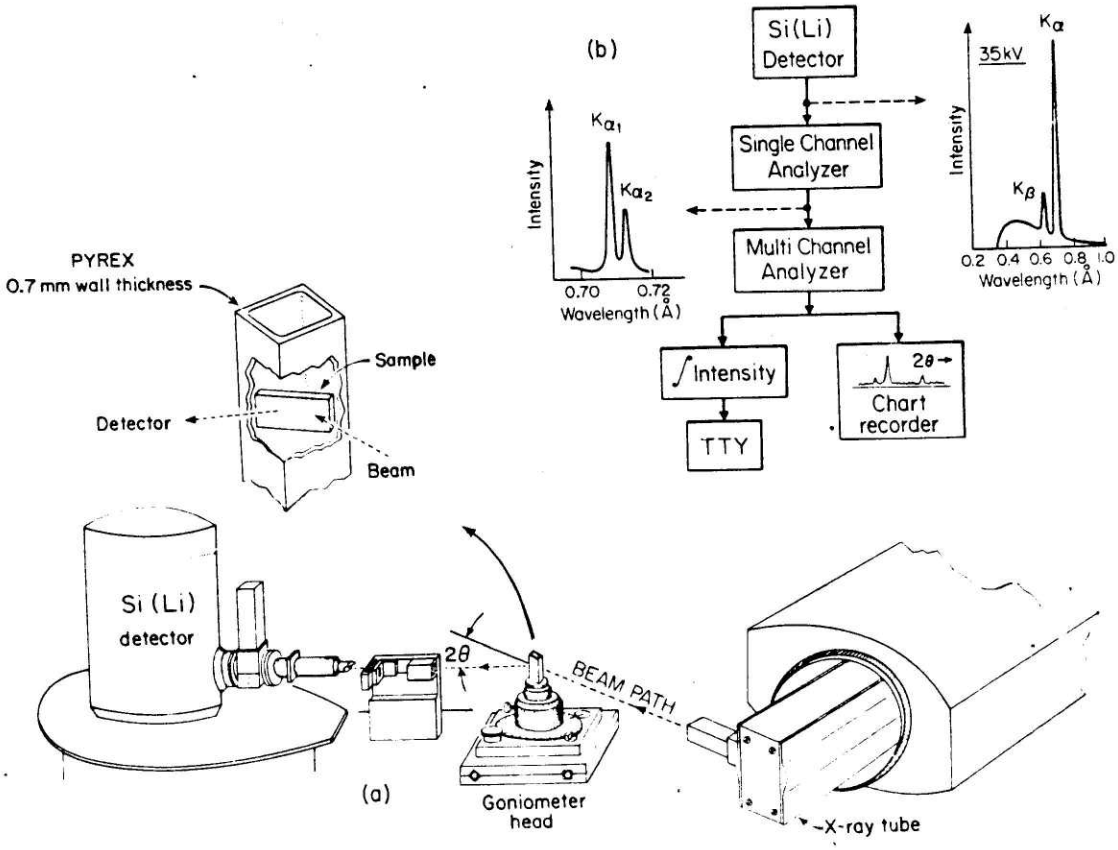


Figure 3.5

X-ray system for (00ℓ) diffractometer scans. $K_\alpha$ radiation from a Mo X-ray source is incident on the sample and the diffracted beam is detected by a cooled Li-drifted detector. The detector permits high resolution energy discrimination of the diffracted beam. The energy windows of the single-channel analyzer are set so that only signals corresponding to $K_{\alpha 1}$ and $K_{\alpha 2}$ radiation are processed. The multichannel analyzer is used for data acquisition of (00ℓ) diffractograms [50].

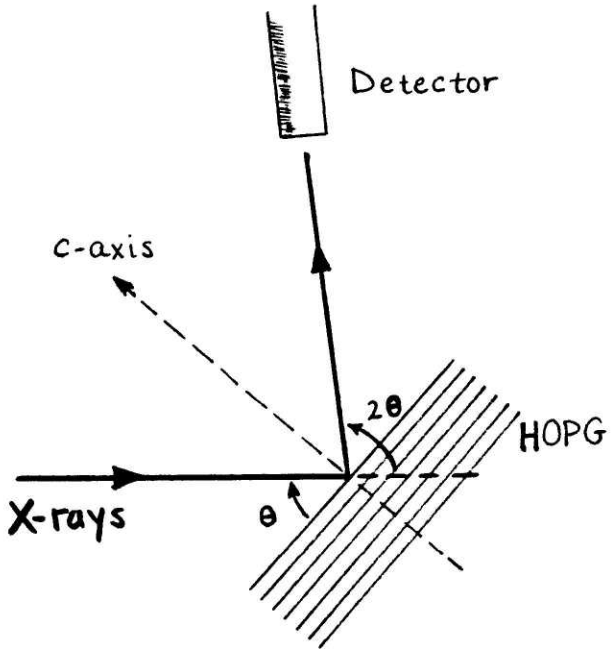


Figure 3.6

Geometry for measurement of X-ray (00ℓ) reflections from intercalation compounds based on single-crystal and highly oriented pyrolytic graphite host materials.

of energy radiated by the Mo source. A single-channel analyzer works as the energy window, and when properly set, singles out the Kα radiation ( $\lambda = 0.7107\text{Å}$)*. The multi-channel analyzer shown in Fig. 3.5(b) is used to make several measurements such as θ - 2θ scans or the integrated intensity measurements. Examples of θ - 2θ diffractograms are shown in Fig. 3.7 for potassium compounds of stages 2, 3, and 4.

Previous work [50,52,54] as well as present work has shown that graphite interlayer separation is essentially unaffected upon intercalation. Thus, the stage index n is found from the relation:

$$I_c = nc_o + d = (n-1)c_o + d_s,$$

where $c_o$ is the distance between adjacent graphite layers, and $d_s = c_o + d_i$ is the distance between two graphite bounding layers. Analysis of (00ℓ) diffractograms have shown also that $d_s$ and $c_o$ are essentially independent of stage for a given intercalant [48,52,54].; $c_o$ remains equal to 3.35Å (as in pristine graphite) and $d_s$ is 5.35Å for potassium [48] and 5.65Å for rubidium [1,2,51]. With this information, the expected positions of the X-ray diffraction peaks for different stage compounds can be predicted. Using the above values for $c_o$ and $d_s$, and $\lambda = 0.7107\text{Å}$, we have listed the $2\theta_\ell$ angles for several ℓ values in Table 3.2 for graphite-potassium compounds of several stage indices.

---

* Molybdenum in fact has $K\alpha_1$ ($\lambda = 0.70930\text{Å}$) and $K\alpha_2$ ($\lambda = 0.71359\text{Å}$) radiation. The value $\lambda = 0.7107\text{Å}$ is the weighted average of the two wavelengths [53]. Diffraction peaks corresponding to these two wavelengths can sometimes be resolved at high $\theta_\ell$ angles.

| | K-Stage-2 | | K-Stage-3 | | K-Stage-4 | |
|---|---|---|---|---|---|---|
| | | | $2\theta_\ell$ (Degrees) | | | |
| $\ell$ | Obs. ($\pm 0.10^\circ$) | Calc. | Obs. ($\pm 0.10^\circ$) | Calc. | Obs. ($\pm 0.10^\circ$) | Calc. |
| 1 | 4.64 | 4.68 | 3.38 | 3.38 | 2.66 | 2.64 |
| 2 | 9.35 | 9.37 | 6.77 | 6.76 | 5.31 | 5.29 |
| 3 | 14.08 | 14.08 | 10.16 | 10.15 | 7.99 | 7.94 |
| 4 | 18.85 | 18.81 | 13.55 | 13.55 | 10.60 | 10.59 |
| 5 | 24.60 | 23.57 | 17.02 | 16.96 | 13.28 | 13.25 |
| 6 | 28.39 | 28.37 | - | 20.38 | 15.92 | 15.92 |
| 7 | - | - | 23.86 | 23.83 | 18.61 | 18.59 |
| 8 | - | - | 27.24 | 27.29 | - | 21.27 |
| 9 | - | - | - | - | 23.94 | 23.97 |

Table 3.2

Comparison between observed and calculated $2\theta_\ell$ angles for K-GIC (stages 2,3,and 4). The very good agreement indicates that the assumpitons made in the calculation of $2\theta_\ell$ ($c_o$=3.35Å and $d_S$=5.35Å, both stage-independent) are valid.

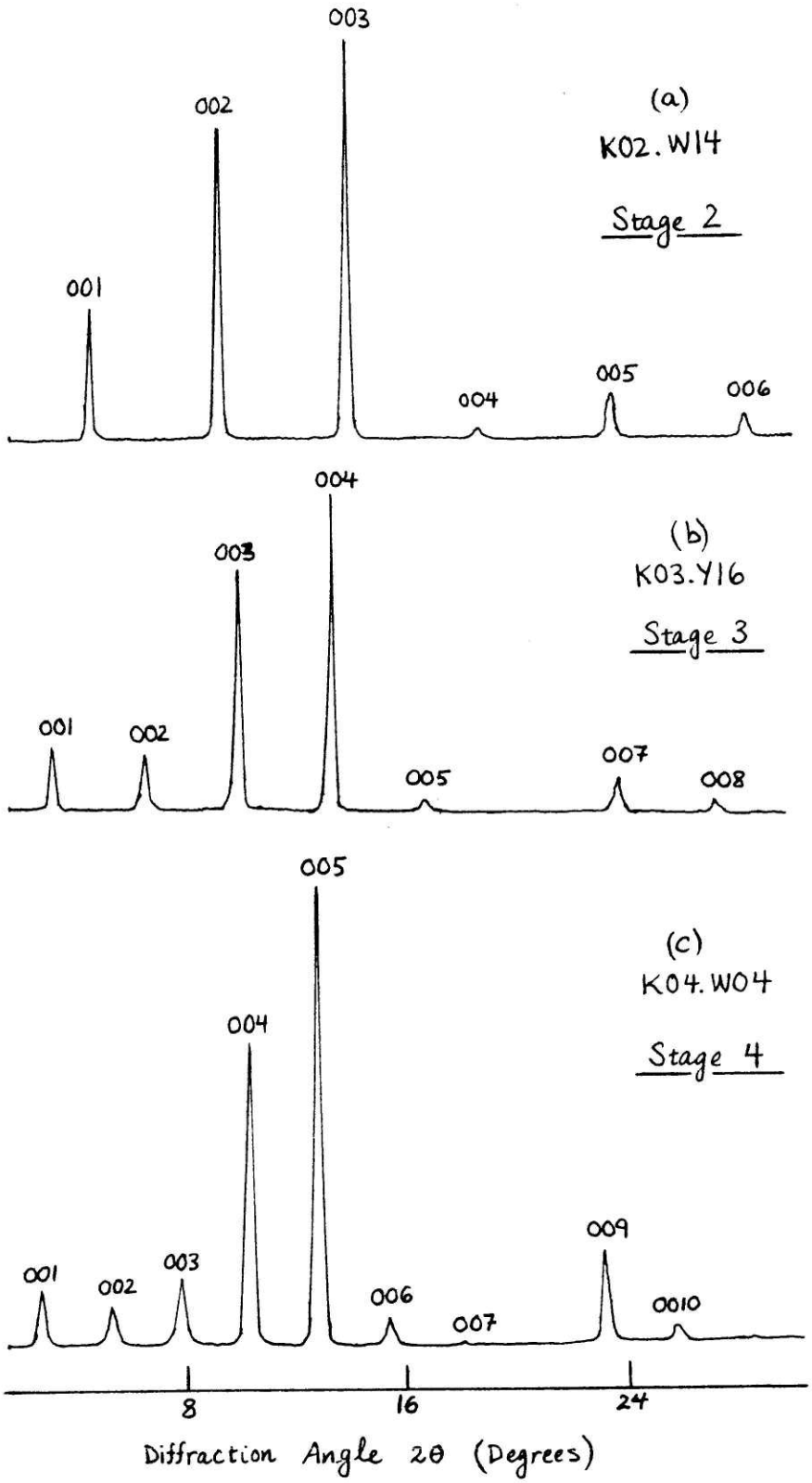


Figure 3.7

X-ray stage characterization using (00ℓ) diffractograms for stages 2, 3, and 4 graphite-K compounds.

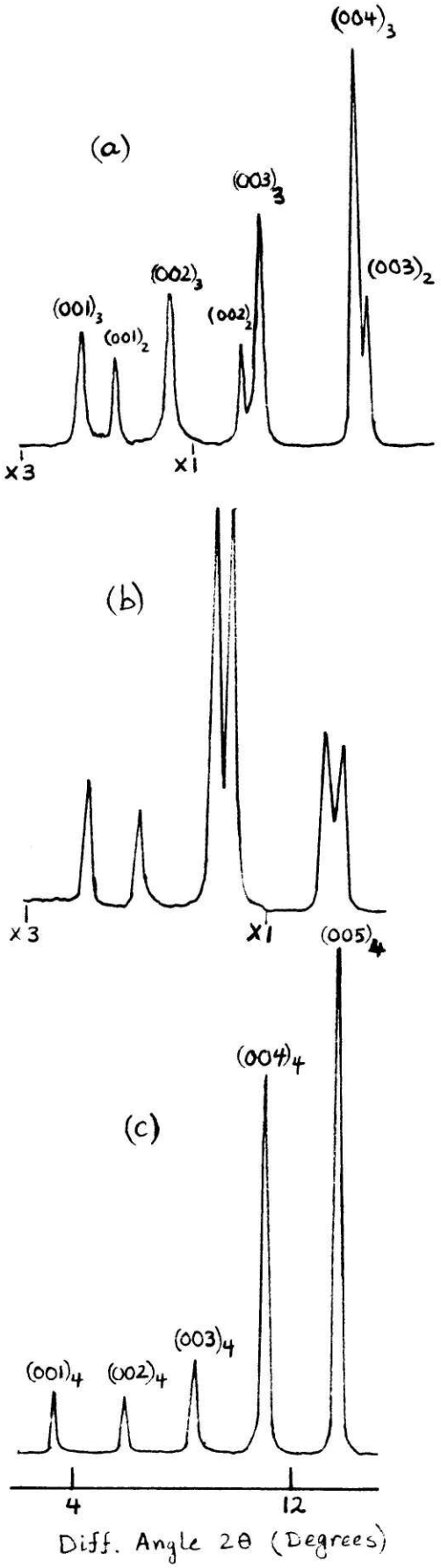


Figure 3.8

X-ray diffractogram showing how "recooking" can be used to change a sample of mixed stages 2 and 3 (a) to a mixed 3 and 4 (b), and finally to a sigle stage 4 sample (c).

For comparison, the peak positions (2 $\theta_\ell$ values) observed for some of the samples are tabulated together with the calculated values (Table 3.2). The very good agreement between the observed and calculated angles indicates that the assumption is indeed valid that the $d_s$ and $c_o$ values are stage-independent and are equal to the above-mentioned values.

The structure factor analysis shows that the index $\hat{\ell}$ of the reflection with maximum peak intensity (00$\hat{\ell}$) for K and Rb compound of stage n is given by $\hat{\ell} = n + 1$ [54]. Also, the separation between consecutive peaks increases with decreasing stage.

To obtain accurate X-ray data, sample alignment is critical. A fast method for aligning the sample is as follows:

a) Initially, place the sample at the goniometer head (Fig. 3.5) such that the c-axis is parallel to the horizontal plane and is also perpendicular to the beam when $\theta = 0°$. Visual alignment is sufficient at this step.

b) Set $2\theta$ to $\sim 13°$ (maximum intensity of the envelope function) and maximize the reflected beam (detector output) by using the goniometer to rotate and translate the sample. Thus, the main (00$\ell$) peak can be roughly found.

c) Once this peak is found, a fast scan for angles $2\theta \lesssim 13°$ can be taken and the stage of the sample can be determined by either counting the number of peaks below the main (00$\hat{\ell}$) one, or by measuring the separation between two neighboring peaks (Table 3.2).

d) Now $2\theta$ can be set exactly equal to the $2\theta\hat{\ell}$ angle for the given stage (Table 3.2, *e.g.*) and the sample can be realigned using the goniometer so that the main peak appears precisely at this $2\theta$. A new and accurate diffractogram can now be obtained.

e) Finally, the position and width of the peaks can be measured and compared to the calculated/expected values; thereby it can be judged whether the sample is single-stage or consists of mixed stages.

Note that in Fig. 3.7, the full widths at half maximum (FWHM) intensity for the intercalation compounds are roughly equivalent to those of pristine graphite. Typical FWHM values for the most intense $(00\hat{\ell})$ peaks are $\sim 0.2°$ to $0.3°$. In the case of samples of mixed stages, the X-ray diffractograms show a superposition of the $(00\ell)$ peaks for the two stages present in the sample (Fig. 3.8), but these peaks are usually broadened relative to those from a single-stage compound. The existence of such fairly well defined patterns is compatible with the presence of macroscopic regions that exhibit stage n and other macroscopic regions with different stages (n+1 or n-1).

The X-ray $(00\ell)$ diffraction measurements can provide more information than just the stage of the sample. For example, the intensities of the peaks, using structure factor analysis, provide detailed information about the internal structure of the intercalate layer [54]. In this work however, the X-ray technique was used mainly to determine the stage of the sample at different steps of the experiments. No strong correlation was found between

the quality of the X-ray traces, such as the width of the peaks, and the SdH periods for single-stage compounds. However, the SdH oscillations were usually very hard to observe for samples of mixed stages, and single-stage samples were needed to give good SdH results.

# IV. DETAILS OF THE SDH EXPERIMENT

In this chapter the details of the SdH experiment will be presented. In section 4.1, we will explain how the leads were attached to the sample for the electrical resistivity ($\rho$) measurements. Section 4.2 illustrates the geometry of the experiment and the last section deals with data acquisition and analysis.

## IV-1. Mounting the Sample

In order to do the resistivity measurements, the four-point probe method was used. In this method, four leads are connected to the corners of the sample and the voltage drop across two of these is measured, while a current flows through the other two [Fig. 4.1(a)]. This method is not the most suitable one for resistivity measurement of highly anisotropic materials and corrections have to be made to obtain correct values of the resistivity and Hall tensors [55,56]. In the case of the SdH experiment, however, the anisotropy of the solid, or the non-uniformity of the injected current, pose no problem - since we are interested only in the change in conductivity as the magnetic field is varied; neither the uniformity of the current nor the anisotropy of the material is a function of the magnetic field.

Because of the instability of the alkali-metal samples in the presence of the air and moisture, the samples had to be handled in a dry box (Argon filled with $\lesssim 1$ pmm oxygen content). Since this handling in the dry box was physically the hardest, as well as the most crucial step of the experiment, a detailed description of this aspect of the

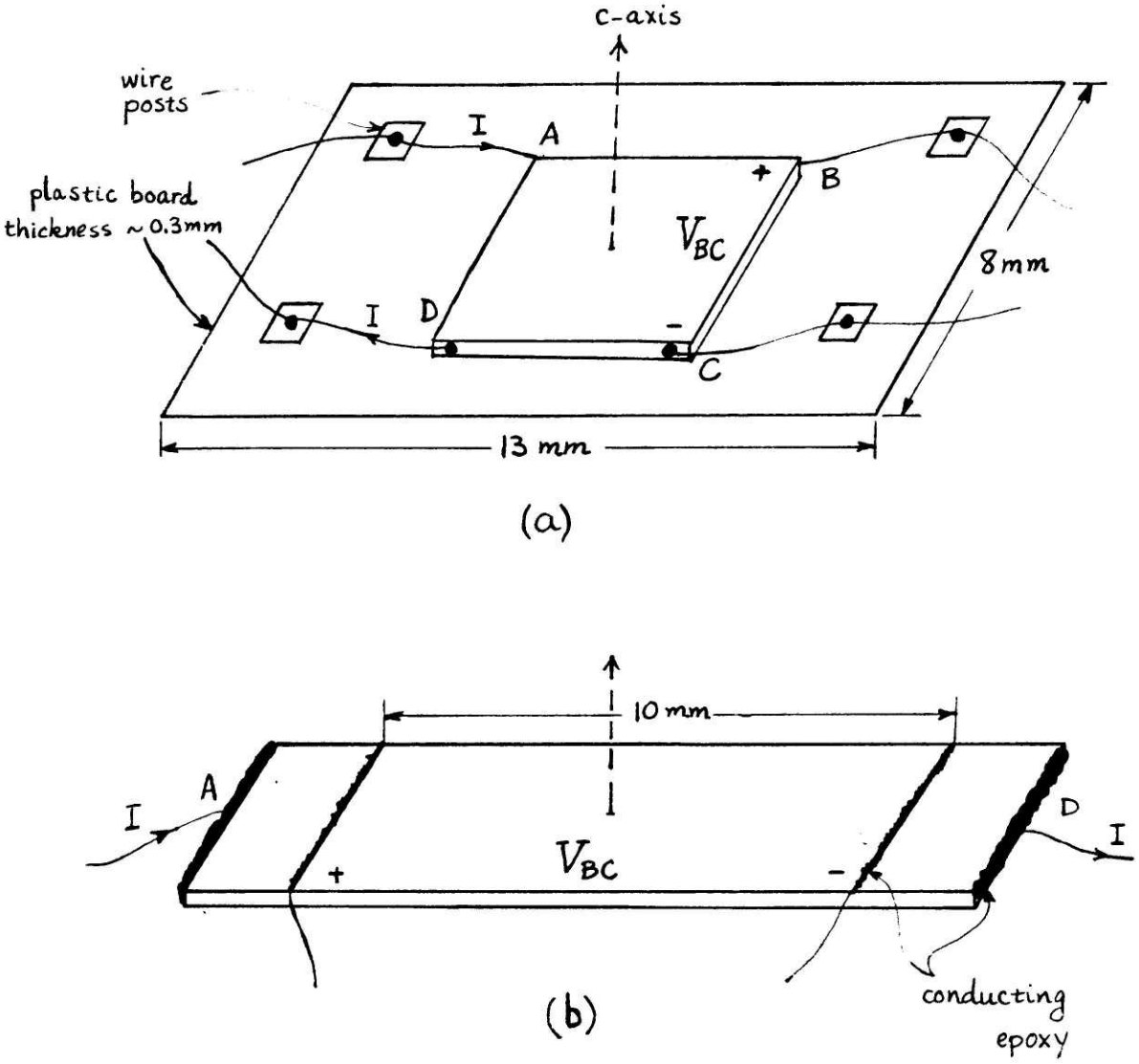


Figure 4.1

(a) Geometry for the four-point probe method. Resistance is measured by measuring the voltage $V_{BC}$ while a known current I flows from A to D.

(b) Another geometry for sample and contacts for the resistivity measurements. Again, $V_{BC}$ is measured as current I flows through AD.

experiment will be presented here.

Usually, on the day before the experiment, two or three reaction vessels containing grown samples were transferred to the dry box. Small boards [Fig. 4.1(a)] with contact posts and wires attached to these posts were prepared in advance and transferred to the glove box. (Contact posts were made by printed circuit techniques.) The magnet wires (Belden Co., 32 AWG HVY Polythermalize, No. 8068) used were tightly wound in pairs to minimize magnetic flux linkage, and thus reduce the pickup noise during the SdH experiment.

The ampoules were broken inside the glove box and samples were secured in their positions on the boards, using a very small amount of vacuum grease. The leads were then brought in contact with the corners of the sample and conducting epoxy (Eccoband Solder 56C with Catalyst 9, purchased from Emerson and Cuming, Inc., Canton, MA) was used to attach the leads [Fig. 4.1(a)]. The contacts made by this epoxy proved to be ohmic and much stronger than those made at the earlier runs of these experiments, when silver paint (DuPont, composition No. 4929) was used. Leads attached by silver paint tended to fail and usually broke when the sample was cooled down to liquid Helium temperature, and subsequently brought back to room temperature. Recycling the temperature very rarely caused a problem when the above conducting epoxy was used.

The mounted sample was then inserted inside a rectangular (3 x 9mm ID; 1 mm wall thickness) rectangular ampoule, sealed at one end, very carefully; then the ampoule was sealed off, using epoxy (Stycast 2850F, with catalyst 9), while it was placed in a stream of He gas. This partial

filling of the ampoule with He gas was used as a means of heat exchange, since the ampoules were to be immersed in a liquid helium bath. Stycast, although a very good sealant for glass at room temperature, is not a perfect seal under temperature recycling. Cleaning the glass ampoule with trico and acetone before using Stycast proved helpful in retaining the seal.

The sealed ampoule was left inside the dry box for the conducting epoxy and sycast to cure (about 12-18 hours). A sketch of the encapsulated sample, with contacts attached and ready to be mounted on the sample holder, is shown in Fig. 4.2.

Although simple in principle, the above procedure proved to be the most crucial, as well as the most painstaking, step of the experiment. Working in the dry box for four or five hours can be very tedious and frustrating. Some brief hints which are results of the author's experience after repeating the above stps over 10 times follow:

a) Use flexible holding jigs (Edmund Scientific Co., Barrington, NJ) inside the dry box. As many as six hands are needed there -- and you have only two!

b) Plan to work inside the dry box as little as possible. Prepare the leads such that minimum changes in their position and length are needed inside the box.

c) Since the pot-life for stycast is about two-three hours, either prepare it in advance (mix it with catalyst) or use a hot-air blower to heat it for a few minutes. (After mixing with catalyst but prior to applying it to the ampoule.) Once heated, it will

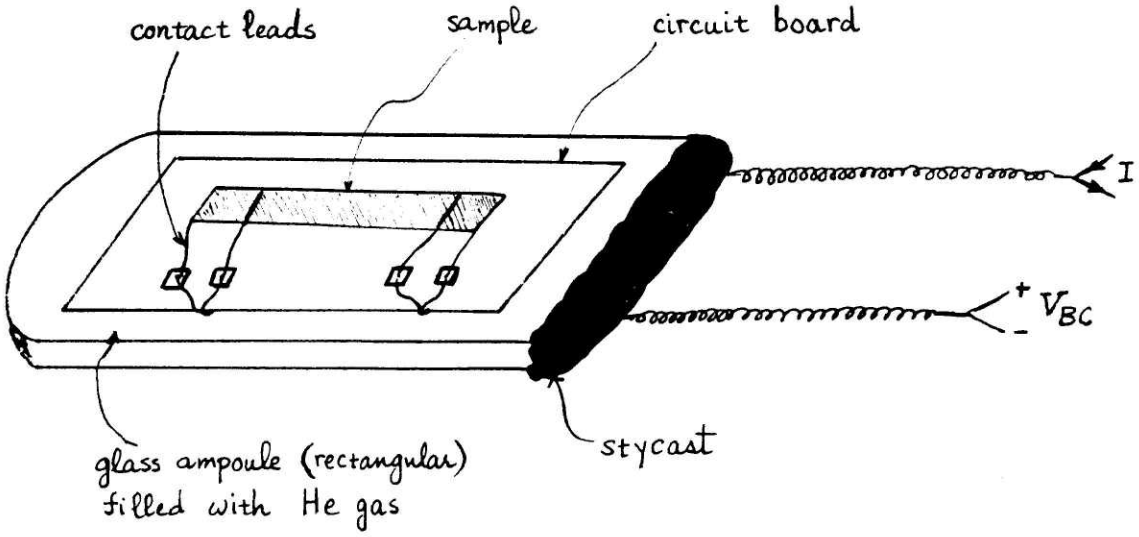


Figure 4.2

Sketch of the encapsulated sample with contact leads attached and ready to be mounted on the sample holder for the magnetoresistance measurements.

harden very fast ( $\sim$ 30 minutes), and it takes only a few hours to cure.

d) Leave the sealed ampoule in the He atmosphere overnight. Helium diffuses through glass easily. The antechamber of the dry box can be filled with He and used to store the ampoules while the Stycast is being cured. At other times, use a He-filled dessicator to store and transfer the samples.

In general, with good timing and calmness, the time spent working in the glove (dry) box can be cut down to one and one-half hours (for mounting two or three samples). This is important, because even though the dry box contains less than 1 ppm oxygen, the samples, especially low-stage compounds, are not stable in it for long periods of time such as 12 hours. As for the sealant, stycast was the best material available with the desired properties - i.e., endurance when recycling the temperature, and curing at room temperature (the alkali-metal graphite compounds cannot be heated to high temperatures). However, it was noted that Stycast reacts with the samples, especially when near them. This reaction was particularly notable for concentrated samples (stage $\leq 3$) and resulted in discoloration of the sample surface. However, the X-ray traces, even in the case of discolored samples, showed no change, in most cases. Hence, it may be concluded that Stycast has little effect on the bulk of the sample.

In order to ensure the stage fidelity of the samples (00$\ell$) X-ray diffractograms were taken at different steps of the experiment. Examples of such traces are shown in Fig. 4.3. This figure shows X-ray profiles for a K-stage-4 sample when it was still in its original reaction ampoule

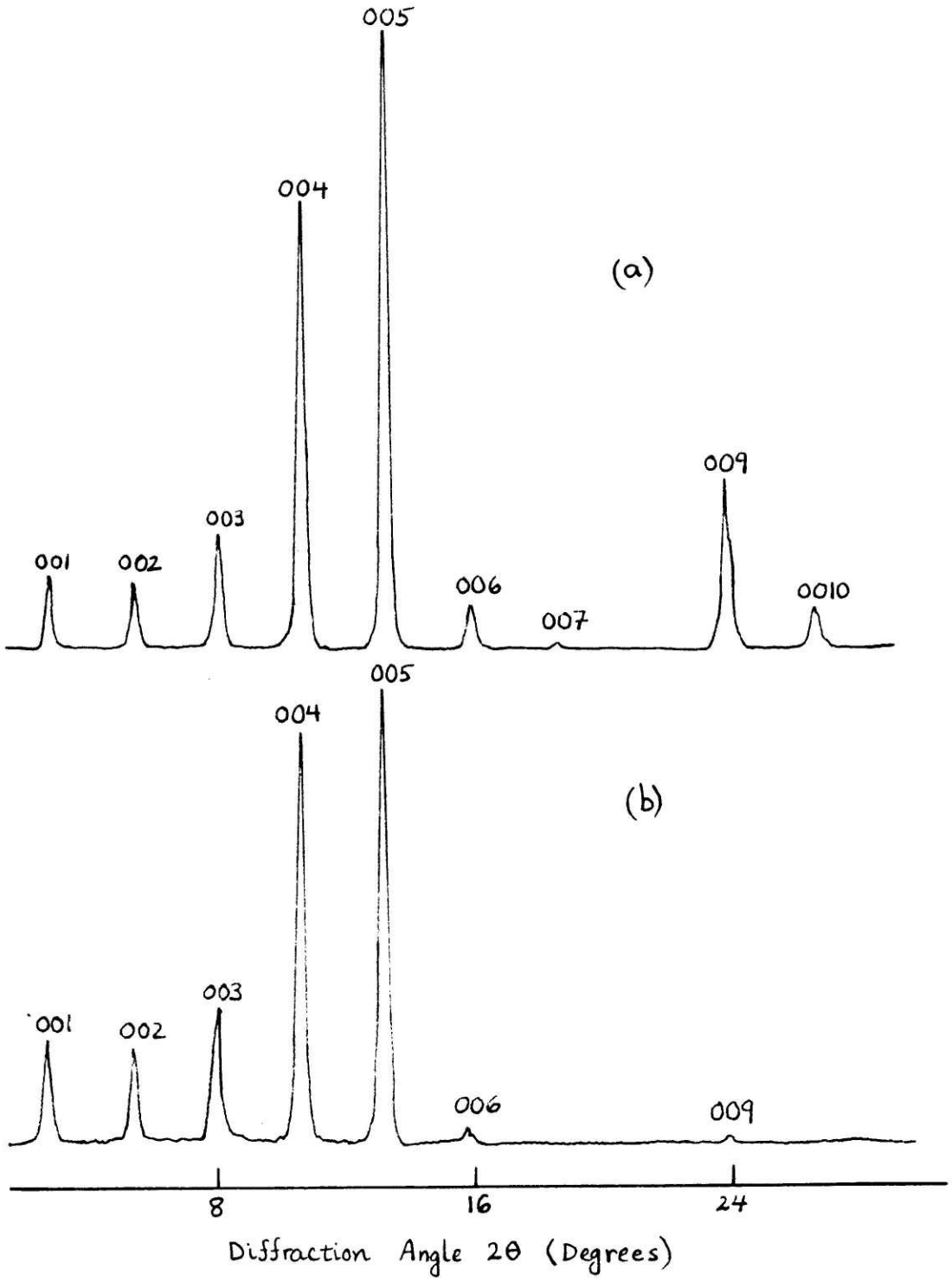


Figure 4.3

X-ray traces for a K-stage-4 sample before (a) and after (b) the SdH experiment. The position of the peaks and their linewidths are indicative of a K-stage-4 compound. The difference in relative intensities of peaks is related to the geometry of the glass ampoules encapsulating the sample.

(a), and after the SdH experiment (b). The position of the peaks and their linewidths are characteristic of (single-stage) potassium-stage-4 compound. The change in relative intensities of the peaks, especially the attenuation of the (009) peak, can be related to the geometry of the glass ampoules containing the sample: the ampoule used in trace (a) was made of a thin cylindrical tube, while in (b), rectangular tubing was used.

In numerous cases, when a sample of stage n, but containing a slight amount of stage n+1 was mounted, traces taken after the experiment showed that the sample had entirely changed to a pure stage n+1. In general, starting with a compound of single stage ($n > 1$), this encapsulation technique is capable of preserving the stage of the sample. If a compound of mixed stage is used, however, it is very likely that it will change toward the higher stage. In this thesis, unless explicitly stated otherwise, the reported results correspond to compounds whose stage identities were determined to be the same both before and after the SdH experiment.

## IV-2. The SdH Experiment

The resistivity measurements were made at the Francis Bitter National Magnet Laboratory for the field range $0 < H \lesssim 15$ Tesla and at liquid Helium temperature (4.2°K). In most cases, pumping on liquid He was used to get to lower temperatures(1.4 to 4.2°K).

The position of the sample in the magnetic field is shown in Fig. 4.4. Initially, with the c-axis of the sample parallel to the H-field constant-current I ($\sim$ 20 to 80 mA) flows through the current contacts A

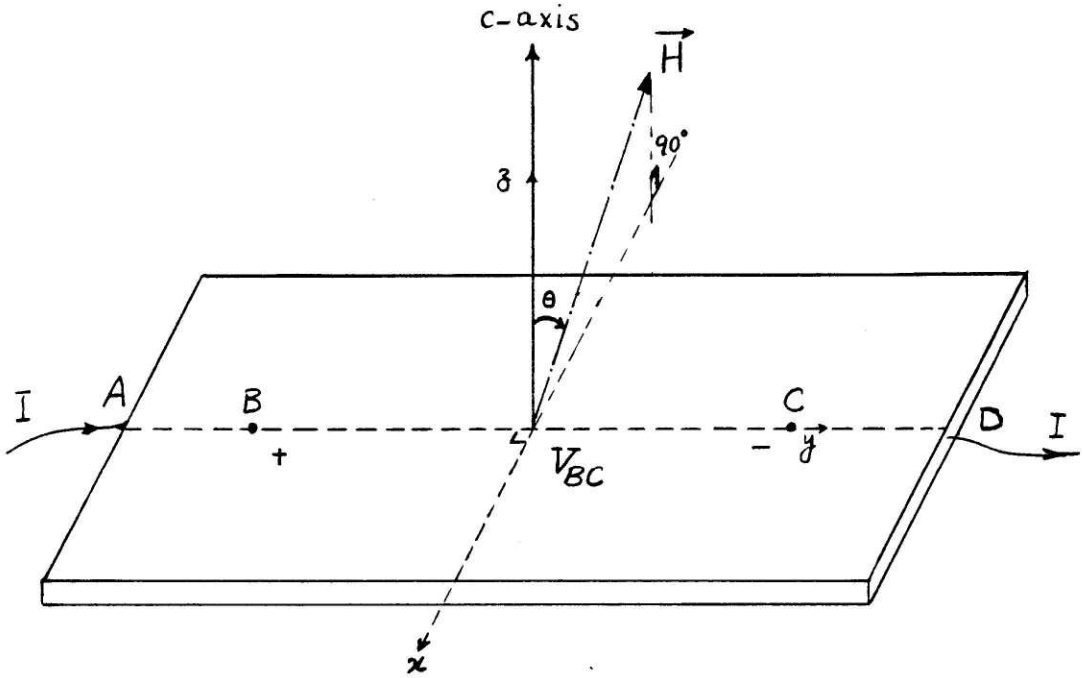


Figure 4.4

Sample geometry with respect to the magnetic field.
For angular dependence measurements, the sample is rotated around AD so that the c-axis of the sample makes an angle θ with $\vec{H}$. Since $\vec{H} \perp \vec{I}$, transverse magnetoresistance is measured.

and D while voltage $V_{BC}$, which is proportional to the electrical resistivity, is measured across the other two contacts. By rotating the sample around the AD axis, the angular dependence of the SdH oscillations is measured. $\theta$ is the angle between the c-axis and the H-field. Note that with this geometry, H is always perpendicular to AD, and hence transverse magnetoresistance is measured. The sample holder used in these studies was generously donated by Dr. L. Rubin of the Magnet Laboratory, and was rewired and slightly modified by the author. The modification made it possible to mount up to three samples at one time, and hence much time and expense was saved.

At the beginning of the experiment (with zero field), the contacts were checked to be ohmic. This check of contacts was done at both room temperature and at 4.2°K. The I-V relation was in most cases linear for currents of up to about 200 mA. The resistivities estimated from the slops of the I-V lines were, in general, in agreement with published values [ 1,2]. Resistivity dropped by a factor of 5 to 20 when the sample was cooled from room temperature to 4.2°K.

It must be emphasized that measuring the absolute resistivity of the material was not the aim of these experiments. As mentioned in section 4.1, the above method is not suitable for such measurement and the results should be considered only as an order-of-magnitude estimate of resistivity.

The magnetoresistance measurements were made using both DC and AC techniques. The emphasis was on the oscillatory part of the resistance, rather than the background magnetoresistance. In both dc and ac methods,

constant current I flows from A to D within the a-planes of the sample (Fig. 4.4). Figure 4.5 shows the dc setup. The voltage $V_{BC}$ is measured directly and recorded after amplification (Keithley precision nanovoltmeter No. 140) as the magnetic field is swept continuously from high to low field ($\sim$ 15 to 0 Tesla). A typical trace corresponding to a K-stage-5 compound is shown in Fig. 4.6. The magnitudes of the signal and oscillations are very typical (20-100 $\mu$V for a current of $\sim$ 40 mA) of the results that were obtained. The setup for the AC magnetoresistance technique is illustrated in Fig. 4.7.

The sample geometry and the constant current applied to the sample remain the same. Superimposed on the sweeping field, however, is a small sinusoidal magnetic field. The output signal $V_{BC}$, which is proportional to the derivative of the electrical resistivity with respect to magnetic field ($\partial\rho/\partial H$), is detected by a lock-in amplifier (Ithaco Dynatrac 391A). An oscillator (GenRad. 1310-B) and a frequency divider provide a stable 7.5Hz modulating signal to drive the oscillatory part of the sweeping field as well as the reference to the lock-in amplifier. The frequency divider, which divides the 60 Hz line frequency by 8, is essential in procuding stable modulation. In choosing the magnitude of the modulating signal, care should be taken: the magnitude must be large enough to produce a reasonable signal, yet it has to be sufficiently small not to lose the fine structure of $\partial\rho/\partial H$. A typical amplitude for the modulation field was $\sim$1000-2000 Gauss (0.1 - 0.2T). Figure 4.8 shows the signal obtained using the AC technique. Note the absence of the large magnetoresistance background present in Fig. 4.6. This is due to the fact that the AC signal is effectively the derivative of the DC signal. When

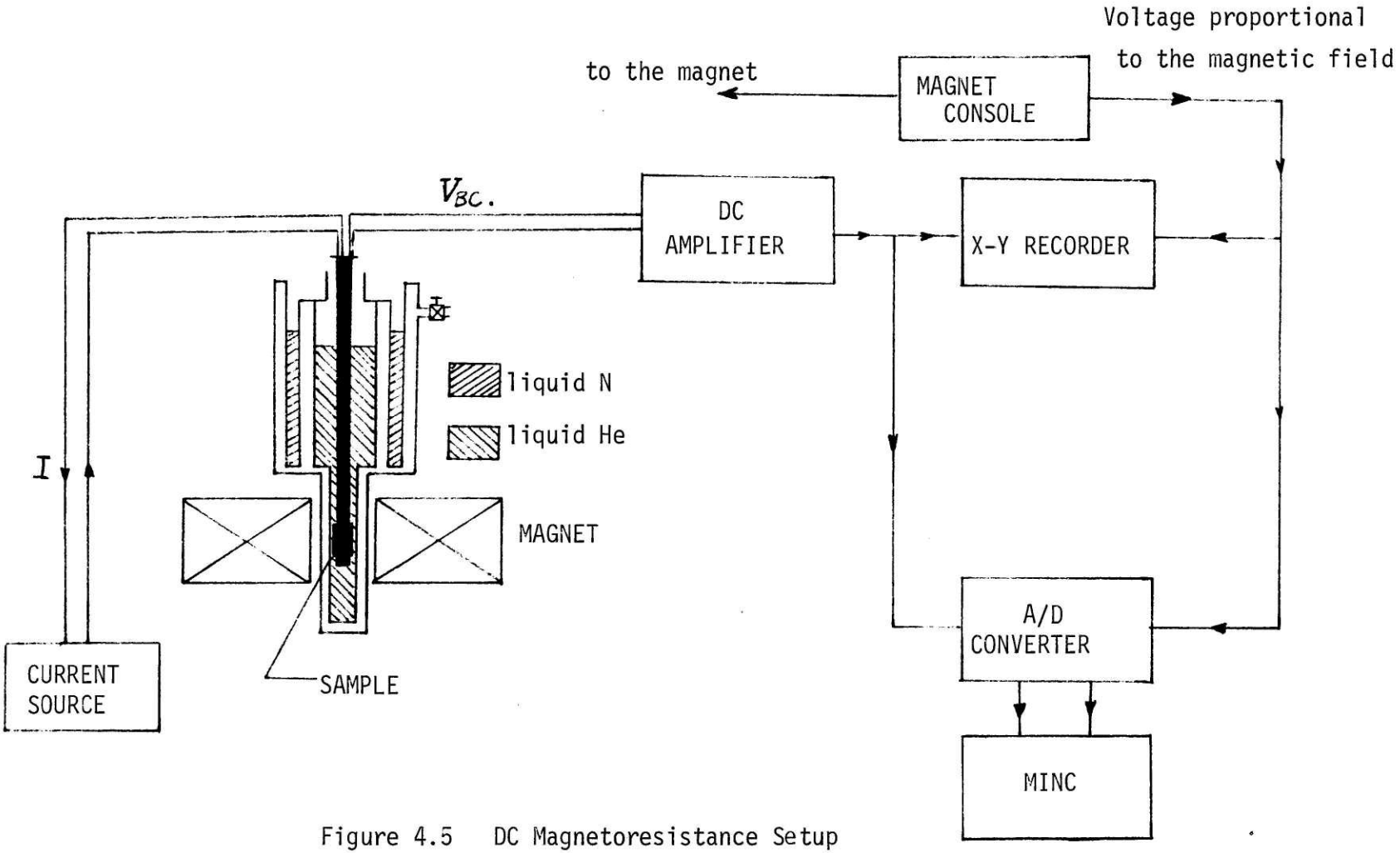


Figure 4.5 DC Magnetoresistance Setup

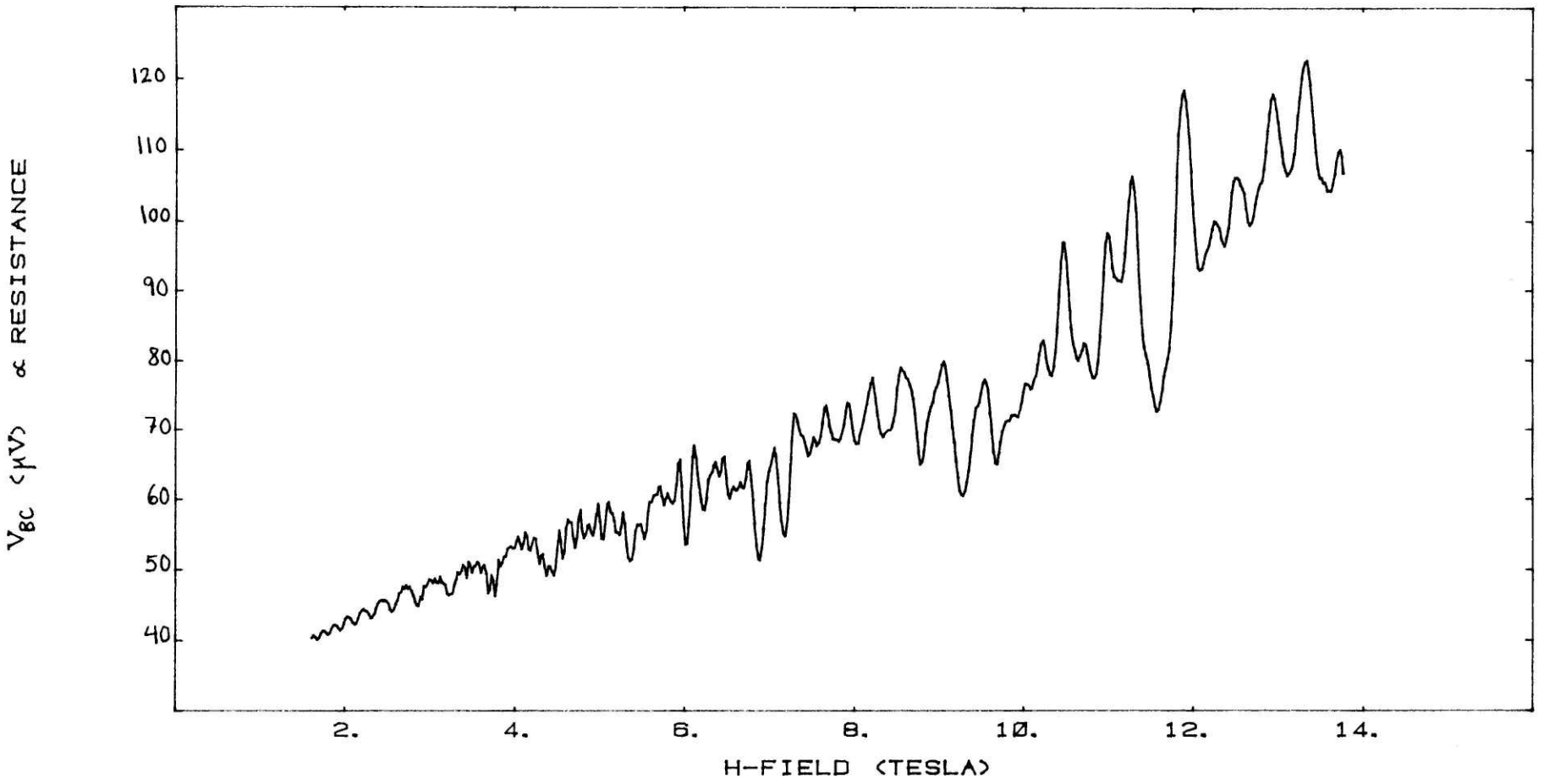


Figure 4.6
Voltage $V_{BC}$ (∝ resistivity) as a function of magnetic field for a potassium-stage-5 sample. Data were taken at 1.4°K with the c-axis of the sample parallel to the H-field.

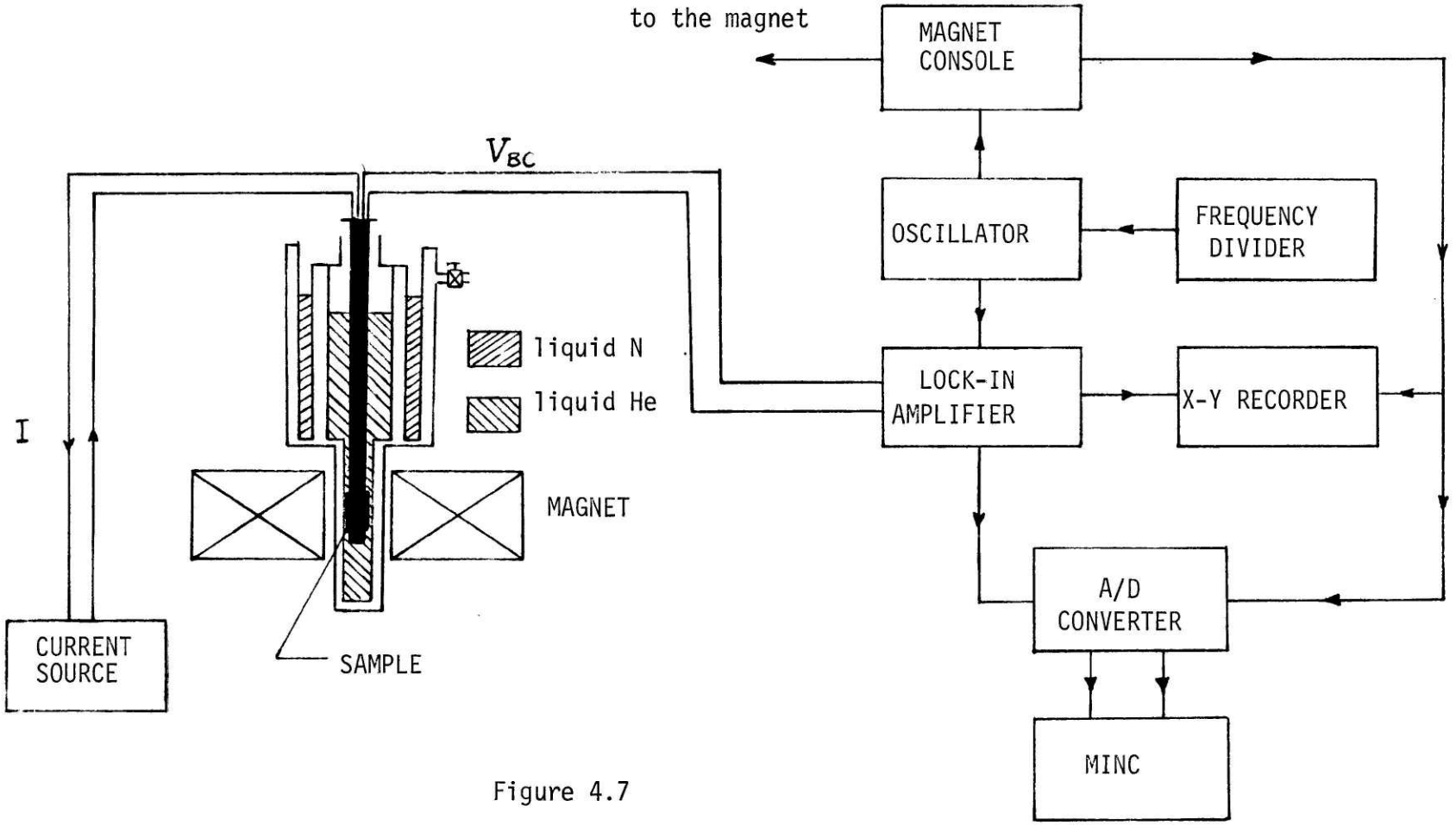


Figure 4.7

AC setup for measuring the derivative of resistivity with respect to field ($\partial\rho/\partial H$).

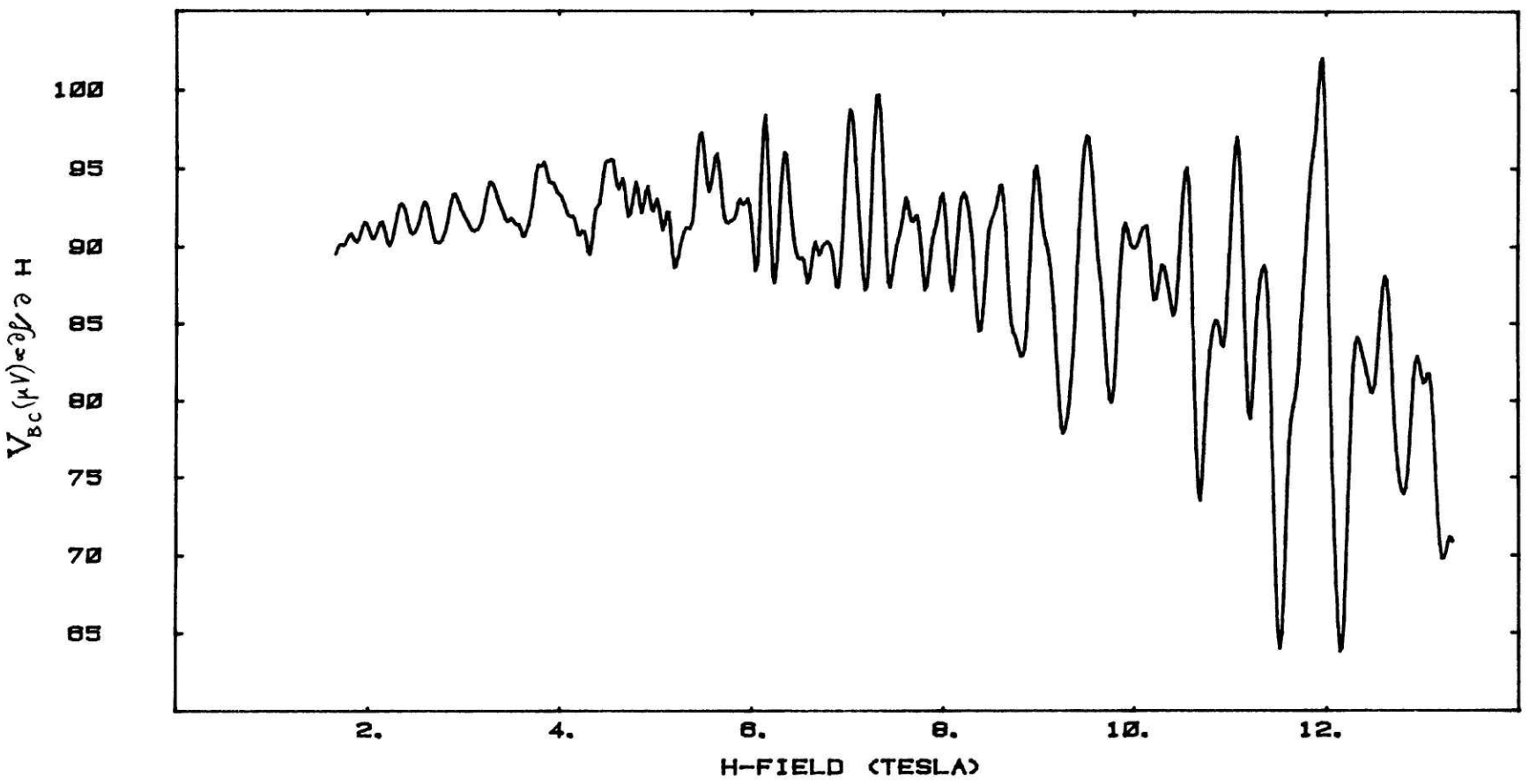


Figure 4.8

Derivative of the resistivity $\partial\rho/\partial H$ as a function of H for the potassium-stage-5 sample

Data were taken with T = 1.4°K and $\vec{C} \parallel \vec{H}$. Note the absence of a large background magnetoresistance. This is expected in view of the fact that in the AC technique, the derivative of the DC signal (Fig. 4.6) is effectively obtained.

the power spectra* for the DC and AC signals are compared (Figs. 4.9 and 4.10), we note that some of the fine structure of the DC spectrum is lost in the AC case, perhaps due to overmodulation (compare Figs. 4.9 and 4.10). In one case, modulation of the current I (Fig. 4.3) at a frequency of 500 Hz was used instead of field modulation. This technique did not improve the signal to any large extent.

The temperature-dependent measurements were made using another sample holder available at the Magnet Laboratory. Using this fairly sophisticated sample holder [57] one can attain any desired temperature (between 4.2 and $\sim 40°K$) with an accuracy of $\Delta T/T \cong 0.1\%$. The position and orientation of the sample cannot be changed, once it is mounted onto this sample holder; nor can the sample be encapsulated easily.

The presentation in the previous paragraphs about making the magnetoresistance measurements also applies when using this sample holder, with the additional constraint that, in order to avoid heating the sample, small current ( $\sim$ few mA) should be used.

In general, one of the major sources of noise in these measurements is the current induced in the four contact wires attached to the sample. In the DC case, the large magnetic field varies only slowly, however, the sample and the leads vibrate a great deal because of the vibrations of the magnet due to the water-cooling hoses. In the AC case, some of the noise due to vibrations is reduced; however, the modulating magnetic field passing through the wire loops varies much faster. To deal partially with this source of noise, which is common to both methods, the lead wires were tightly twisted in pairs to minimize the loop area, and hence the

* Details concerning data processing and the taking of the Fourier transforms will be discussed shortly, in the next section.

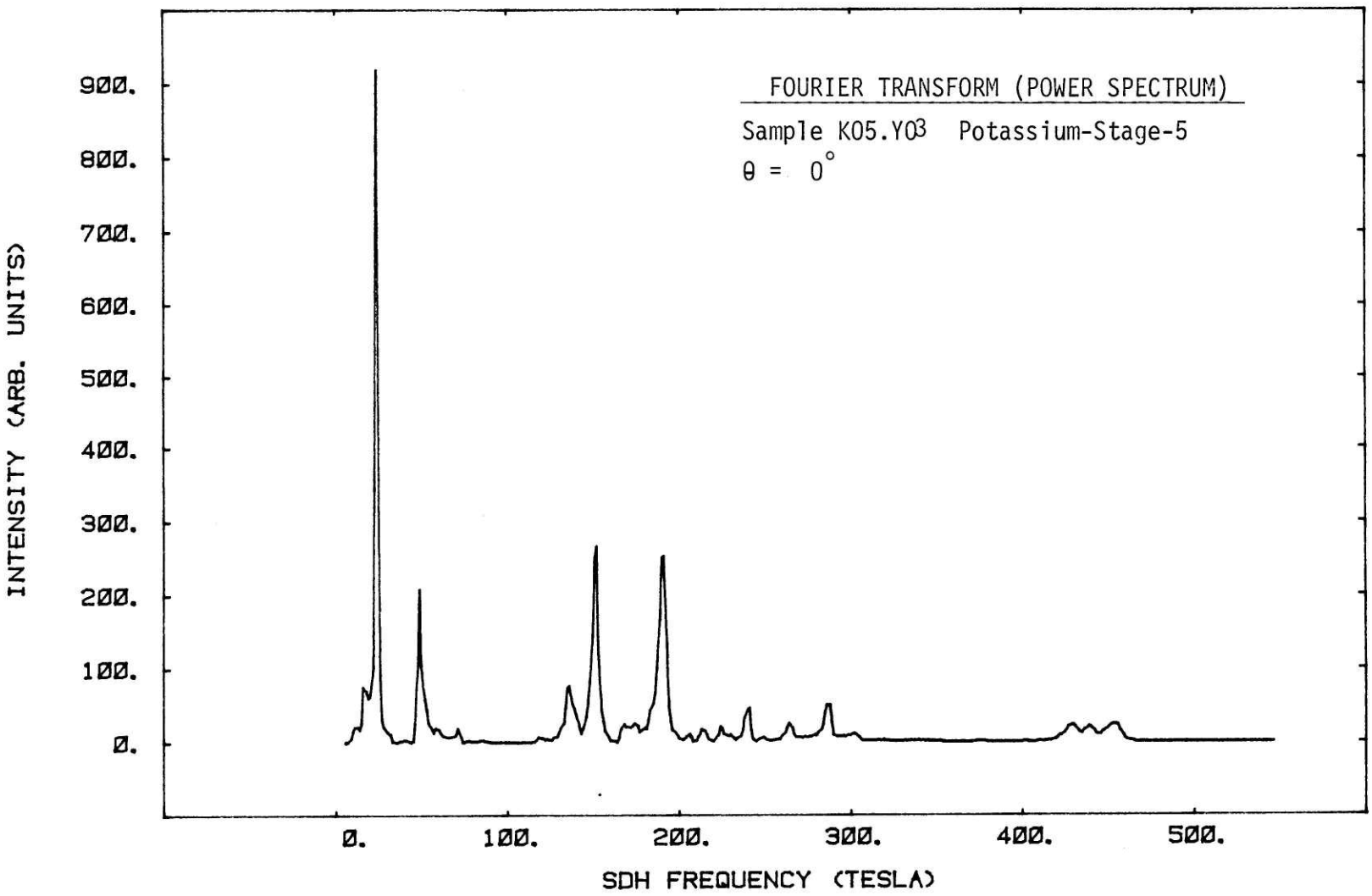


Figure 4.9

Power spectrum of the resistivity $\rho_{oscil.}$ versus $H^{-1}$ corresponding to Fig. 4.6. The fine structure (multitude of frequencies) present in Fig. 4.6 is made evident in this spectrum.

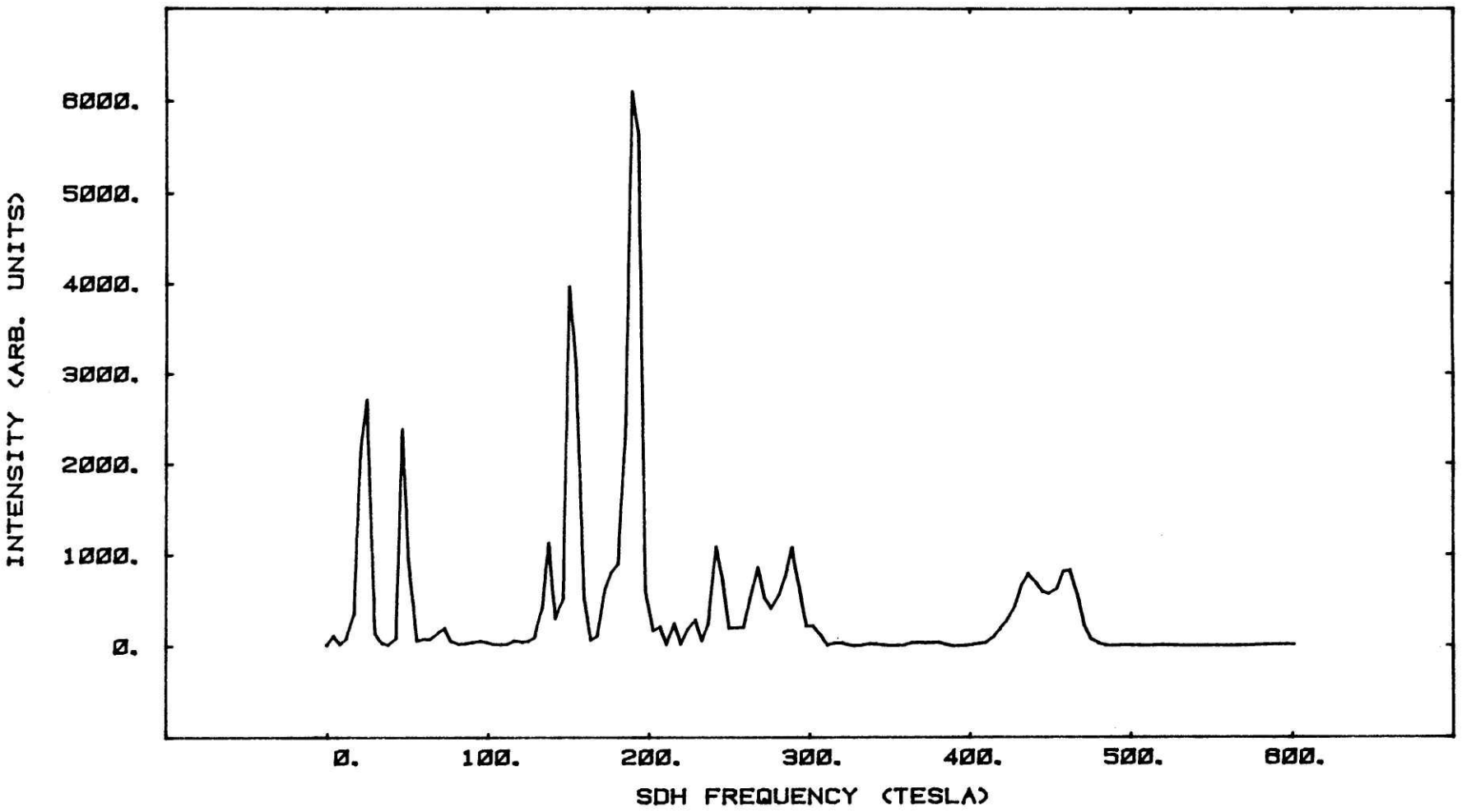


Fig. 4.10

Power spectrum of $\partial\rho/\partial H$ vs $H^{-1}$ (see next section) corresponding to AC signal of Fig. 4.8. This should be compared to Fig. 4.10 which is the power spectrum of the DC signal (Fig. 4.6). Some fine structure has been lost, especially at the higher frequencies ( $\sim$ 450 T).

induced currents.

The output signal $V_{BC}$, as mentioned before, was usually in the range 20-100 μV. For a water-cooled magnet, and with the geometry of the experiment, signals less than a few μV are comparable to the noise level. It is thus desirable to have large signals. One way to do this is to increase the resistance of the samples.

The recently grown samples which had dimensions $\sim$3 x 15 x .05 mm proved to be very suitable for this experiment: at zero field and 4.2°K, with a current of $\sim$40 mA, they produced signals as large as $\sim$ 50 μV. Hence, this sample shape is recommended for this experiment.

IV-3. Acquisition and Reduction of Data

It was stated in section 2.5 that the oscillatory behavior of the magnetoresistance is periodic in 1/H. It is evident from Figs. 4.6 and 4.9 that these oscillations occur at many frequencies and that there is also fine structure. Thus, in order to extract the details of these profiles, it was necessary to use a computer for the acquisition and processing of the data. Data processing, in brief, consisted of inverting the H-field and taking a Fourier transform (power spectrum) of $\rho_{oscil.}$ or $\partial\rho/\partial H$) vs 1/H. Details of data acquisition and processing will now be presented.

To take the data, the signal $V_{BC}$ and the voltage proportional to the magnetic field were digitized and recorded in pairs on floppy disks using a MINC 11/3 (Digital Equipment Corporation) computer. When equipment was available, the experiment was performed on two samples simultaneously; in this case, triplets of numbers (Field, $V_{BC}^{(1)}$, $V_{BC}^{(2)}$) were recorded. The programs used for recording data DVM1 and DVM2 are

modified versions of the program RMDVM written by D. Nelson of the Magnet Laboratory. In most cases, 3000 pairs (or triplets) of data were taken at the rate of 10 pairs per second (magnetic field was usually swept in five minutes). If needed, the magnetic field could have been swept more slowly, and also more data points could have been recorded, but this was rarely necessary.

Once the data acquisition was complete, a FORTRAN program, SDH, was used to analyze the data. SDH does the following:

a) Reads data pairs [Fig. 4.11(a)]

b) Subtracts the background magnetoresistance to find the oscillatory part of the data, $\rho_{oscil.}$. This is done by least-square fitting of a first-or second-degree polynomial $(a_o + a_1 H + a_2 H^2)$ through all data points, and subtracting this polynomial (point by point) from the data.

c) Samples the resistivity values as a function of uniform inverse magnetic field. The data thus obtained are (proportional to oscillatory) resistivity vs (uniform) 1/H. A plot of data ($\rho_{oscil.}$ vs 1/H) at this stage of the analysis is shown in Fig. 4.11(b); here the sinusoidal oscillations, as well as the beat frequencies, can be clearly seen.

d) Pads the data obtained in part (c) with zeroes to make the number of points equal to a power of two (usually $2^{11}$ = 2048 points). This is required by the Fast Four Transform (FFT) algorithm. The FFT subroutine used is DEC's FFTM.MAC. Zero padding also allows one to obtain a better resolution in the power spectrum. More about zero-padding and the Discrete Fourier Transform (DFT)

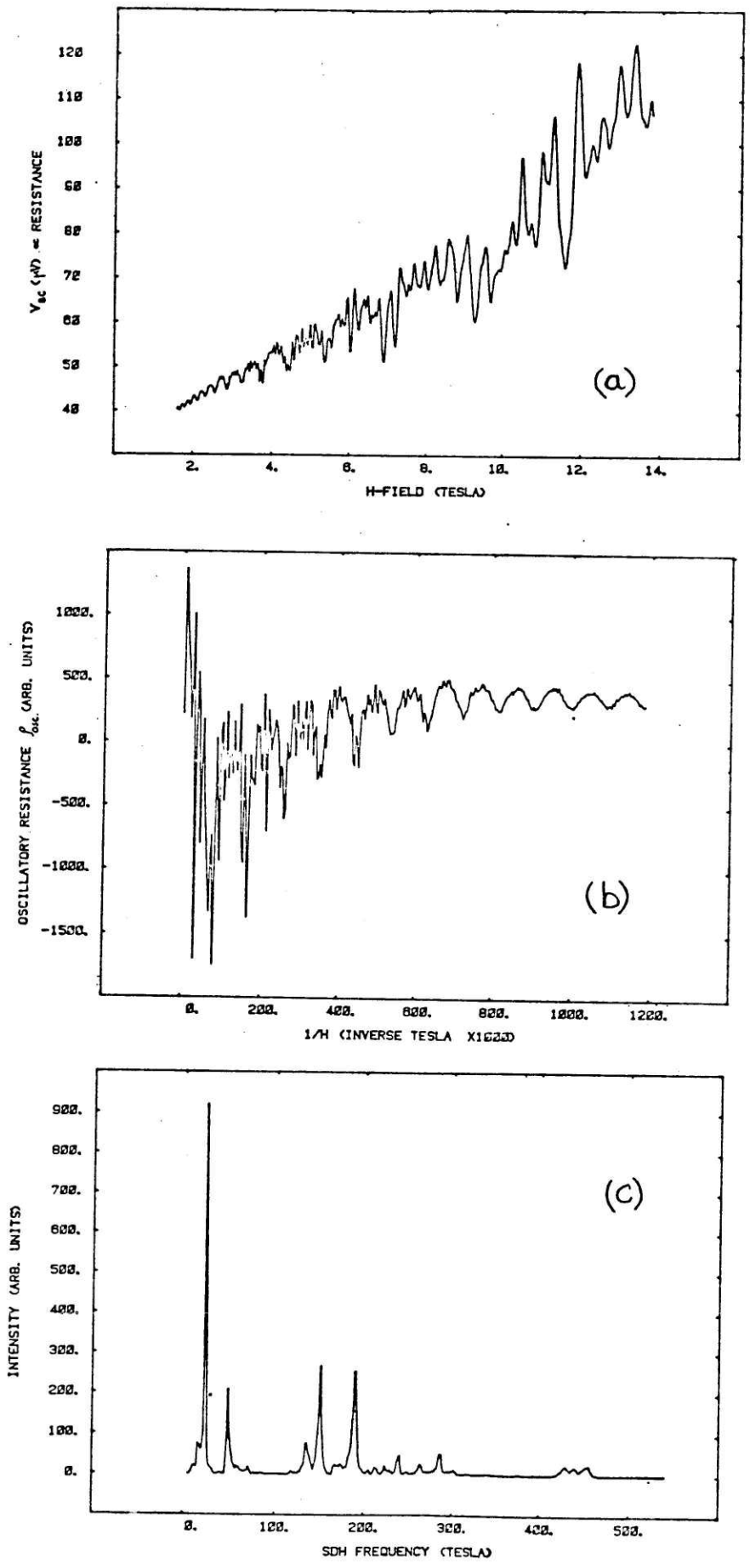


Figure 4.11

Digital processing of the SdH data:

a) Raw data ρ vs H.

b) $\rho_{oscil.}$ vs 1/H data(after subtraction of the magnetoresistance background.

c) The power spectrum of $\rho_{oscil.}$ vs 1/H.

will be presented in Appendix A.

e) Fourier transforms the data in (d), squares the real and the imaginary parts of the DFT, adds the squares and records the sums as the power spectrum points. A plot of such a power spectrum is shown in Fig. 4.11(c).

The basic structure of the program SDH should be clear from the above description. Most of its parts are straightforward. When inverting H and obtaining $\rho$ vs uniform 1/H, one should be careful, since writing an efficient program that does this is somewhat tricky! To obtain spectra with good resolution (1-2 Tesla), zero-padding (see Appendix A) is usually necessary.

Note in the spectrum of Fig. 4.11(c) that, since the data in Fig. 4.11(b) are periodic as a function of 1/H, then the frequencies of oscillations have units of H; i.e., Tesla. Also note the structure of this spectrum, and also that the low- and high-frequency oscillations differ in several respects. The high-frequency oscillations, which correspond to large cross sections of the Fermi surface, have larger (cyclotron) effective mass associated with them. They are smaller in amplitude, and they are also attenuated more rapidly at lower fields. This is an expected feature of SdH experiments (section 2.5). The next chapter deals with the general and specific features of these spectra.

# V. EXPERIMENTAL RESULTS

Chapters V and VI deal with the presentation and analysis of the experimental data. In both of these chapters we first focus on a specific sample (potassium-stage-5) and treat it in much detail. A summary of the results for the other compounds then follows. In section 5.1 of this chapter, the Shubnikov-de Haas (SdH) results and their angular and temperature dependence will be presented for a K-stage-5 sample. Section 5.2 gives a summary of the SdH results for potassium and rubidium compounds. In the last section, 5.3, some brief comments are made about the general features of the results for the different compounds.

## V-1. Results for a Potassium-Stage-5 Compound

In this section, the SdH results for a K-stage-5 sample (namely, sample KO5.YO3 in Table 3.1) are presented. This sample is chosen for a detailed presentation because the SdH experiment was performed on it twice (with new sets of leads and encapsulation for each run) and both the $\rho$ vs H data and the power spectra for the two runs were practically identical. Also, when the SdH experiment was done on another K-stage-5 sample, there was again no notable difference between the results for the two stage-5 samples. Moreover, because of the higher stability of the K-stage-5 compound, compared to the compounds of lower stage, the SdH oscillations for this compound were observed more reproducibly. Finally, this is the compound for which the angular dependence data are most complete and accurate.

Figure 5.1 shows the transverse magnetoresistance results for this K-stage-5 sample at 1.42°K and $0 \leq H \leq 14$ Tesla for $\theta$ = 0°,10°,20°,30°, 40°, 45°, 55° and 65°. Recall from Chapter IV that $\theta$ is the angle between

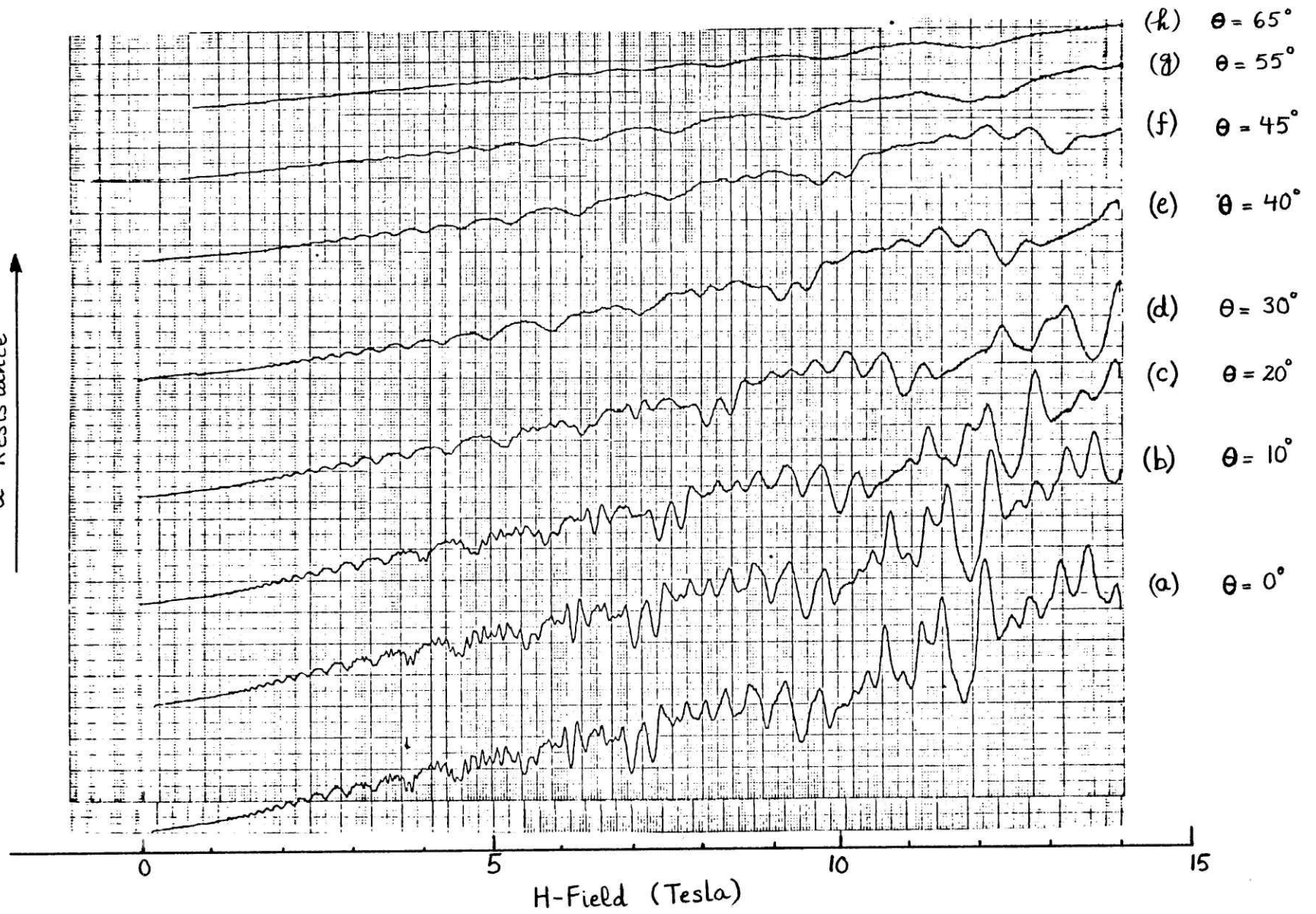


Figure 5.1

The transverse magnetoresistance results at T = 1.42°K for a potassium-stage-5 sample. (a) through (h) show the magnetoresistance data as a function of angle θ, where θ is the angle between the c-axis of the sample and the direction of the magnetic field. Note that as θ is increased, the amplitudes of the oscillations (especially those with high frequencies) are attenuated.

the magnetic field tand the c-axis of the sample (Fig. 4.4). The power spectea of the $\rho$ vs 1/H data corresponding to some of the traces in Fig. 5.1 are shown in Fig. 5.2. Some features of these oscillatory magnetoresistance data, which are also common to other compounds studied in this thesis, can be easily seen from Figs. 5.1 and 5.2. In general, in the SdH experiment, the high-frequency oscillations are weaker in amplitude than the ones with smaller frequencies. This is because the larger frequencies correspond to larger cross-sectional areas of the Fermi surface (section 2.5) and the (cyclotron) effective mass m* (in an orbit containing the cross-sectional area A) defined by:

$$m^* = \frac{\hbar^2}{2\pi} \frac{\partial A}{\partial E} \tag{5.1}$$

is heavier for the larger areas. Note from Eqs. 2.28 and 2.29 that the oscillations in resistivity are more heavily damped with increasing m*. This effect can be seen in Figs. 5.1(a) and 5.2(a), which show, for example, that the $\sim$450 Tesla frequency is small in amplitude and also dies out at the lower field values much faster than the small-frequency oscillations, such as the 24-Tesla frequency oscillation.

Another important feature is that as the angle $\theta$ is increased, the frequencies of the oscillations shift toward higher values, while their amplitudes are decreased. One can see in these two figures that at $\theta = 35°$, for instance, the $\sim$150 Tesla frequency has shifted to $\sim$180 Tesla with decreased amplitude, while the 450 Tesla frequency can no longer be seen because of its very small amplitude. In Table 5.1 the frequencies observed for the K-stage-5 sample at different $\theta$ values are tabulated. Note that the higher the frequency, the smaller the extent of $\theta$ over

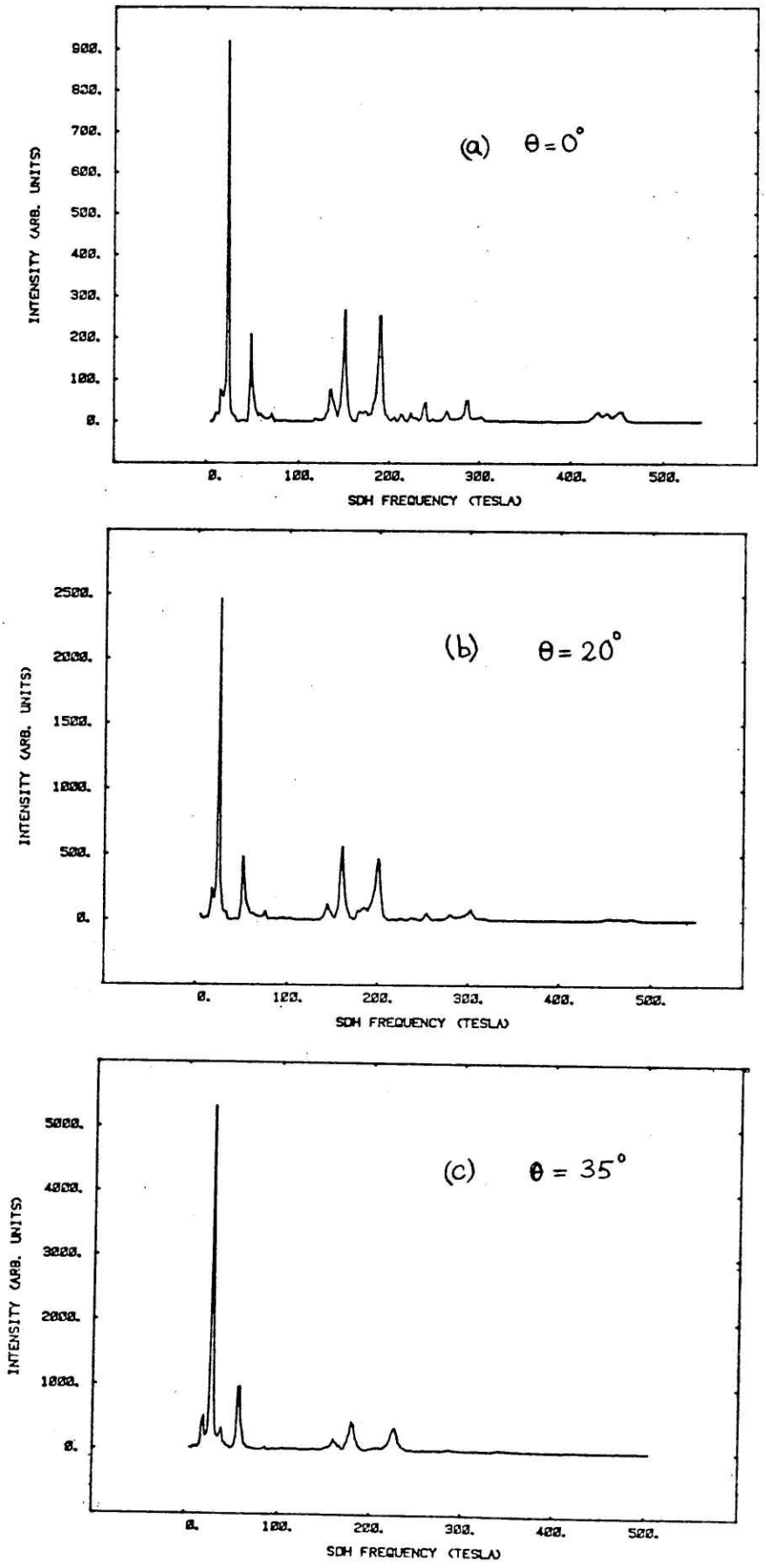


Figure 5.2

The Fourier transforms (power spectra) of the ρvs 1/H data corresponding to the traces shown in Fig. 5.1.

Note the shift of the frequencies (peaks) towards higher values as θ increases. (See discussion in the text.)

| θ(degrees) | Shubnikov-de Haas Frequency (Tesla) | | | | | | | | | | | | | | | | |
|---|---|---|---|---|---|---|---|---|---|---|---|---|---|---|---|---|---|
| 0 | 18 | 24 | 48 | 71 | 135 | 152 | 172 | 191 | 213 | 224 | 243 | 267 | 290 | 302 | 430 | 439 | 453 |
| 5 | 18 | 24 | 48 | 71 | 137 | 153 | 175 | 192 | 215 | 225 | 243 | 267 | 290 | 304 | 431 | 441 | 455 |
| 10 | 18 | 24 | 50 | 72 | 138 | 153 | 175 | 192 | 216 | 226 | 243 | 268 | 292 | 304 | 432 | 442 | 457 |
| 15 | 18 | 25 | 50 | 73 | 139 | 155 | 176 | 195 | 219 | 230 | 246 | 270 | 296 | 305 | 439 | 449 | 463 |
| 20 | 18 | 26 | 52 | 76 | 144 | 161 | - | 201 | 226 | 237 | 254 | 280 | 303 | - | 454 | 463 | 479 |
| 25 | 18 | 26 | 53 | 77 | 147 | 163 | - | 206 | 230 | 242 | 260 | 287 | 315 | - | - | - | - |
| 30 | 19 | 28 | 56 | 84 | 157 | 177 | - | 220 | - | - | 276 | 307 | 329 | - | - | - | - |
| 35 | 20 | 29 | 59 | 86 | 160 | 180 | - | 227 | - | - | - | - | - | - | - | - | - |
| 40 | 22 | 31 | 63 | 96 | 175 | 197 | - | 247 | - | - | - | - | - | - | - | - | - |
| 45 | 24 | 33 | 67 | - | 188 | 212 | - | 263 | - | - | - | - | - | - | - | - | - |
| 50 | - | 37 | 72 | - | - | - | - | - | - | - | - | - | - | - | - | - | - |
| 55 | - | 40 | 80 | - | 200 | 248 | - | 321 | - | - | - | - | - | - | - | - | - |
| 60 | - | 48 | - | - | - | - | - | - | - | - | - | - | - | - | - | - | - |
| 65 | - | 53 | 107 | - | - | - | - | - | - | - | - | - | - | - | - | - | - |
| 70 | - | 62 | - | - | - | - | - | - | - | - | - | - | - | - | - | - | - |
| 75 | - | 74 | - | - | - | - | - | - | - | - | - | - | - | - | - | - | - |
| b/a | - | 5.0 | 4.6 | 4.9 | 2.8 | 4.9 | - | 5.3 | 2.5 | 1.3 | 3.0 | 7.3 | 2.9 | - | 2.6 | 2.3 | 2.5 |

Table 5.1

The SdH frequencies for a K-stage-5 sample at different θ (angle between the c-axis of the sample and the direction of the magnetic field). The anisotropy ratios (b/a) of least-squares fitted ellipsoids are listed in the last row.

which the frequency can be followed. The reason for the upshift of the frequencies to larger values can be understood by considering an anisotropic Fermi surface (FS) of general shape, such as is shown in Fig. 5.3, such that the cross-sectional area perpendicular to the direction of the field increases with θ. In fact, one can plot the ratio $\nu_o/\nu_\theta = A_o/A_\theta$ for the experimental SdH frequencies as a function of θ. Here, ν and A stand for the SdH frequency and the extremal cross section of the FS, respectively, and the subscript gives the value (in degrees) of θ at which the frequency is measured. Such a plot is shown in Fig. 5.4, and gives information about the topology of the FS.

In Fig. 5.4, the solid line is the plot of $\nu_o/\nu_\theta = \cos\theta$, which corresponds to a cylindrical FS [Fig. 5.3(a)]. The dashed line is related to $\nu_o/\nu_\theta$ for an ellipsoidal FS with an anisotropy ratio of b/a = 5.0 (see Fig. 5.3(b)]. Indeed, one can find the b/a ratio of ellipsoids that best (least-squares) fit the experimental points (Appendix B). This was actually done for the data of Table 5.1 and the resulting b/a are given in the last row of this table. The accuracy of these b/a values is very poor (± 0.5 to ±3, depending on the extent of θ to which the frequency could be followed). This is evident from Table 5.1 and Fig. 5.4 , and is due to the fact that b/a is most sensitive to $\nu_o/\nu_\theta$ at large values of θ ( > 50°) and most of the frequencies cannot be followed to such high θ. The general comment about these angular dependent results is that they are compatible with a highly anisotropic FS, a result which is itself compatible with the interpretation of results given in the next chapter, using the theoretical models.

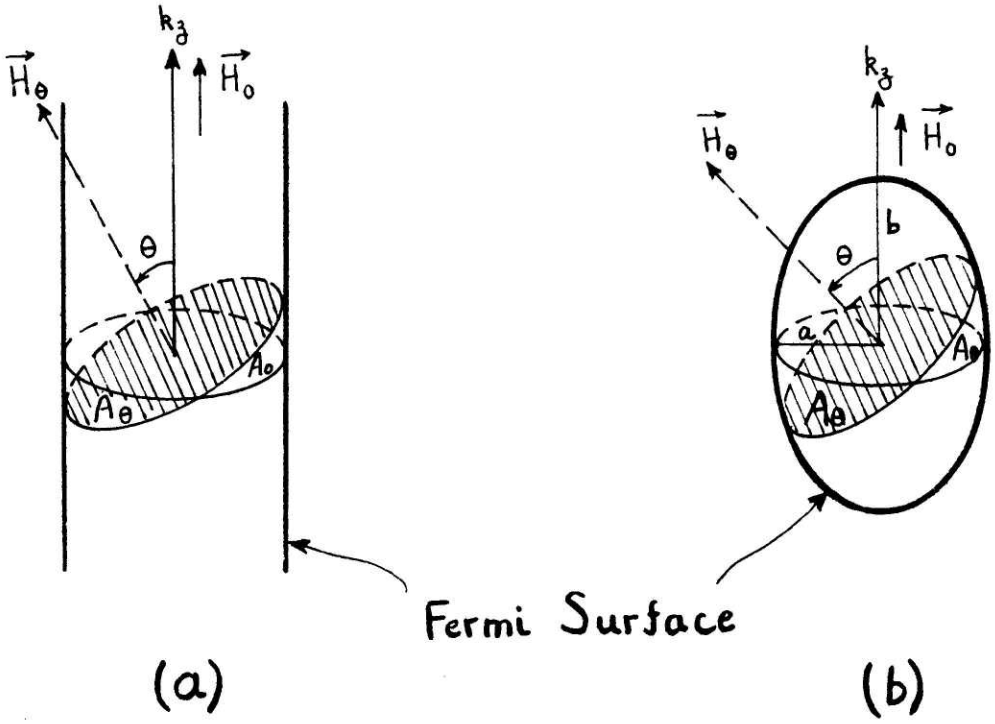


Figure 5.3

Cylindrical (a) and ellipsoidal (b) Fermi surfaces. Note the increase in the cross-sectional area perpendicular to the H-field direction as the angle θ between $\vec{H}$ and $\vec{k}_z$ of the sample is increased.

For case (a), $A_o/A_\theta = \cos\theta$, while for

(b), $A_o/A_\theta = [\cos^2\theta + \frac{a^2}{b^2}\sin^2\theta]^{1/2}$ (Appendix B).

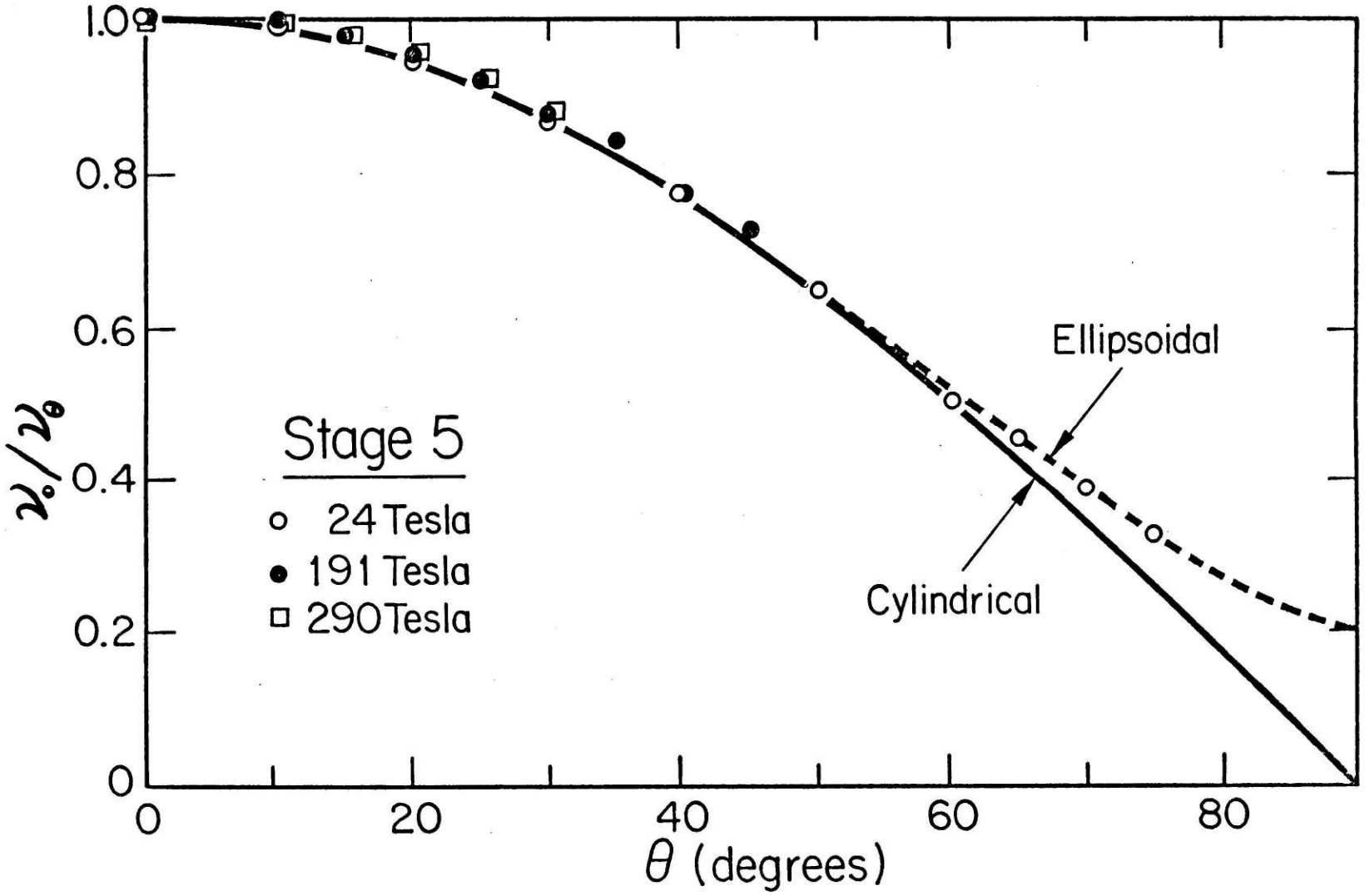


Figure 5.4

The angular dependence of some of the SdH frequencies observed for a K-stage-5 sample. The normalized frequencies $\nu_0/\nu_\theta$ are plotted as a function of θ (angle between c-axis of the sample and the H-field). The solid line is a cosine curve (cos θ) and corresponds to a cylindrical Fermi surface, while the dashed line is for an ellipsoidal Fermi surface with a b/a ratio of 5.0.

As mentioned at the beginning of this section, the SdH experiment was repeated on this K-stage-5 sample after putting on a new set of leads and again encapsulating the sample. The Fourier transform for the repeat experiment is shown in Fig. 5.5 (for $\theta = 0^{\circ}$). Also, the experiment was performed on another K-stage-5 sample and the resulting Fourier transform is given in Fig. 5.6. Note that these transforms are virtually the same*, and that the frequencies contained in them are consistent with those present in Fig. 5.2(a) within about 5%. (A discussion of the accuracy of the reported frequencies will be given in section 5.3.)

The temperature-dependent SdH measurements were performed on two other K-stage-5 samples (K05.W17). These two were grown in the same ampoule under identical conditions. Unfortunately, since encapsulation was not feasible with the temperature-controlled sample holder, these samples were exposed to air for $\sim$ 30 minutes while being mounted onto the sample holder. The X-rays taken the day after the SdH experiment showed that the (00$\ell$) peaks of one of the samples, here referred to as KTEMP.A, were broadened relative to the other stage-5 samples to some extent, while the other sample, KTEMP.B, exhibited an X-ray trace characteristic of a single-stage-5 compound. Surprisingly, sample KTEMP.A was the one which gave the more stable SdH signal. The broadening of the X-ray peaks could be related to the fact that this sample was slightly damaged, physically, after the experiment when the contact leads were removed. The damage resulted because this sample was extremely thin and fragile. The Fourier transforms of $\rho$ vs 1/H (at T = 4.4°K) for these samples are shown in Figs. 5.7(a) and 5.7(b). These should be compared

* Except for the relative intensities of some of the peaks; see section 5.2 for an explanation.

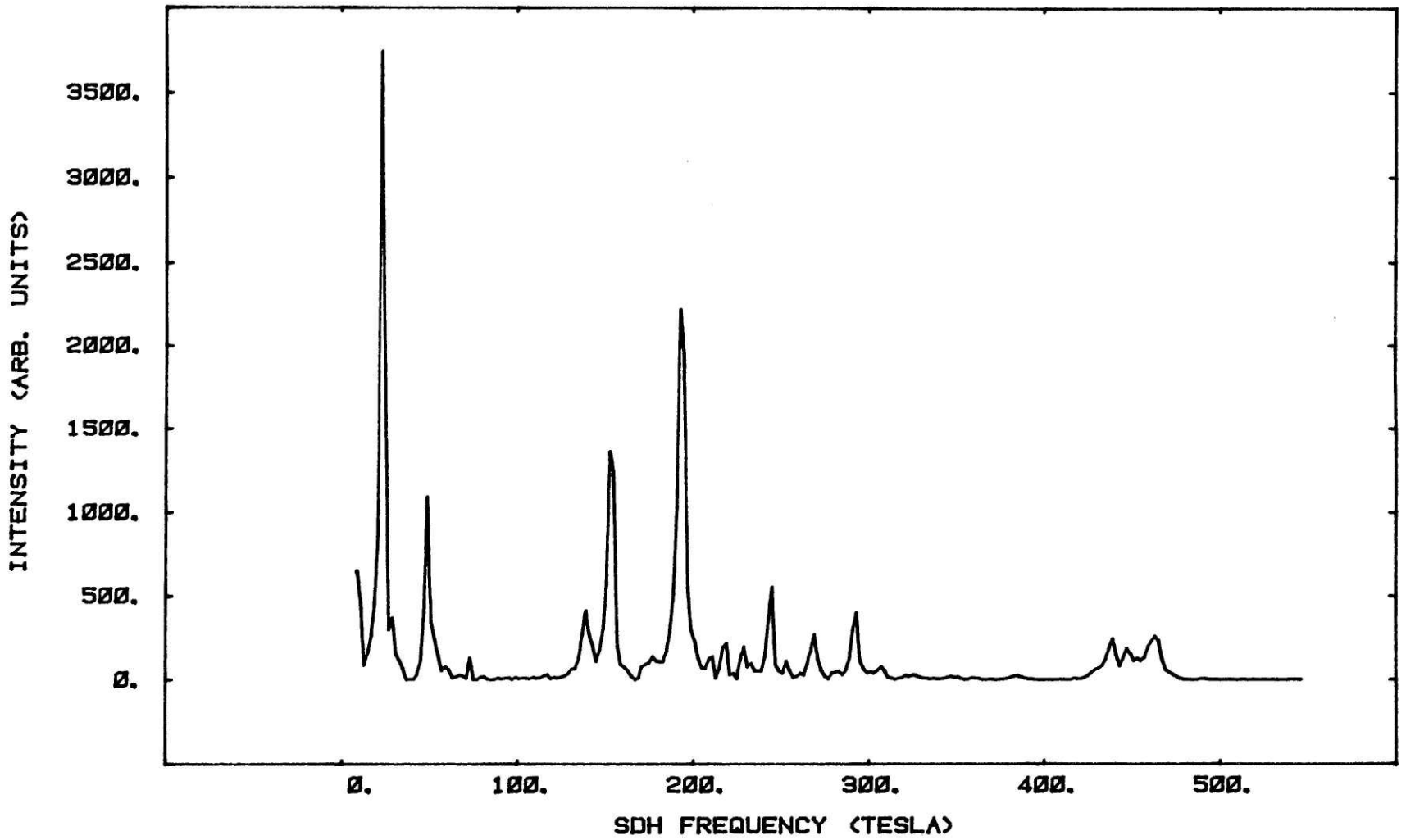


Figure 5.5

The power spectrum of $\rho$ vs 1/H for sample K05.Y03 (K-stage-5) when a new set of leads was used ($\theta = 0°$). This spectrum should be compared to the spectrum shown in Fig. 5.2(a), which corresponds to the same sample. An explanation for the change in relative intensities of the $\sim$190 Tesla peak is given in section 5.2.

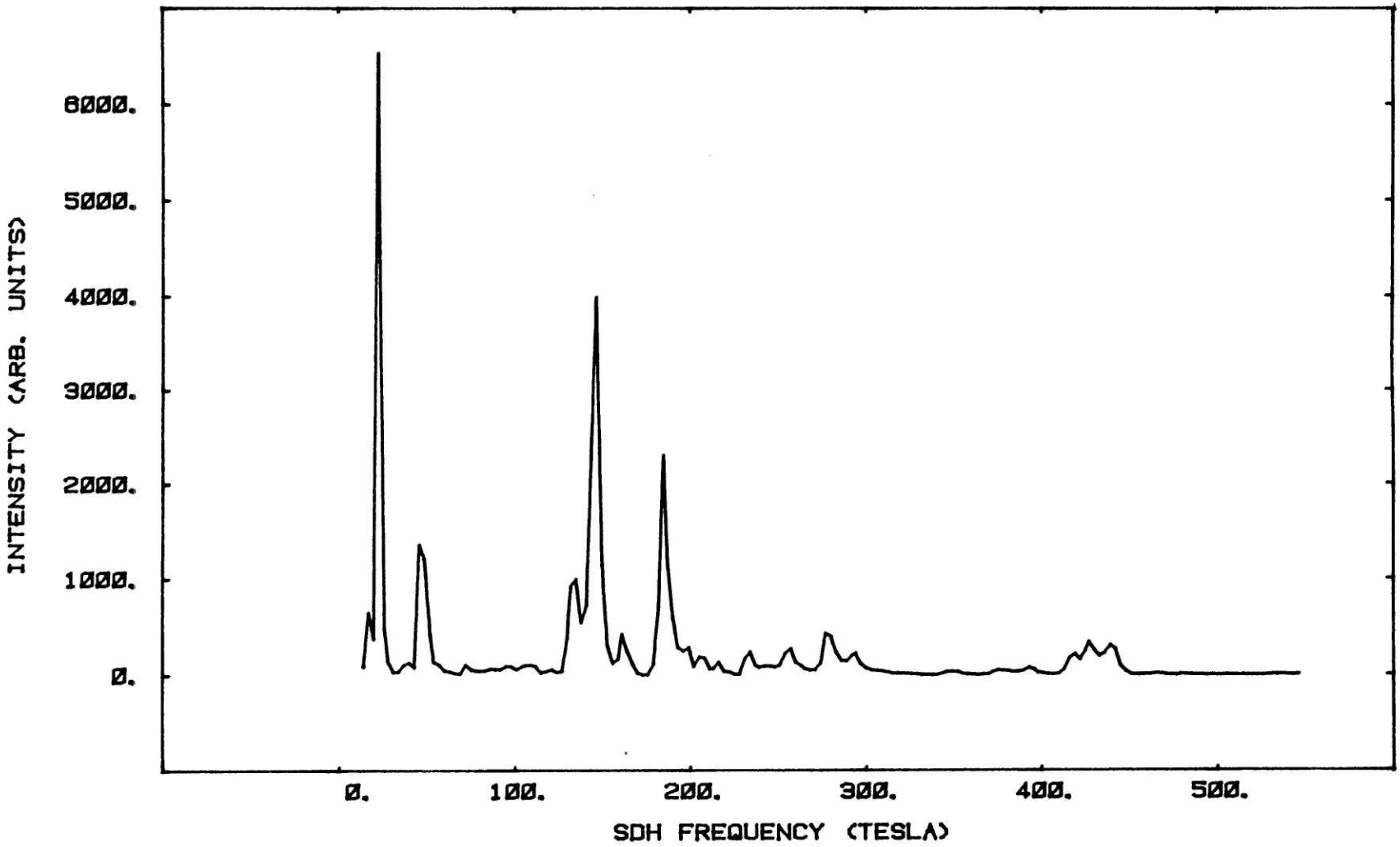


Figure 5.6

The power spectrum of $\rho$ vs 1/H for another K-stage-5 sample ($\theta = 0°$). Again, except for the relative intensities of the peaks (see section 5.2), this spectrum is the same as that of sample K05.Y03. [Figs. 5.2(a) and 5.4].

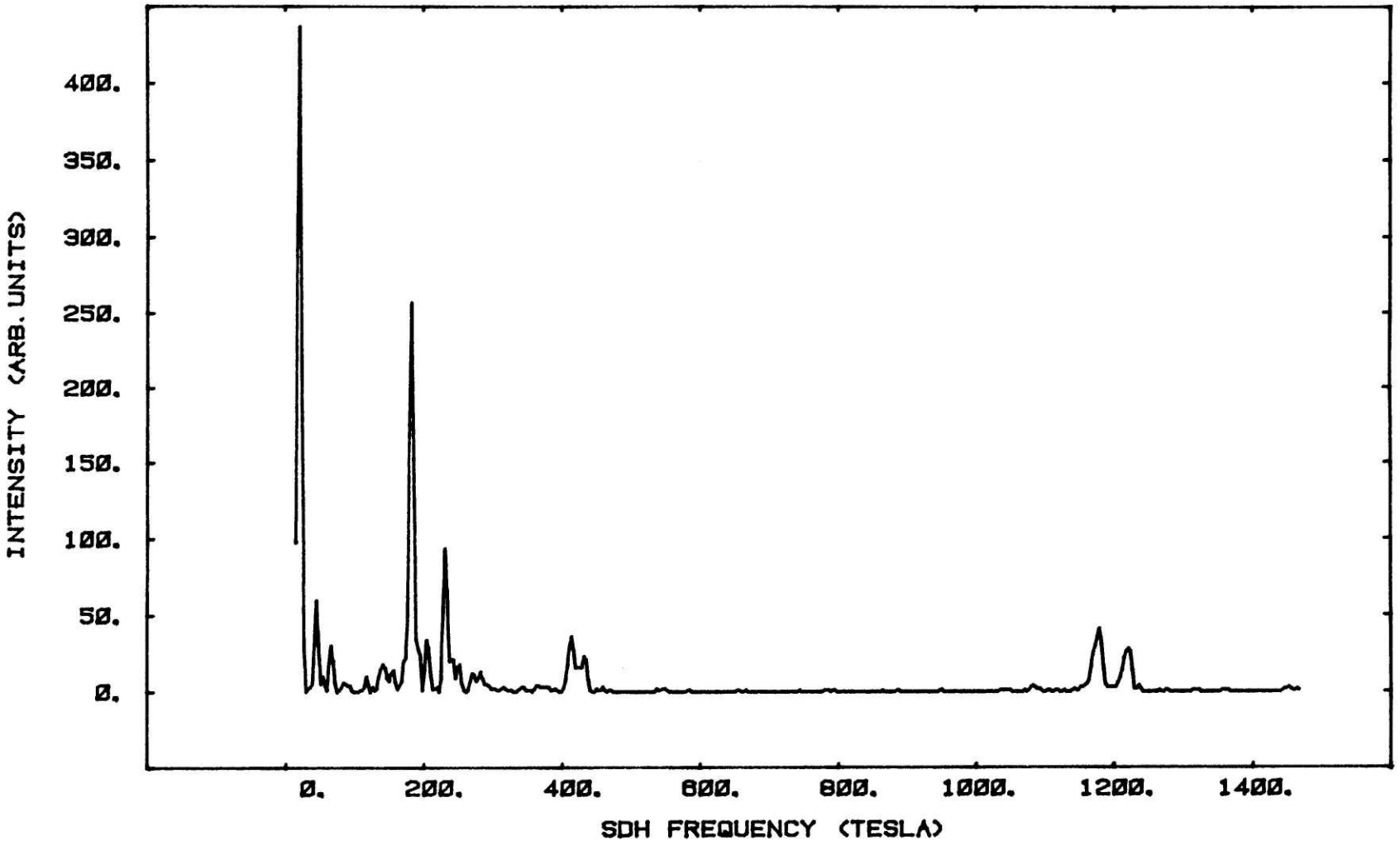


Figure 5.7(a)

The power spectrum of $\rho$ vs 1/H for sample K05.W17 (KTEMP.A) at $\theta = 0°$ and $T = 4.40°K$. This power spectrum corresponds to the trace shown in Fig. 5.8(a). The positions of the peaks are tabulated in Table 5.4.

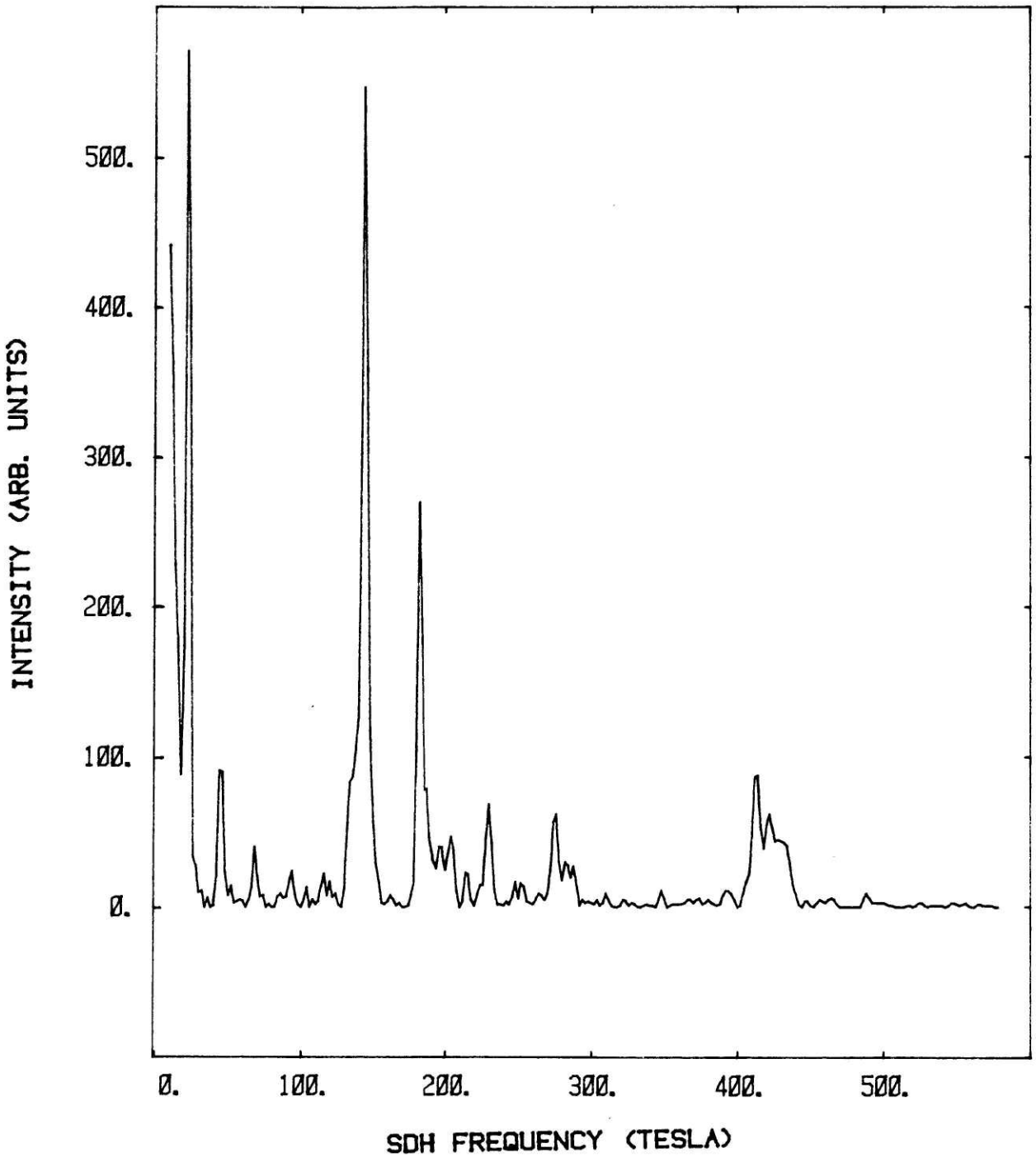


Figure 5.7(b)

The power spectrum of ρ vs 1/H for the other sample (KTEMP.B) on which the temperature-dependent SdH experiment was performed. The positions of the peaks are tabulated in Table 5.4.

to the other K-stage-5 results reported in this chapter [ see Figs. 5.2(a) and 5.5]. Most of the dominant K-stage-5 SdH frequencies are also present in these FFT's. This is especially true for sample KTEMP.B [Fig. 5.7(b)]. But the spectrum for sample KTEMP.A shows significant differences, the major difference being the two new frequencies at $\sim$ 1200T. In the next chapter, comments will be made about the possible origin of these FS cross sections. In Fig. 5.8 , the $\rho$ vs H data are shown for sample KTEMP.A for several temperatures. The y-axis scale is kept fixed in these traces to show the decrease in the amplitude of the oscillations as the temperature is increased.

In order to find the effective masses of the carriers, the amplitudes of the oscillations ($\mathcal{A}$) were analyzed. As explained in section 2.5 the slope of the plot of $\ell n(\mathcal{A}/T)$ vs T (T = temperature) gives the effective mass. It was also discussed in 2.5 that the presence of oscillations at several frequencies complicates the matter. In our case, we do have several frequencies present, and hence to get an approximate measure of the effective masses, the following analysis was done. We note in Fig. 5.8(a) that the oscillations with the frequency $\sim$ 1200T are clearly evident in the field range H $\geq$ 10 Tesla. Also, in the high field range H $\geq$ 14.0T, oscillations with fower frequencies vary flowly. Thus, as an approximation, we assume that the amplitudes shown by arrows on the traces of Fig. 5.8 at H = 14.75T correspond to the cross section with $\nu \sim 1200$ T. The corresponding plot of $\ell n(\mathcal{A}/T)$ vs T for this frequency is shown in Fig. 5.9(a). The experimental points are indicated by ●'s and a least-squares fitted line is drawn through these points. From the slope of this line, and using Eq. 2.33, the effective mass is calculated to be

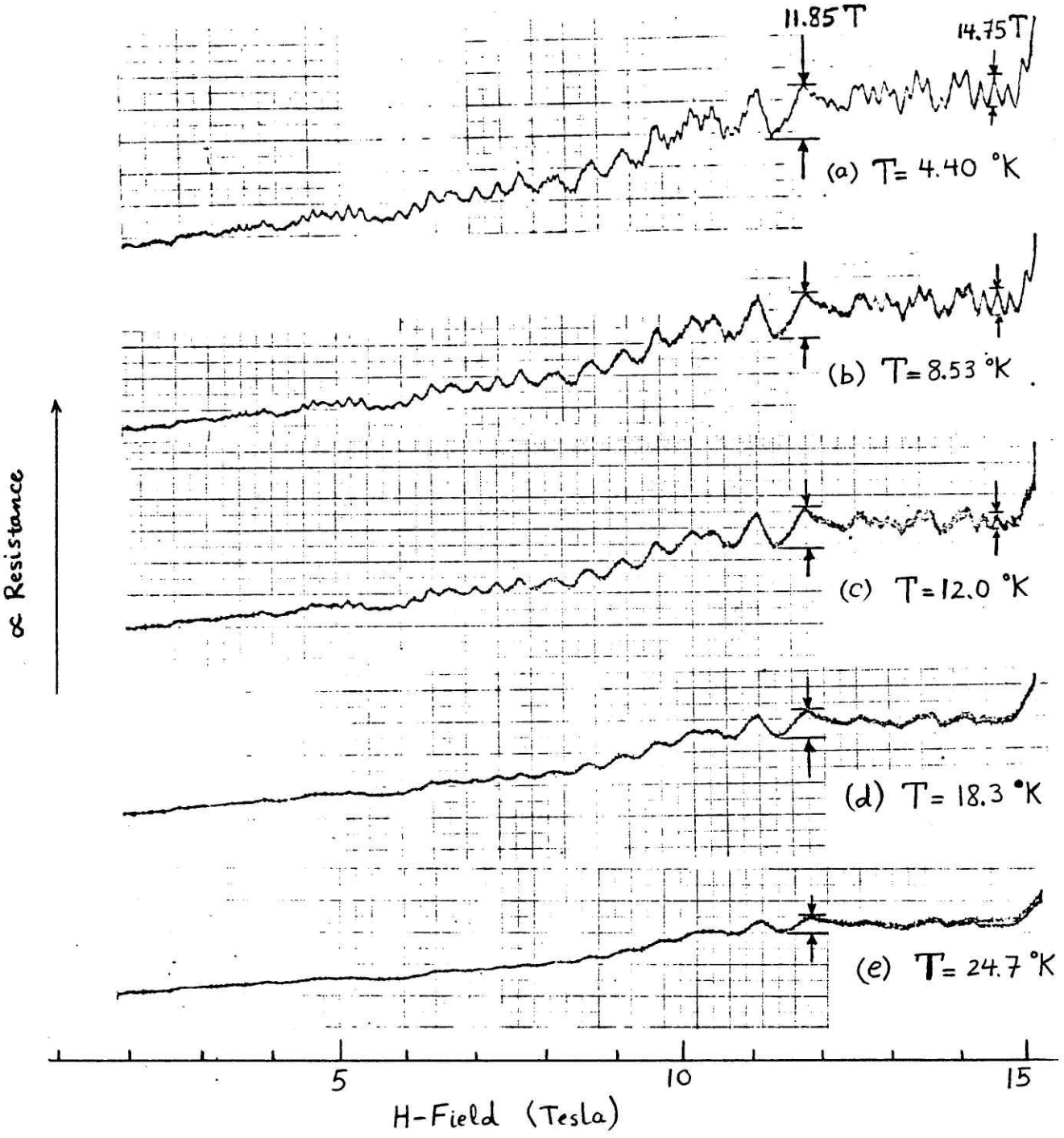


Figure 5.8

The magnetoresistance ( $\rho$ vs H) for the sample KTEMP.A at various temperatures (all at $\theta = 0°$). Note the attenuation of the amplitude of the oscillations as the temperature is increased. The arrows show where the amplitudes for the $\nu \sim 190T$ and $\nu \sim 1200T$ frequencies were measured (see Fig. 5.9).

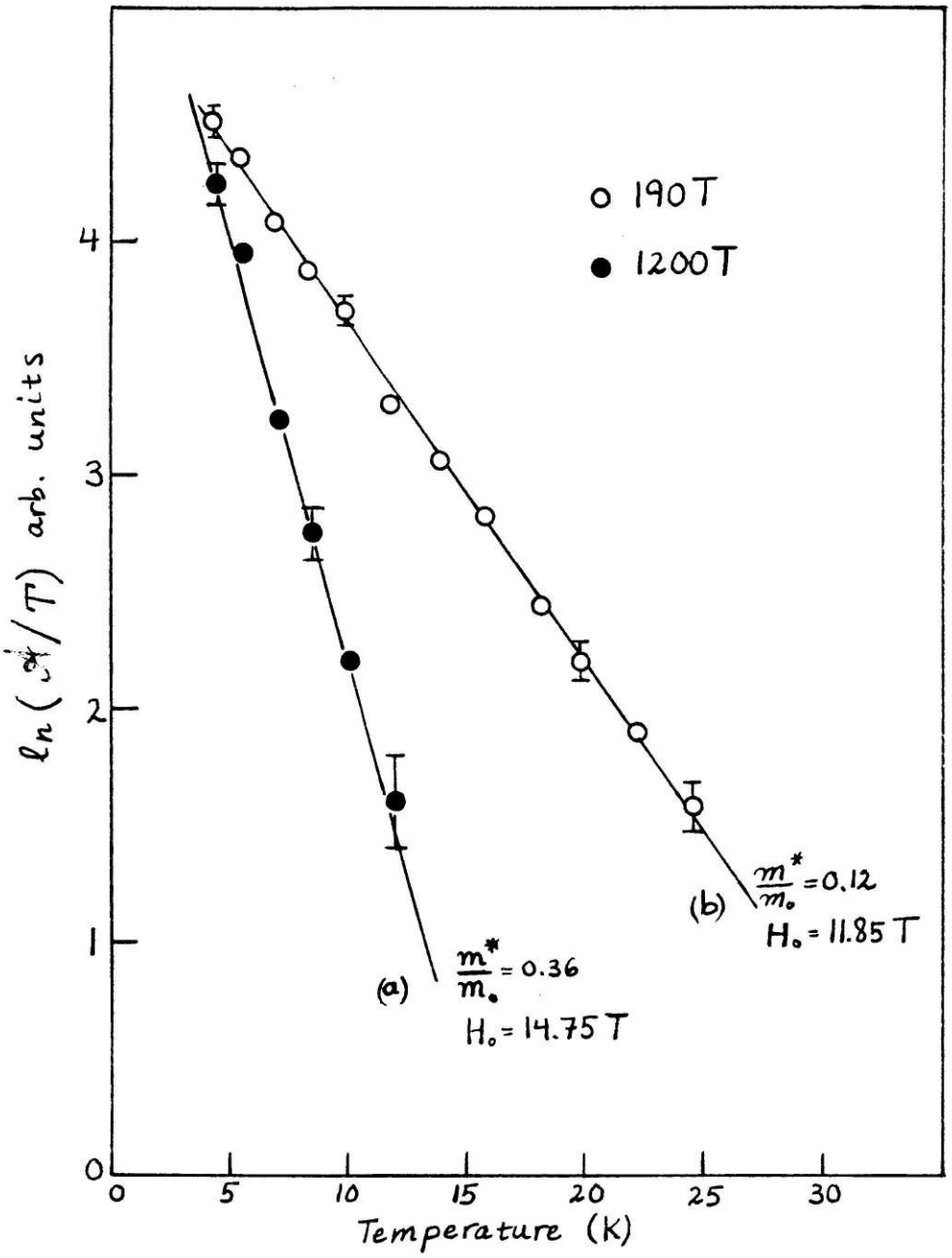


Figure 5.9

Plots of $\ell n(\mathcal{A}/T)$ vs T ($\mathcal{A}$ is amplitude of SdH oscillations in arbitrary units, and T is temperature in °K) for:
a) the $\nu \sim 1200T$ frequency, and (b) the $\nu \sim 190T$ frequency.
The straight lines are least-squares fits to the data points.

$\sim$0.36. The error bars shown are typical, and result from the noise in the measured amplitudes. The same sort of analysis was also done for the $\nu \sim 190$T frequency (shown by the set of arrows at H = 11.85T in Fig. 5.8), and the resulting plot [Fig. 5.9(b)] indicates an effective mass of $\sim$ 0.12. To determine the effective masses associated with the rest of the cross sections, the square roots of the intensity of the peak in the power spectra, which are proportional to the amplitude of the magnetoresistance oscillations, were tabulated at different temperatures. For each SdH frequency, the square root of the intensity ( $\sqrt{I}$) was plotted as in Fig. 5.9 -- i.e., $\ell n(\sqrt{I}/T)$ vs T. Such plots are shown in Fig. 5.10 for the 22, 182, and 1180 Tesla frequencies. As expected, these plots show linear behavior. For $T \leq 7°K$, the experimental points all fall above the straight lines going through the rest of the points. This is due to the fact that at low temperatures ($\leq 7°K$) the large-frequency oscillations have a substantial amplitide [see Fig. 5.8(a)] and hence contribute to some extent to the amplitude of the lower frequency oscillations. Above $\sim 7°K$, the amplitude of these fast oscillations is diminished significantly and thus the intensity of the peak seen in the power spectra at, say, 22T, more closely corresponds to the magnetoresistance amplitude of this cross section.

The straight lines in Fig. 5.10 are again least-squares fitted through the data points (for the 22 and 182T cross sections, the points below 7°K are not included in the least-squares fitting). To find the effective masses, we also need the parameter $H_o$ in Eq. 2.33. Recall that $H_o$ is the value of the field at which we measure the amplitude of the

oscillations. Now we are using the square root of the intensity of the power spectrum ($\sqrt{I}$), which is a measure of the amplitude of oscillations at all field values, rather than being sensitive to the amplitude at a specific field value. Also, note that, since the amplitude of the oscillations is smaller at lower field than at higher values, the power spectrum intensity is more sensitive to the high field oscillations. As an approximation, then, let us assume that the amplitude of the oscillations is an exponential function of inverse field (see Eqs. 2.28, 2.29); that is, $\mathcal{A} \propto e^{-\alpha X}$ where $X = H^{-1}$ (see Fig. 5.11). In this figure, $X_h = H_h^{-1}$ and $X_\ell = H_\ell^{-1}$, where $H_h$ and $H_\ell$ define the field range over which the Fourier transform is taken. As an approximation for $H_o$ (Eq. 2.33), we may use an effective field value $H_{eff} = X_{eff}^{-1}$ which satisfies:

$$\int_{X_h}^{X_{eff}} e^{-\alpha x} dx = \int_{X_{eff}}^{X_\ell} e^{-\alpha x} dx \quad . \tag{5.2}$$

This equation can be solved for $X_{eff}$ thus:

$$X_{eff} = X_h - \frac{1}{\alpha} \ell n \left| \frac{1 + e^{-\alpha(X_\ell - X_h)}}{2} \right| = H_{eff}^{-1} \quad . \tag{5.3}$$

The exponential factor $\alpha$ can be estimated directly by measuring the decaying behavior (as a function of inverse field) of the magnetoresistance amplitude. From Fig. 5.8(a), $\alpha$ is estimated to be $\sim$ 7, 20, and 55T for the $\sim$ 22, 182 and 1180T frequencies. Using these values of $\alpha$, and with $H_\ell$ = 2.0T and $H_h$ = 15.3T, Eq. (5.2) gives $H_{eff}$= 6.4, 9.9 and 12.8T. Substituting these $H_{eff}$ for $H_o$ in Eq. 2.33, we obtain 0.045, 0.11, and 0.33 for the effective masses of the 22, 182, and 1180T cross sections. Note that the effective masses obtained in this fashion are in reasonable

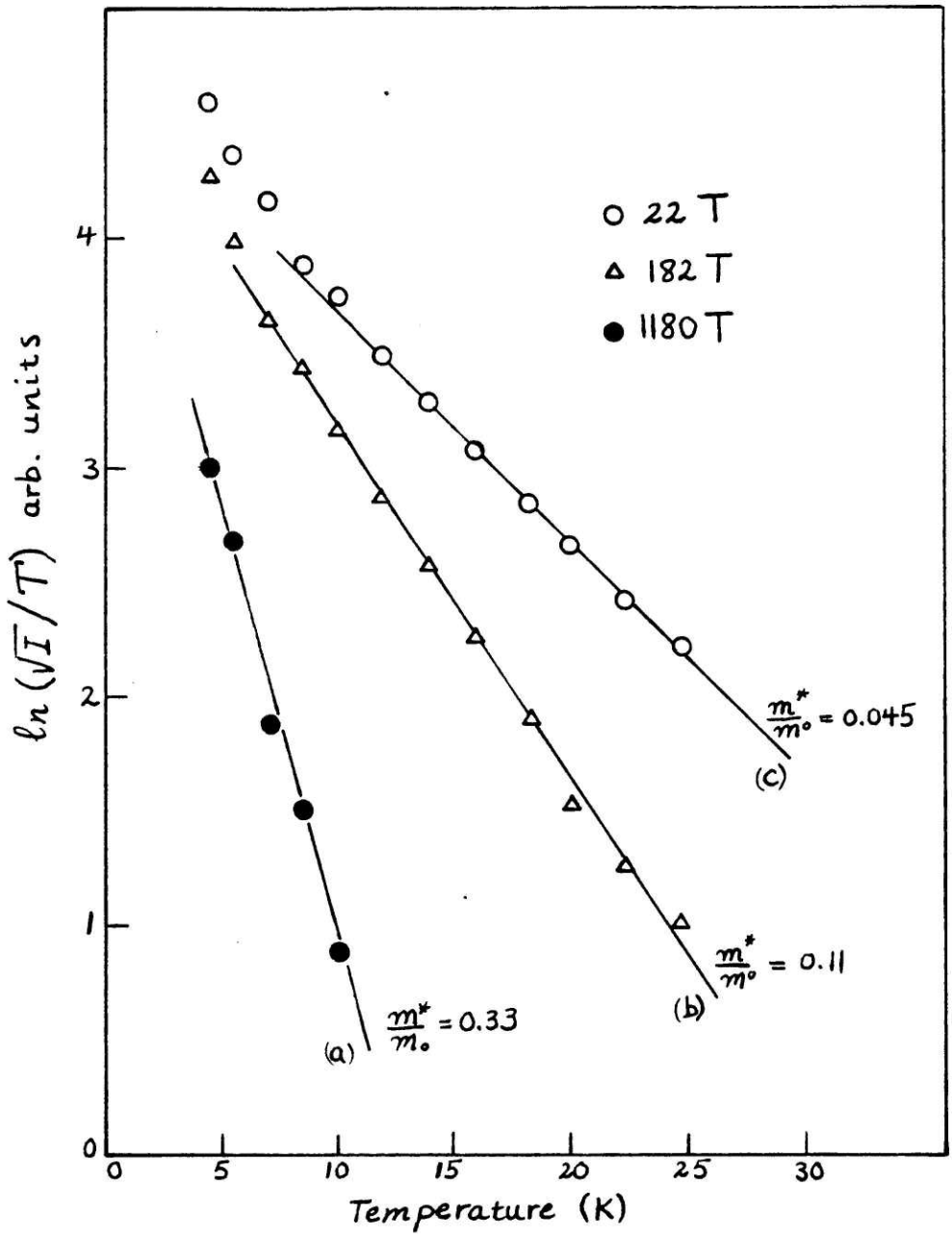


Figure 5.10

Plot of $\ell n(\sqrt{I}/T)$ vs T, where I is the intensity of the peaks in the power spectra for several SdH frequencies: (a) $\nu$ = 1180T, (b) $\nu$ = 182T, and (c) $\nu$ = 22T. The lines are fitted to the experimental points (see text).

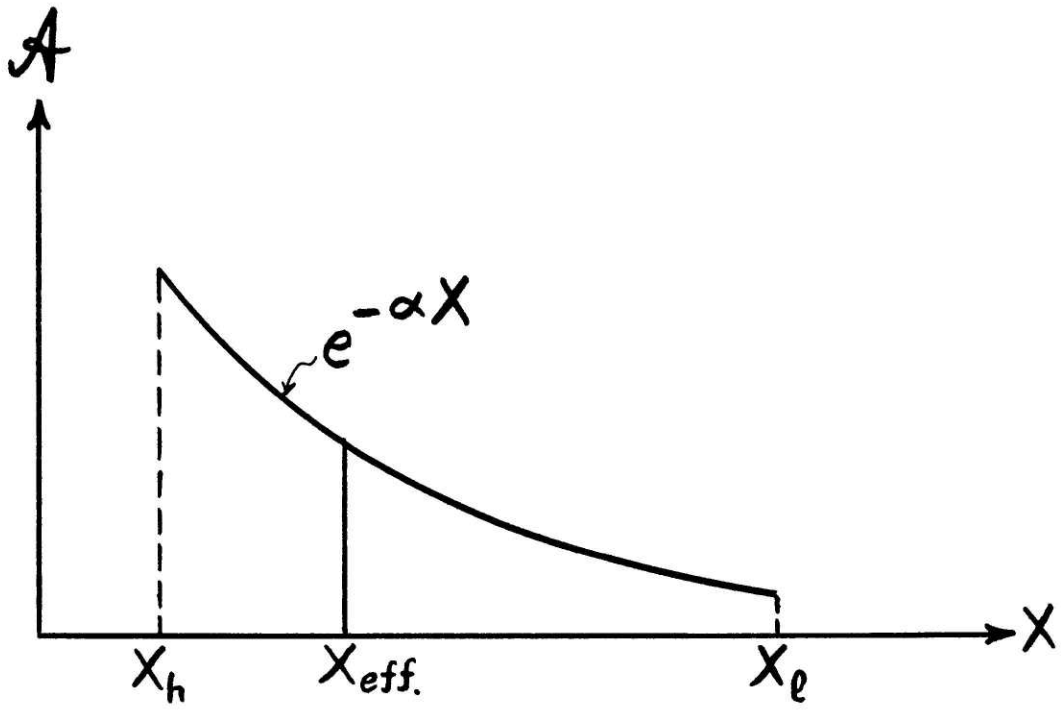


Figure 5.11

Schematic representation of the behavior of the amplitude of the SdH oscillations as a function of inverse field ($X = H^{-1}$). The definition and significance of $X_{eff}$ is explained in the text.

agreement (within $\sim$ 10%) with the values found earlier (Fig. 5.9).

It is not easy to estimate $\alpha$ for the other cross sections because of the interference of the oscillations (see Fig. 5.8). But, $H_{eff}$ can be estimated if we plot $\ell n(\nu_{SdH})$ vs $H_{eff}$ for the above three cross sections (Fig. 5.12). $H_{eff}$ can be approximately found from this plot by drawing a straight line through the three points, and using this line to find $H_{eff}$ at other cross sections ($\nu_{SdH}$). In Table 5.2, the results of the above analysis for the two K-stage-5 samples are summarized. The overall accuracy of the tabulated effective masses is about 20%. In Chapter VI these values will be compared to the theoretically calculated values.

It should be mentioned that, in the cases where the FS is fairly simple and there are only two or three SdH frequencies present, one can try to fit a curve to the experimental magnetoresistance signal. This curve would be based on Eqs. 2.28 and 2.29 (it would be the sum of two or three such terms), and one will have to choose and vary many parameters such as amplitude, frequency, phase, damping factors, etc. for each cross section. Such an analysis has actually been done for pristine graphite, which has a fiarly simple FS [58]. In our case, not only would such an analysis be laborious and impractical, but it is not even clear that it would be rewarding. After all, Eqs. 2.28 and 2.29 are based on many assumptions and simplifications, and they probably do not apply directly to the materials that we are studying because of their fairly complicated Fermi surfaces.

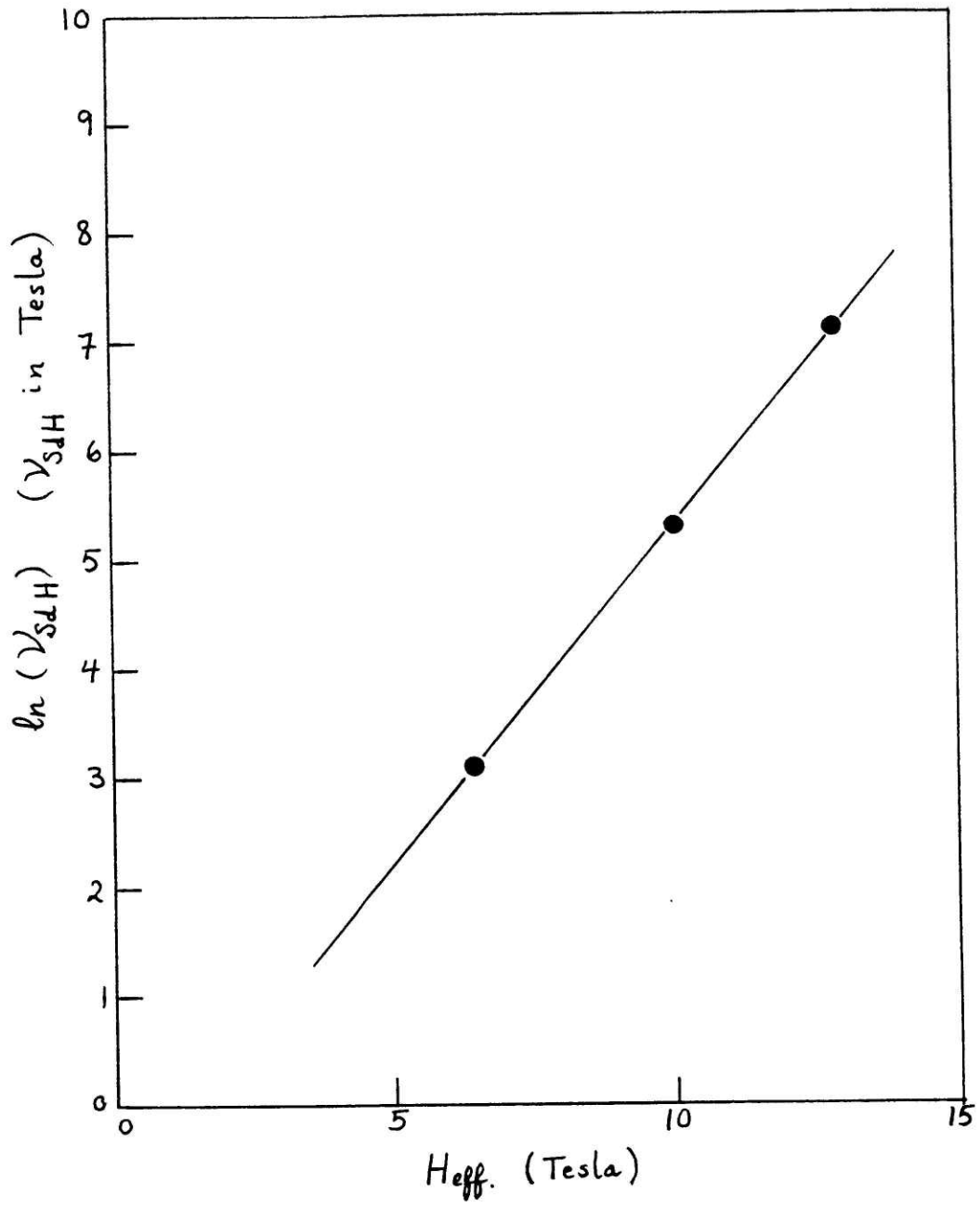


Figure 5.12

Schematic dependence of $H_{eff}$ on $\nu_{SdH}$. The three ●'s represent experimental points. The line is used to estimate $H_{eff}$ for other $\nu_{SdH}$.

| | $\nu_{SdH}$ (Tesla) | Slope (1/°K) | $H_{eff}$ (Tesla) | $\frac{m^*}{m_o}$ |
|---|---|---|---|---|
| KTEMP.A | 22 | 0.104 | 6.4 | 0.045 |
| | 182 | 0.164 | 9.9 | 0.11 |
| | 204 | 0.216 | 10.0 | 0.15 |
| | 230 | 0.181 | 10.2 | 0.13 |
| | {414, 430} | 0.215 | 11.1 | 0.16 |
| | {1180, 1220} | 0.380 | 12.8 | 0.33 |
| KTEMP.B | 22 | - | - | - |
| | 142 | 0.169 | 9.4 | 0.11 |
| | 180 | 0.148 | 9.9 | 0.10 |
| | 230 | - | - | - |
| | 272 | - | - | - |
| | 426 | 0.203 | 11.1 | 0.15 |

Table 5.2

SdH frequencies observed in KTEMP.A and KTEMP.B samples and the effective masses associated with them. The absolute values for the slope(|Slope|) were found from plots such as Fig. 5.10, while Fig. 5.12 was used to estimate $H_{eff}$. The overall accuracy for these effective masses is about 20%.

## V-2. Results for Other Compounds

The SdH experiment was performed on potassium samples of stages 4, 5, and 8 and on rubidium samples of stages 2, 3, 5 and 8. To show that there is signifcant sample- and stage-dependence for the SdH data, the $\rho$ vs H traces corresponding to some of the rubidium and potassium samples are shown in Fig. 5.13. It is evident from this figure, and also the following power spectra in Figs. 5.14 and 5.15, that there is significant change as a function of stage and/or intercalant in the oscillatory behavior of the magnetoresistance for the donor graphite intercalation compounds. In Figs. 5.14 and 5.15, the power spectra for K stages 4,5,8 and Rb stages 2,3,5, and 8 are shown (all for $\theta = 0^{\circ}$ and $T \sim 1.4^{\circ} - 4.2^{\circ}K$). For stage 8 compounds of K and Rb, there are some other frequencies ( > 600T) with very small amplitudes which are not shown in Figs. 5.14 and 5.15. (See Fig. 6.5 for Rb-stage-8 for example.)

The oscillations at these large frequencies can clearly be seen from the $\rho$ vs H data at high fields. (For instance, note the oscillations at $\sim$ 12-14T in the $\rho$ vs H data of K-stage-8 compound shown in Fig. 5.13(c). In Table 5.3, the frequencies (peaks) present in the spectra of Figs. 5.14 and 5.15 are tabulated. The spectra shown in Figs. 5.14 and 5.15 correspond to samples of single stage (as determined by X-ray diffraction before and after the SdH experiment; see Fig. 4.3, for instance.) In addition to these spectra, experiments were performed on some other samples whose stage either changed or was not determined after the experiment. The $\rho$ vs H and power spectpa for some of these samples are shown in Figs. 5.16-18.

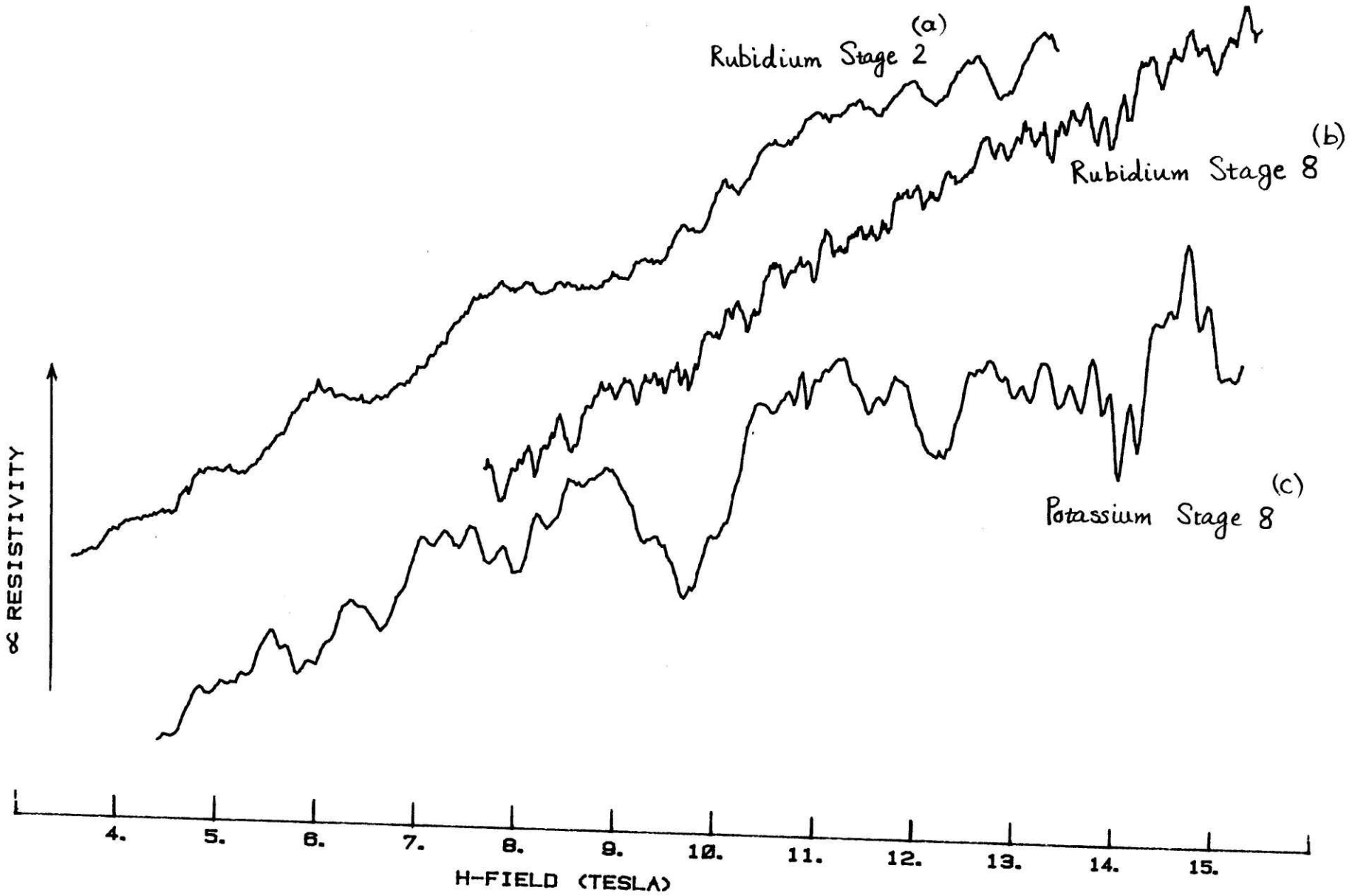


Figure 5.13 The magnetoresistance data for some selected potassium and rubidium GIC. Note the stage and intercalant dependence of the magnetoresistance, especially the oscillatory part. These measurements were all made for $\theta = 0°$ and $T = 1.4 - 4.2°K$.

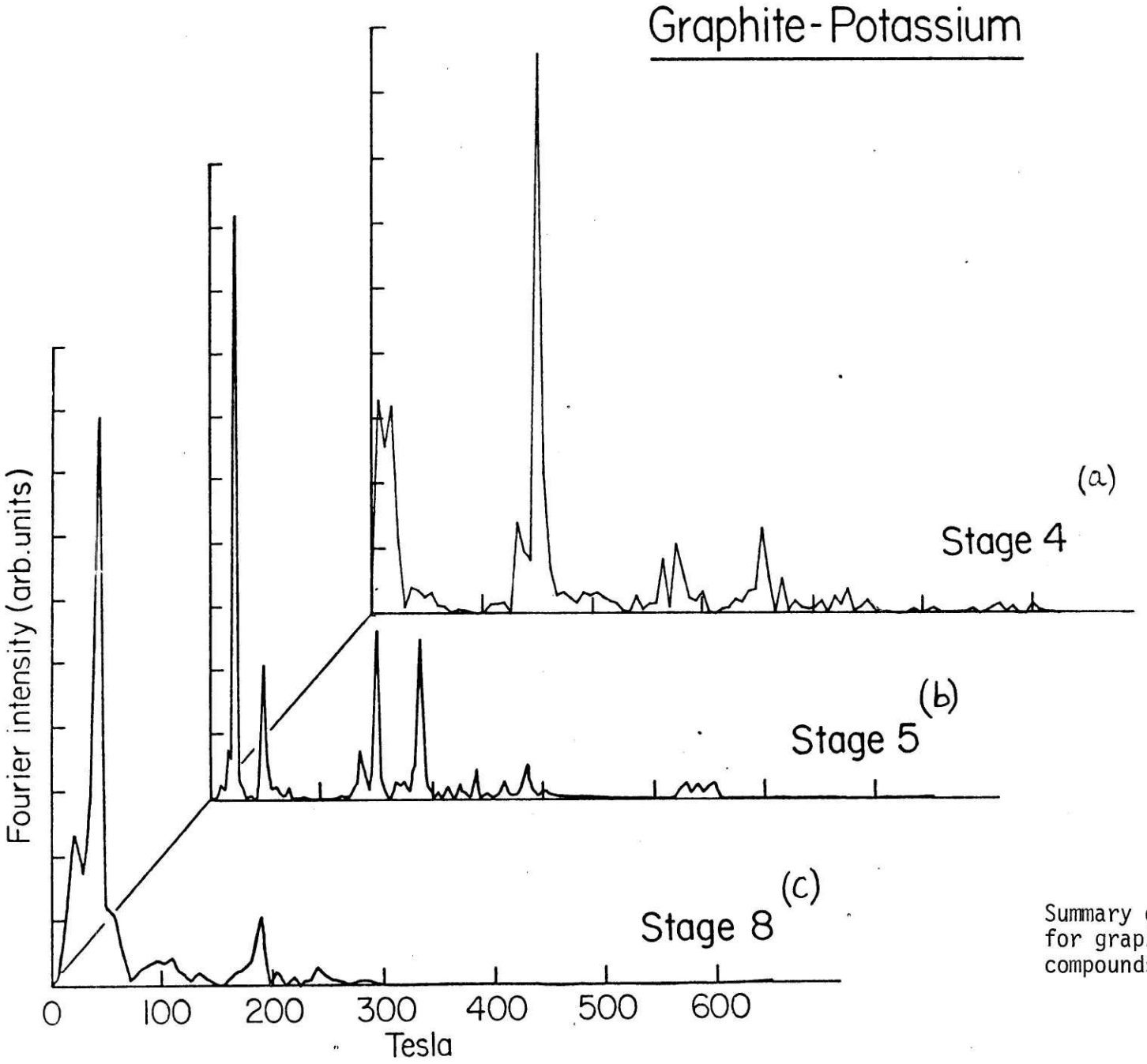


Figure 5.14

Summary of the power spectra for graphite- potassium compounds.

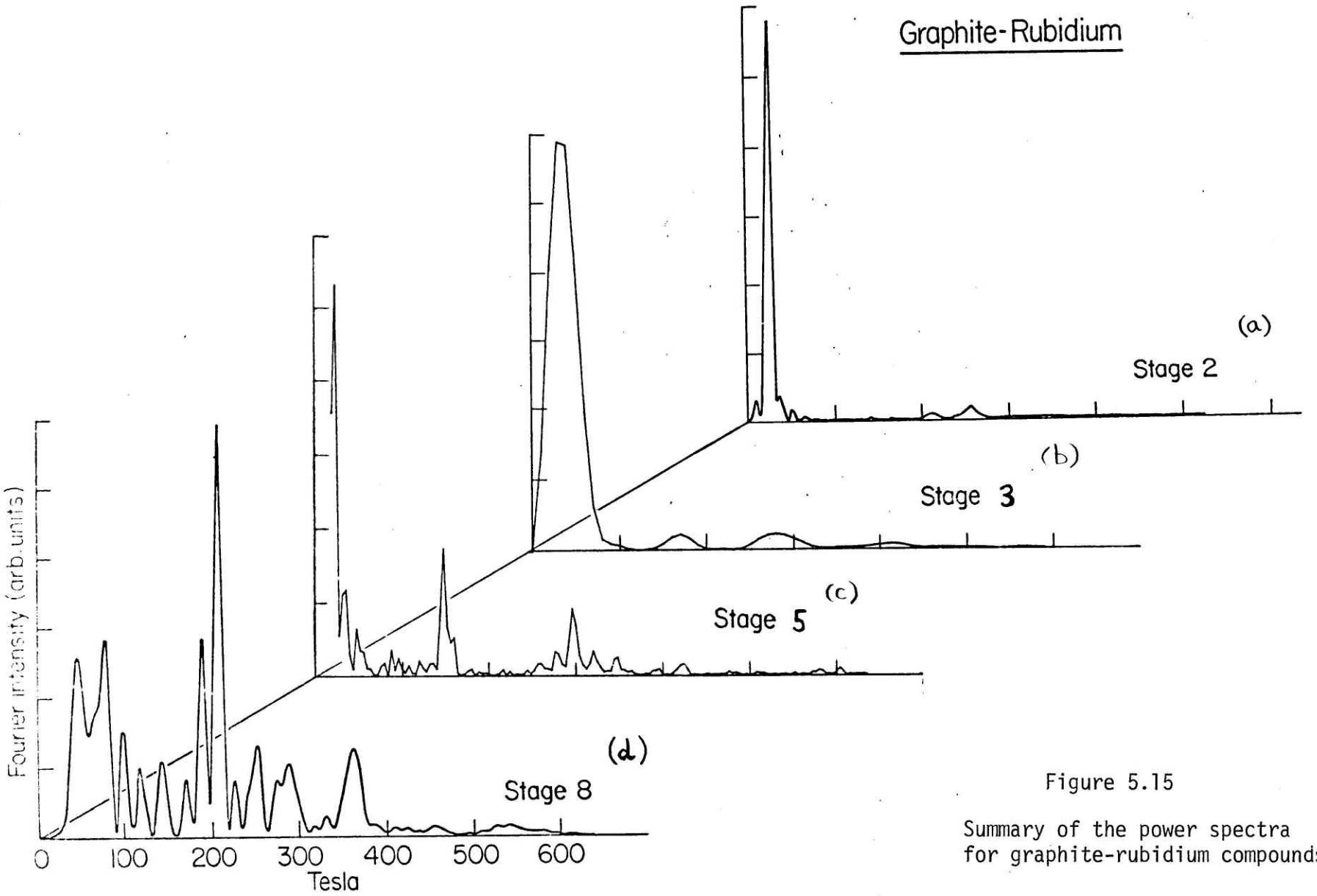


Figure 5.15

Summary of the power spectra for graphite-rubidium compounds

| Graphite-Potassium | | | Graphite-Rubidium | | | |
|---|---|---|---|---|---|---|
| Stage 4 | Stage 5 | Stage 8 | Stage 2 | Stage 3 | Stage 5 | Stage 8 |
| 12 | 18 | 20 | | | | |
| 24 | 24 | | 28 | 35 | 24 | 30 |
| | 48 | 45 | | | 36 | |
| | | 60 | | | | 60 |
| | 71 | 105 | | | 80 | |
| | | | | | | 95 |
| 132 | 135 | | | | | 115 |
| 150 | 152 | | | | | 130 |
| | 172 | | | | 148 | 165 |
| | 191 | 190 | | 170 | | 175 |
| | 213 | 210 | | | | 200 |
| | 224 | | 213 | | | 220 |
| | 243 | 240 | | | | |
| 264 | 267 | | 255 | | | |
| 276 | 290 | 280 | | 260 | 276 | 265 |
| 354 | 302 | | | | 294 | 285 |
| | 430 | 380<br>400 | | | 320 | 325 |
| | 439 | | | | 344 | 355 |
| | 453 | 660 | | 405 | 420 | 380 |
| | | 700 | | | | 450 |
| | | 825 | | | | 860 |
| | | 865 | | | | 900 |
| | | 1015 | | | | 1190 |
| | | 1060 | | | | 1220 |

Table 5.3

Observed SdH frequencies (in Tesla) for potassium and rubidium Graphite Intercalation Compounds (all for $\theta = 0°$). The dominant (high Fourier transform peak intensity) frequencies are underlined.

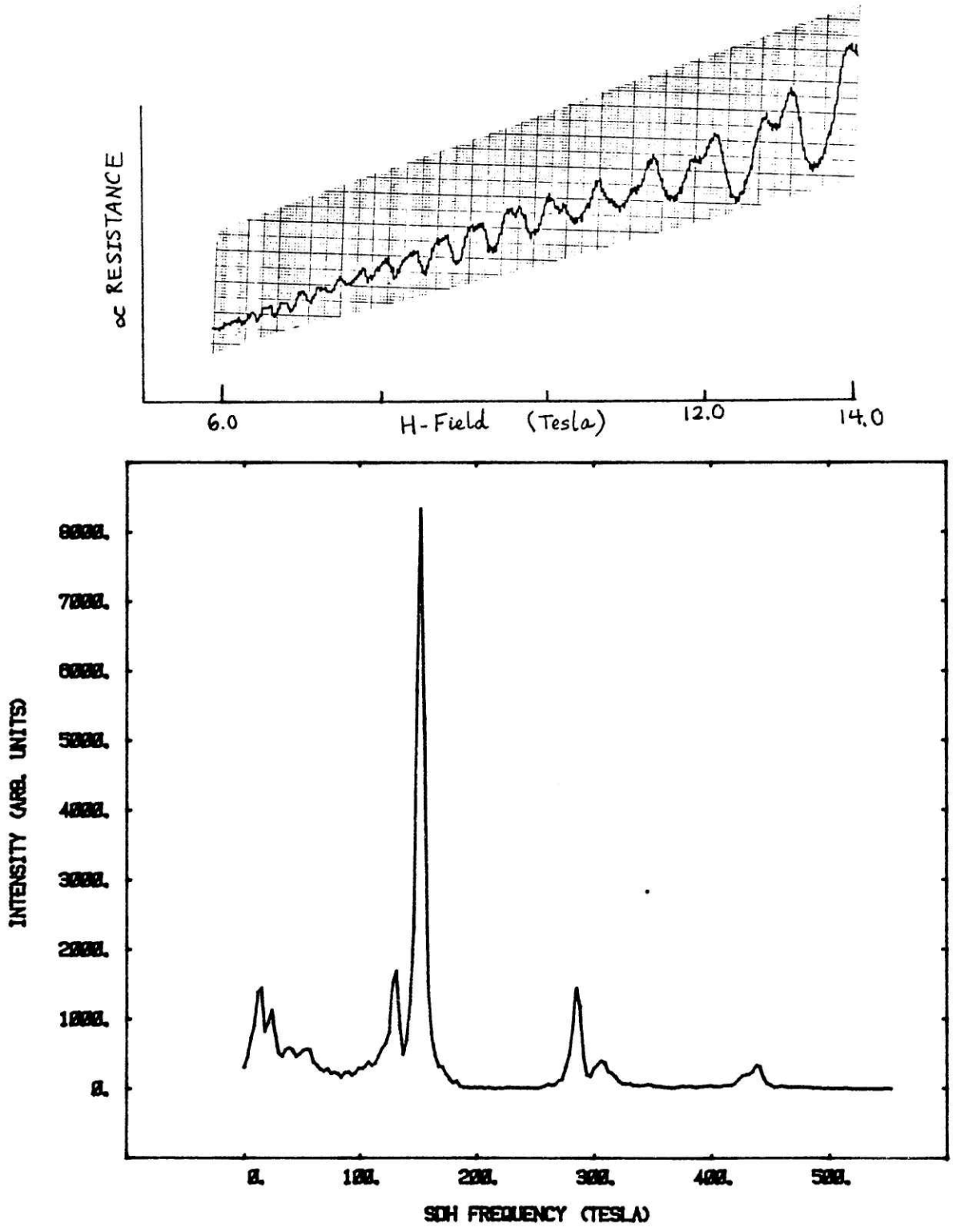


Figure 5.16

The magnetoresistance ($\rho$ vs H) and the power spectrum of ( $\rho$ vs 1/H) for a graphite-potassium compound. The X-ray diffractograms indicated a stage-2 sample before the SdH experiment. However, no X-ray traces were taken after the experiment, hence the stage of the sample during the experiment is not known with certainty.

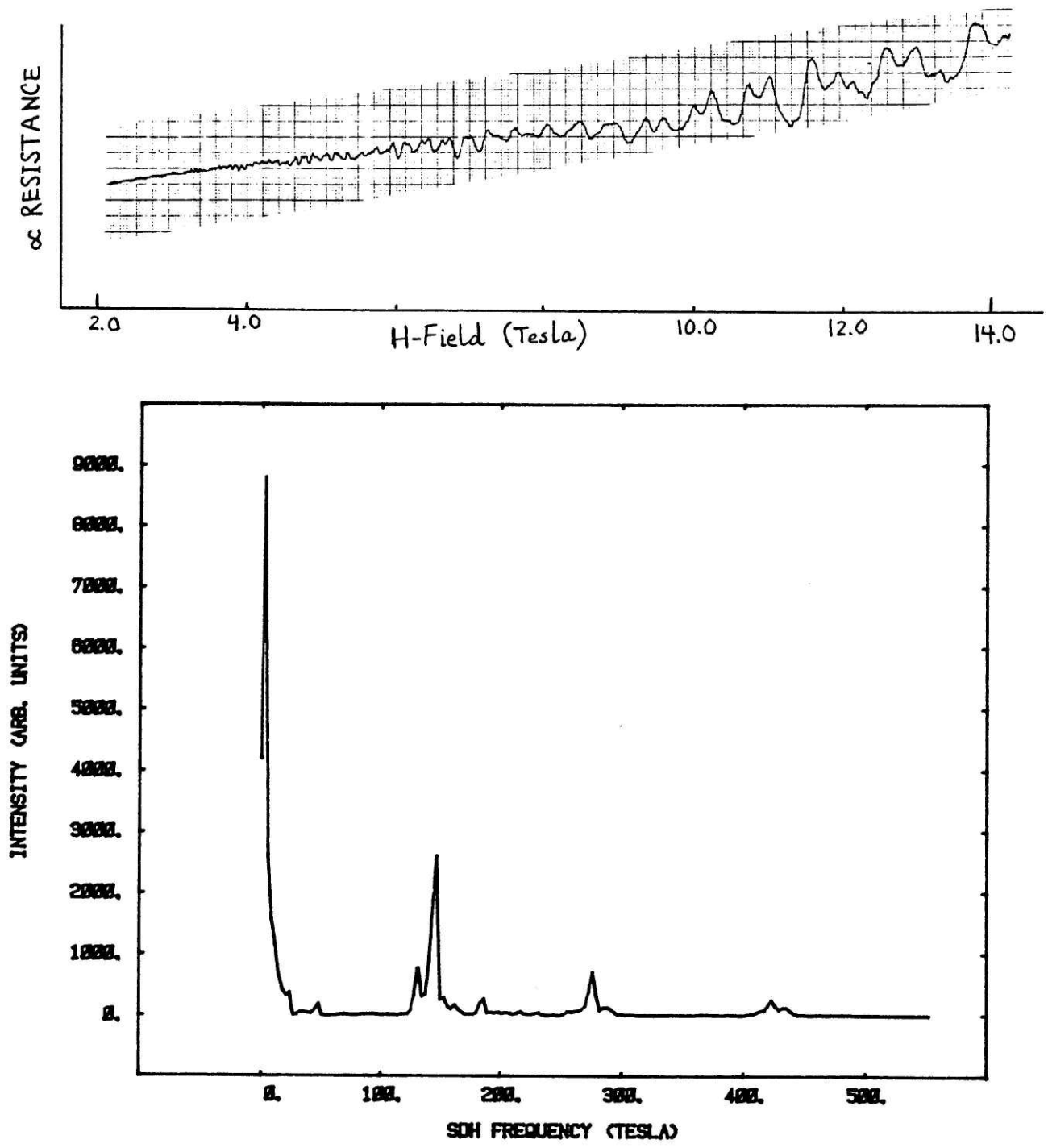


Figure 5.17

The magnetoresistance (ρ vs H) and the power spectrum of (ρ vs 1/H) for a graphite-potassium compound. The X-ray diffractograms indicated a stage-4 compound before the SdH experiment, but a stage-5 (mixed with some stage-4) after the experiment.

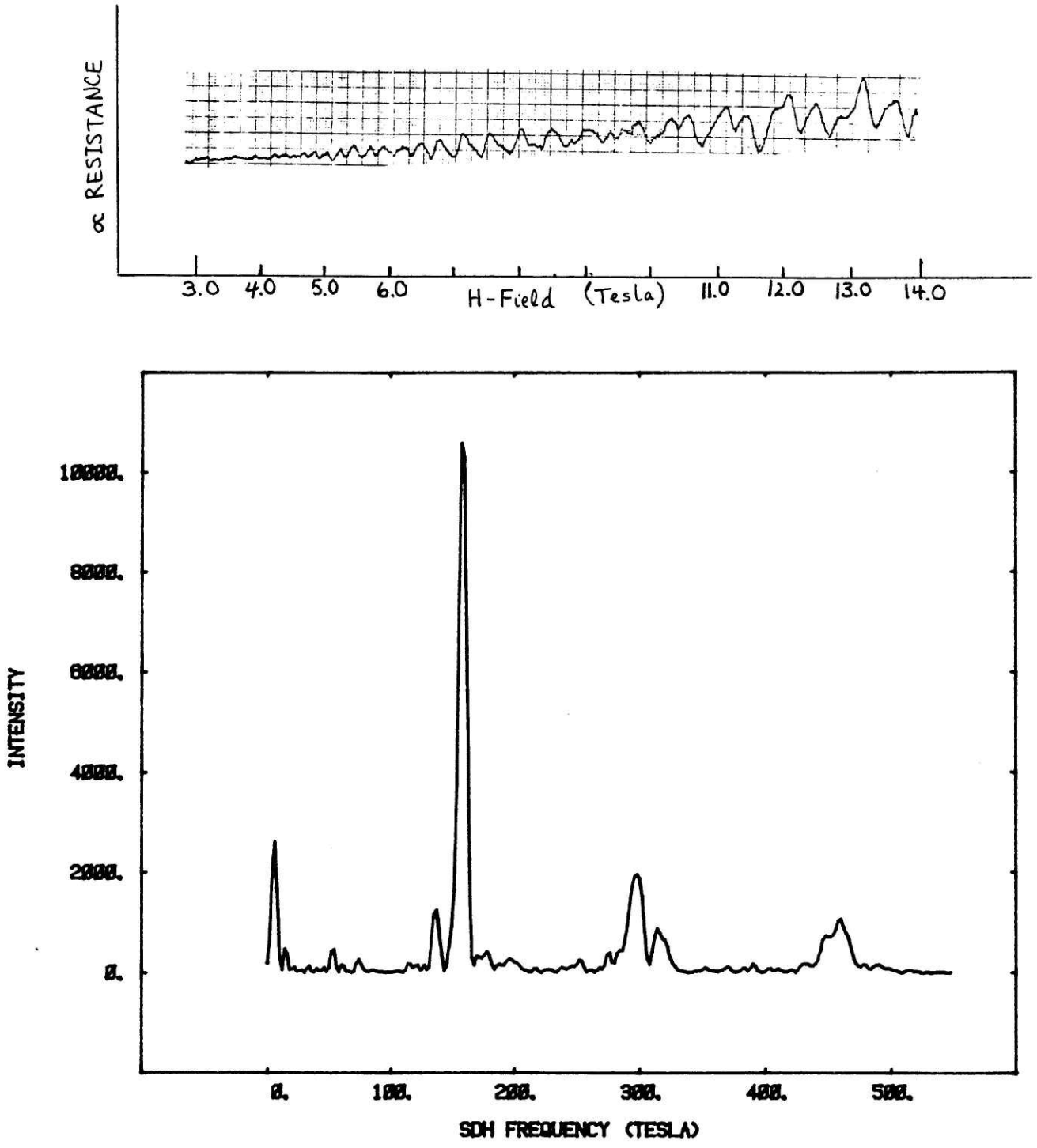


Figure 5.18

The magnetoresistance ($\rho$ vs H) and the power spectrum of ($\rho$ vs 1/H) for another graphite-potassium compound. Again, the X-ray diffractograms showed that the sample had changed from a stage-4 to a mixed stage-5 and -4. The amount of stage-4 contained in this sample after the experiment was more than that present in the sample of Fig. 5.17.

The X-ray diffractogram (taken before the SdH experiment) for the sample in Fig. 5.16 indicated a K-stage-2 compound, but there is no X-ray trace available for this sample after the SdH run. The samples shown in Figs. 5.17 and 18 both X-rayed as nearly single-stage K-stage-4 compounds before they were taken to the dry box to put the leads on, but the X-ray diffractograms after the SdH run indicated a dominantly stage-5 compound, mixed with stage-4. For comparison, in Table 5.4 the observed SdH frequencies for these samples are listed together with the K-stages 4 and 5 compounds from Table 5.3, also, the two samples KTEMP.A and KTEMP.B on which the temperature-dependent measurements were made (see last section).

Note that the frequencies present in the power spectra of Figs. 5.16 to 5.18 are among the dominant frequencies (peaks of greatest amplitude) that also exist in the spectrum for K-stage-5 compound shown in Fig. 5.2(a). In a sample of mixed stage, the fine splitting of the energy levels, which is characteristic of single-stage compounds (see next chapter) is absent and this may explain the absence of spectra with fine structure for the mixed-stage samples.

Another interesting point about these spectra is the behavior of the $\sim$ 190T frequency as one goes from a single-stage 5 to a single-stage 4 compound. Note in Fig. 5.2(a) that, for the K-stage-5 sample, the intensities of the $\sim$ 190T and $\sim$ 150T frequencies are roughly equal. In the spectrum shown in Fig. 5.17 (which corresponds to a K-stage-5 mixed with stage-4), the relative intensity of $\sim$ 190T to $\sim$ 150T frequency is small. This ratio is even smaller in Fig. 5.18, and in Figs. 5.16 and 5.14(a) (for K-stage-4), the $\sim$ 190T peak is completely absent. This observation, and a careful examination of the X-ray diffractograms taken after the SdH experiment, indicate the the $\sim$ 190T frequency can be associated with a K-

| Stage → 4* | 4 | 2(?) | $5_4$ | $5_4$ | KTEMP.A (5?) | KTEMP.B (5?) | 5 | 5 ← Stage |
|---|---|---|---|---|---|---|---|---|
| Figure → | 5.14(a) | 5.16 | 5.18 | 5.17 | 5.7(a) | 5.7(b) | 5.6 | 5.2(a) |
| -- | 12 | 15 | 6 | 3(?) | -- | -- | -- | 18 |
| -- | 24 | 24 | -- | 24 | 22 | 22 | 23 | 24 |
| -- | -- | -- | -- | 48 | 45 | 45 | 46 | 48 |
| 121 | 132 | 132 | 138 | 132 | -- | -- | 135 | 135 |
| 144 | 150 | 153 | 160 | 147 | 150 | -- | 147 | 152 |
| -- | -- | -- | -- | -- | 182 | 180 | 172 | 172 |
| -- | -- | -- | -- | 186 | | | 185 | 191 |
| --- | -- | -- | -- | -- | 204 | -- | -- | 213 |
| -- | -- | -- | -- | -- | 230 | 230 | 220 | 224 |
| 238 | -- | -- | -- | -- | -- | -- | 239 | 243 |
| 264 | 264 | -- | -- | 276 | -- | 272 | 270 | 267 |
| -- | 276 | 285 | 298 | 285 | -- | -- | 285 | 290 |
| -- | -- | 306 | 314 | -- | -- | -- | -- | 302 |
| 338 | 354 | -- | -- | -- | -- | -- | -- | -- |
| -- | -- | -- | -- | 423 | 414 | 426 | 423 | 430 |
| -- | -- | 438 | -- | 435 | 430 | -- | 438 | 439 |
| -- | -- | -- | 460 | -- | -- | -- | 450 | 453 |
| -- | -- | -- | -- | -- | 1180 | -- | -- | -- |
| -- | -- | -- | -- | -- | 1220 | -- | -- | -- |

* Data of Ref. [5].

TABLE 5.4

Observed SdH frequencies (in Tesla) for several potassium compounds at $\theta = 0°$. The first column represents results reported by Tanuma et al[5]; the other samples have all been discussed in this chapter.

stage-5 compound and that the intensity of this frequency becomes weaker as the sample is mixed with lower stages. This conclusion is also verified by looking at Fig. 5.6 which corresponds to a nearly single-stage 5 sample mixed with a very small amount of stage 4 ( $\lesssim$ 2-3% according to X-rays). Also, note that in the spectrum shown in Fig. 5.5, which is for the same stage-5 sample that had the spectrum of Fig. 5.2(a), the above ratio is $\sim 5/3 > 1$. This is expected, in view of the fact that the second experiment (which resulted in Fig. 5.5) was done 10 days after the first [Fig. 5.2(a)] and that no matter how carefully the sample handling was done, the sample was apt to change to higher stage (more dilute).

Finally, note that in the K-stage-8 compound [Fig. 5.14(c)], the $\sim$190T frequency is certainly present as one of the higher intensity peaks in the power spectrum. The same comment applies to the KTEMP.A and KTEMP.B samples, which were exposed to air. In a sense, this frequency can be associated with the graphite interior layer(s)(those which have <u>two</u> graphite layers as the nearest neighboring layers). Note that such layers exist only in compounds of stage $\geq$ 5.

V-3. <u>General Comments about the SdH Results</u>

The first point to be made about the above results concerns the accuracy of the reported results. Since our main interest is the shape of the Fermi surface, or more specifically, the frequencies of the SdH oscillations, then the geometry of the experiment is the most important factor. The two important issues which should be dealt with carefully when doing those SdH measurements are: (1) the calibration of the magnetic field, and (2) the angle between H and the c-axis of the sample. The calibration constants given at the Magnet Laboratory are correct to better than 1% for

the center of the magnet. However, at a distance of one or two centimeters away from the magnet center, the field is reduced by approximately 3 - 7%. Now in the cases when our measurements were done on two or three samples, the stacking of the ampoules containing the samples on top of one another resulted in not having all of them exactly at the center of the magnet. Also, the presence of Stycas on the ampoule (see Fig. 4.2) sometimes made it difficult to have all the c-axes of the samples aligned and hance corrections for the angular dependence measurements had to be made. In general, a very practical way to determine the position $\theta = 0°$ ($\vec{H} \parallel \vec{c}$) is to do the SdH measurements for both positive and negative $\theta$. Unless the Fermi surface is spherical, there will usually be an extrema in the observed frequencies at $\theta = 0°$. Thus, either by eye or by fitting a parabola through the frequencies observed near $\theta = 0°$, the position at $\theta = 0°$ can be determined. This was, in fact, done for sample K05.Y03, and the frequencies given in Table 5.1 are the corrected values.

Another factor that determines the accuracy of the results is the resolution (in frequency) in the power spectra. This resolution is usually a few Teslas (see Appendix A) and for most frequencies, is less than 1-2% of the value of the frequency. The overall accuracy for the results, then, is dependent on the experimental conditions and the amount of data available (for angular dependence). However, a general accuracy of about 5-10% is estimated for most of these results. The same remarks apply to the accuracy of the reported SdH frequencies in the temperature-dependent measurements. The accuracy for measuring the temperature was $\Delta T/T \lesssim 0.5\%$ [57].

Another general comment about these results is that very often, because

of the weakness of the signal, it was not possible to do complete angular dependence measurements. In the few cases that the angular dependence was measured (such as samples of Figs. 5.5 and 5.16-5.18), the frequencies showed a behavior very similar to that shown in Fig. 5.4 (K-stage-5 compound). This similarity is compatible with the models for the Fermi surface, as will be discussed in the next chapter in more detail.

# VI. INTERPRETATION OF THE SdH RESULTS USING ENERGY BANDS, MODELS AND CONCLUSIONS

In the first section (6.1) of this chapter, a brief review of some of the results reported by other workers about the Fermi surface (FS) of the graphite intercalation compounds is presented. Section 6.2 deals with the detailed application of the two energy-band models (discussed in section 2.4) to the K-Stage-5 sample. This is followed in 6.3 by presenting the results of similar analyses for the other compounds studied in this project. A summary of conclusions based on this work is given in the final section (6.4) and topics of interest for future study are suggested.

## VI-1. Brief Overview of Some Previous Results on the Fermi Surface of GIC and Their Interpretations

The aim of this section is to give a general perspective of the experimental results and their interpretations reported by other authors with regard to the Fermi surface (FS) of the graphite intercalation compounds (GIC). As briefly discussed in Chapter I, the FS of many donor and acceptor GIC has been studied, mostly by the measurements of the quantum oscillatory effects in these compounds. These results have generally emphasized either the stage-dependence or the stage-independence of the observed Shubnikov-de Haas (SdH) frequencies.* The dependence or independence of the SdH frequencies on stage has significant implications on the FS models used to interpret the experimental data, as will be briefly discussed.

---

* Here the author is using "SdH frequency" as a general term for the frequency of oscillations in the quantum oscillatory phenomenon (see Chap. II). Also, "SdH frequency" and "FS cross section" will be used as equivalent terms. Indeed, from Eq. 2.31 it may be noted that they are related by a universal constant.

The stage-independent SdH frequencies have been reported only for acceptor GIC, such as $Br_2$ [3-5,14], $SbCl_5$[10], and $FeCl_3$[9]. The measurements on $Br_2$ were carried out on dilute samples which were not well characterized. For $FeCl_3$ and $SbCl_5$ compounds, however, the experiments were done on samples which were characterized for stage index. The numerous frequencies (up to 11 for $Br_2$-GIC [14]) reported are in the range $10T \lesssim \nu \lesssim 600T$ for the above compounds.

A basic approach to interpret these stage-independent results has been suggested by Batallan et al [10] and by Bok [59]. In their proposed model, it is assumed that all the charge released by the intercalate resides in the graphite bounding layers and that these layers effectively screen the charge from the interior layers. Thus, a metallic sandwich is present about the intercalate layer, which plays a dominant role in the elecrronic properties of the compound - including the quantum oscillations. To account for the observed stage-independent frequencies, these authors [10,14,59] use a nearly free electron model together with in-plane zone-folding. Such a model, in general, predicts few frequencies and thus, in their interprepation, many of the observed frequencies are identified as harmonics or combination modes (associated with magnetic breakdown phenomena).

The SdH frequencies observed in donor compounds*[5,8] and some acceptor compounds such as $AsF_5$ -GIC [11,16] are reported to be stage-dependent. These frequencies are also numerous and the number of

* Also note that not all authors agree on results for a given intercalant; for example, the recent work by Iye and Tanuma [60] on $SbCl_5$-GIC shows stage-dependent frequencies, while authors of Ref. 10 report stage-independent results.

observed frequencies increases with increasing the stage index. The simplest model used to interpret the stage-dependent SdH frequencies is one based on the Dilute-Limit Model and zone-folding, as discussed in section 2.4.1. This model, which will be denoted by model I in this thesis and will be discussed in the next section in more detail, was first presented by McClure [21] and later used by Tanuma et al [5] to interpret the SdH frequencies observed in graphite-potassium compounds. The results of their analysis for the K-stage-4 compound and a similar analysis for a $AsF_5$-Stage-3 compound [11] are shown in Table 6.1. The details of such analysis will be discussed fully in the next section, when we apply this model to our experimental data. Said briefly, the $\pi$-bands of graphite are used (Fig. 2.4) and the Fermi level $E_F$ is raised for the donor compound (K-GIC) and is lowered for the acceptor compound ($AsF_5$-GIC) relative to $E_F$ for pristine graphite (-0.024 eV). The Fermi levels are determined by the requirement that the largest predicted SdH frequency coincides with the largest observed frequency. The smaller calculated frequencies are then identified with c-axis zone-folding (see Fig. 2.8). Using Eq. 2.16, the carrier density for each compound is calculated. Assuming chemical formulae $C_{48}K$ and $C_{24}AsF_5$ (the carbon in-plane density is assumed to be $C_{12}$ and $C_8$ for these compounds, respectively), the charge-transfer rate from the intercalate layer to the graphite layers (f) is found ($f = 1$ corresponds to complete ionization). The reader is reminded again that full details of the above analysis are given in the next section.

In the following sections, comments will be made about the agreement between the number and the values of the predicted frequencies (by this model) when analyzing our data. Most of these comments also apply to the

| SdH Frequency (T) | |
|---|---|
| $\nu_{observed}$ | $\nu_{calculated}$ |
| 338 | 338 |
| 264, 238 | 289 |
| 144, 121 | 143 |
| $C_{48}K$ (stage 4) | |
| $E_F = 0.42$ eV | |
| $n_e = 4.24 \times 10^{20}$ cm$^{-3}$ | |
| $f = 0.21$ | |

(a)

| SdH Frequency (T) | |
|---|---|
| $\nu_{observed}$ | $\nu_{calculated}$ |
| 877, 833 | 877 |
| 580, 513 | 516 |
| 109, 101, 72 | 98 |
| $C_{24}AsF_5$ (stage 3) | |
| $E_F = -0.611$ eV | |
| $n_h = 1.04 \times 10^{21}$ cm$^{-3}$ | |
| $f = 0.22$ | |

(b)

Table 6.1

The observed and calculated SdH frequencies reported by Tanuma et al [5] for a K-stage-4 compound and by Iye et al [11] for $AsF_5$ -stage-3. The calculated frequencies are the results of the application of the Dilute-Limit Model by these authors.

results in Table 6.1. It is evident from this table that the agreement between the observed and calculated frequencies is quite good, giving qualitative support for the use of this model.

An important point to be made about the results in Table 6.1, however is the small value of the fractional charge transfer ratio f found by these authors ($f \cong 0.20$). Their similar analysis of their data for compounds of other stage also indicates a small f. For instance, they report f values of 0.22 and 0.26 for $C_{24}AsF_5$ (stage 3) and $C_{32}AsF_5$ (stage 4) compounds. As we will see in the following sections, the analyses of our data also indicates small values of f ( $\sim$ 0.07 to 0.4). It is important to note, however, that such small f values are the result of assuming that all the carrier pockets present are those observed in the SdH experiments. There may be other carrier pockets, possibly elsewhere in the BZ and away from the KH axes, which are not seen in the SdH experiments. (See section 6.4 ) If such pockets exist, f will be higher than what is calculated here.

## VI-2. Analysis of SdH Results for a Potassium-Stage-5 Compound

The material presented in the last section was intended to serve as a background and to set the perspective for the interpretation of our experimental data, which will now be presented. In this section we use the two models of section 2.4 to interpret the FS parameters of sample KO5.YO3 (Table 5.1) at $\theta = 0°$. The experimental results for this sample are used because they are the most reliable of those reported in this thesis.

We first use the "Dilute-Limit Model " (Model I) of section 2.4.1 to interpret the observed SdH frequencies. As explained in that section, we start the analysis by raising the Fermi level $E_F$ to the point where the largest cross-sectional area of the FS isequal to the largest cross section that is experimentally observed. This $A_{max}$ is at the K-point [area $S_1$ in Fig. 2.8(c)] and thus $E_F$ is the solution to Eq. 2.15:

$$A^e_{max}\ (\xi = 0) = \frac{4\pi}{3a_o^2\,\gamma_o^2}\ \frac{(E_3-E_F)(E_2-E_F)}{(1+2\gamma_4/\gamma_o)^2} = \frac{2\pi e}{\hbar c}\ \nu_{max} \qquad (6.1)$$

where $\nu_{max}$ is the maximum SdH frequency observed. The values for band parameters used are those of Table 2.1 with $\gamma_3 = 0$. Note that Fig. 2.7 is based on Eq. 6.1, taking $E_F$ and $\nu_{max}$ to be the coordinate variables. The next step is to introduce zone folding along the $k_z$-direction and to find the cross sections of the FS at the new zone boundaries (see Fig. 2.8 for a stage-4 compound). These cross sections are given below in Eq. 2.15:

$$A^e(\xi) = \frac{4\pi^2}{3a_o^2\,\gamma_o^2}\ \frac{(E_3-E_F)(E_2-E_F)}{(1+\nu)^2} \qquad (2.15)$$

where here $\xi$ takes values:

$$\xi_i = \frac{1}{2}\frac{I_c^\circ}{I_c}\,i \qquad (i = 1,2,\ \ldots\ M) \qquad (6.2)$$

where $I_c^\circ$ and $I_c$ are the lattice parameters of pristine graphite (6.70Å) and the intercalation compound along the z-direction. The largest value of i in Eq. 6.2, M, gives the smallest non-negative cross section. In Table 6.2 the result of the above analysis for sample K05.Y03 (Table 5.1) is summarized.

| | | SdH Frequency (T) | |
|---|---|---|---|
| $\xi$ | $S_i$ | $\nu_{calculated}$ | $\nu_{observed}$ |
| 0 | $S_1$ | 453 ⟷ | 453 |
| 0.1787 | $S_2$ | 412 | 439<br>430 |
| 0.3573 | $S_3$ | 304 | 290<br>267<br>243 |
| 0.5360 | $S_4$ | 157 | 191<br>152<br>135 |
| — | — | — | 24<br>18 |

$E_F = 0.505 eV$ ; $n = 5.85 \times 10^{20} cm^{-3}$ ; $f = 0.30$

Table 6.2

The observed SdH frequencies for the K-stage-5 compound and their comparison with the calculated frequencies resulting from the application of the Dilute-Limit Model (model I).

$E_F$ is determined to be 0.505eV. With $E_F$ at this level, the model predicts four extremal cross sections: $S_1$, $S_2$, $S_3$ and $S_4$. In this table, the dominant observed frequencies for sample K05.Y03 are also written. The fairly good agreement between the observed and calculated frequencies is an indication of the validity of the Dilute-Limit Model for the stage 5 sample which is evidently a dilute compound. Note that the model as used corresponds to a FS similar to Fig. 2.8(b), where no splittings at the new zone boundaries due to the periodic potential of the superlattice are made. If these aplittings are considered, then the cross sections $S_2$, $S_3$ and $S_4$ will each be replaced by a pair of cross sections of nearly equal areas [Fig. 2.8(c)]. This could explain the presence of some of the numerous observed frequencies that are grouped in Table 6.2.

With $E_F$ = 0.505eV, we can use Eq. 2.16 or Fig. 2.6 to find the carrier density, which is found to be $n = 5.85 \times 10^{20}$ cm$^{-3}$. To get an estimate of the rate of charge transfer from the intercalate (potassium) layer to the graphite layers, we also calculate the total charge (1 electron/K atom) that is available for donation to the graphite layers, assuming a chemical composition $C_{\alpha n}K$ where n is stage and $\alpha$ is the in-plane density. $\alpha$ has been found to be $\sim 10.5$ for potassium compounds (with $n \geq 2$) [61] and thus, for a K-stage-5 compound, we find:

$$n' = \#\text{carriers/cm}^3 = \frac{1}{\text{Vol. of Prim. cell}} = \left(\frac{\sqrt{3}}{2} a^2 I_c\right)^{-1} = \left(\frac{\sqrt{3}}{2} \frac{\alpha}{2} a_o^2 I_c\right)^{-1}$$

$$= 1.94 \times 10^{21} \text{cm}^{-3} \qquad (6.3)$$

Here, n' is the carrier density that we would have if there were a complete transfer of charge from the intercalate to the graphite layers.

The ratio $n/n' = f \cong 0.30$ gives an estimate for the fractional charge transfer from the potassium layer into the graphite layers. Note that such an f value is in general agreement with Tanuma's value for a K-stage-4 compound (see Table 6.1). More will be said about the f value later on in this chapter.

In order to see explicitly how the cross sections $S_i$ in Table 6.2 vary as a function of $E_F$, in Fig. 6.1, $S_i$ are plotted vs $E_F$. To draw these curves, $E_F$ is successively increased, from 0.30eV to 1.0eV, and for each value of $E_F$, Eq. 2.15 is used to find $S_i$ at $\xi_i$ values given by Eq. 6.2. Horizontal lines correspond to the (dominant) experimentally observed SdH frequencies, while the vertical solid line is drawn at the determined Fermi level $E_F = 0.505$eV. Once such a diagram is available, we can easily see how the different SdH frequencies (FS cross sections) behave as $E_F$ is changed. We note, for example, that if we increase $E_F$ to approximately 0.56eV, the model will predict an SdH frequency of $\sim$20T (from the $S_5$ branch) in accordance with the observed frequencies (24T). However, the other frequencies, from branches $S_1$ - $S_4$, will all be shifted to larger values, and also a larger f value will result.

A curious situation would be to raise $E_F$ to a value which results in a carrier concentration of $1.94 \times 10^{21}$ $cm^{-3}$, i.e., an f value equal to unity. The vertical dahsed line in Fig. 6.1 at $E_F = 0.970$eV corresponds to this case. We see that, except for $S_5$ and $S_6$, all other predicted cross sections fall above the observed values. With $E_F = 0.970$eV, the largest cross section, $S_1$, is predicted to be $\sim$ 1165T! No such frequency was observed in the several encapsulated single-stage-5 potassium compounds that were studied. It is interesting, however, to

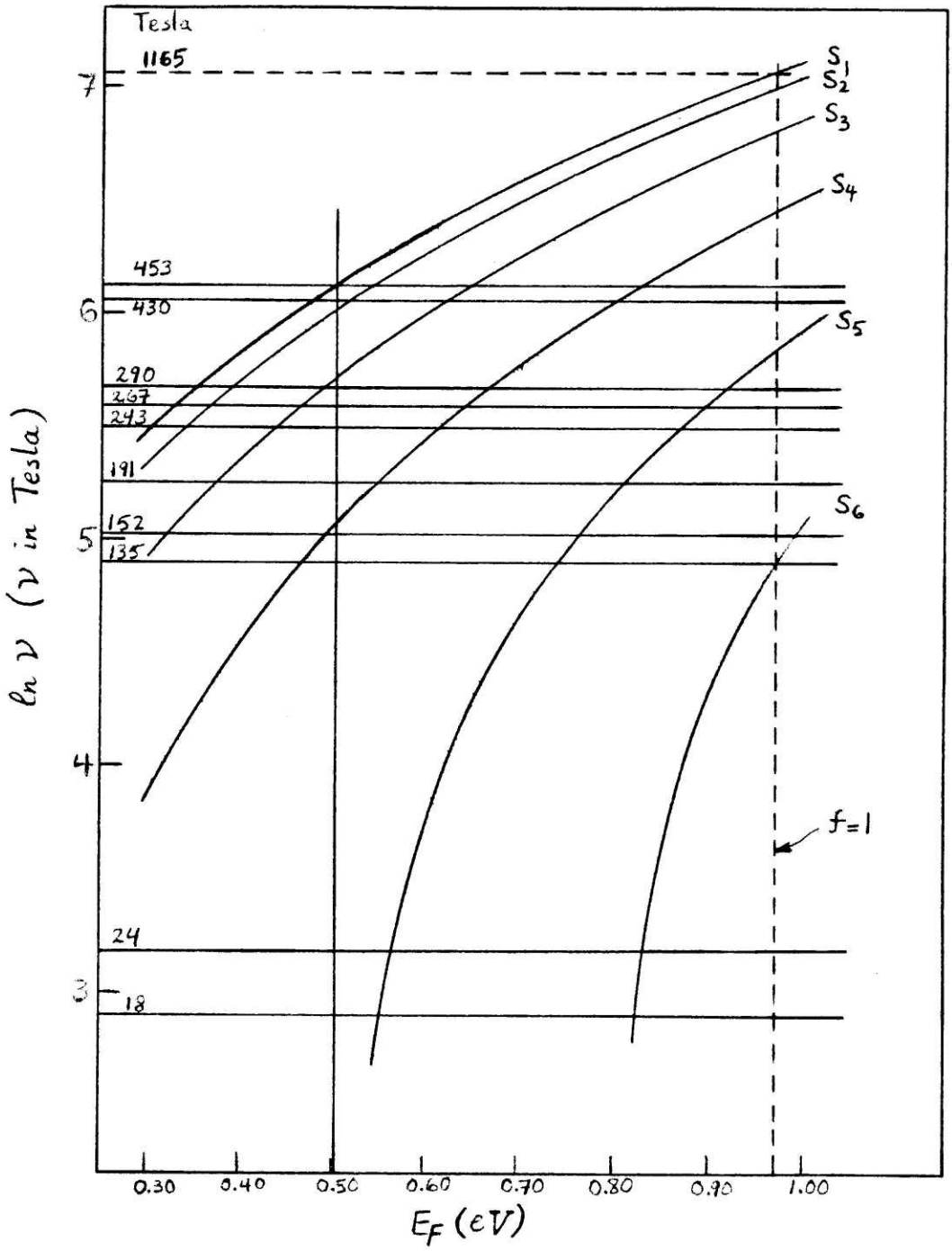


Figure 6.1

Plot of $\ell n\nu$ vs $E_F$ ( $\nu$ is the FS cross section in T) for different cross sections (cuts) of the Fermi surface for a stage-5 compound. Different cuts are labeled by $S_i$. Horizontal lines denote the observed SdH frequencies for a K-stage-5 compound. The vertical line at $E_F$ = 0.505eV is the Fermi level of this K-stage-5 compound determined by matching the largest observed frequency (453T) to the largest predicted frequency (from the cut at $S_1$). The dashed line at $E_F$ = 0.970eV corresponds to an f-value of unity (see text).

note that the two largest frequencies ( $\sim$ 1200T) seen in the dubious stage-5 sample (KTEMP.A) agree very well with the predicted 1165T frequency. This puzzling feature needs clarification and some comments aimed at resolving this point will be made later in this chapter. One final point to note is that the (cyclotron) effective mass at $E_F$ defined by

$$\frac{m^*}{m_o} = \frac{\hbar^2}{2\pi m_o} \left.\frac{\partial A}{\partial E}\right|_{E_F} \tag{6.4}$$

can be easily found from the slopes of the $S_i$ curves in Fig. 6.1. The effective masses predicted by this model are calculated using Eq. 6.4 and are tabulated in Table 6.4.Their discussion and comparison to observed values will be presented at the end of this section.

Next we use the general phenomenological $E(\vec{k})$ model [22] as discussed in section 2.4.2 to interpret the observed SdH frequencies. This model will be referred to as model II. A computer program written by G. Dresselhaus and S. Leung [40] was used to set up and diagonalize the Hamiltonian (Eqs. 2.21 and 2.22) at many $\vec{k}$-vector values near the edge of the BZ. Plots of the eigenvalues as a function of $\vec{k}$ (such as Fig. 2.9) were made. The Fourier expansion parameters used in this model were derived from the band parameters of Table 2.1 and trigonal warping of the Fermi surface was included ($\gamma_3$ = 0.315eV [40]). Because of including the trigonal warping of the constnat energy surfaces (see Fig. 6.2), $E(\vec{k})$ was different as we go from K to $\Gamma$ as compared with K to M. A plot of $E(\vec{k})$ for a stage-5 compound with a "vacuum" intercalate layer (see section 2.4.2.) is shown in Fig. 6.3. The position of $E_F$ is determined empirically so that the FS cross sections of the four partially occupied

* Here $E_F$ is measured relative to the point of high degeneracy at the K-point (see Fig. 6.3).

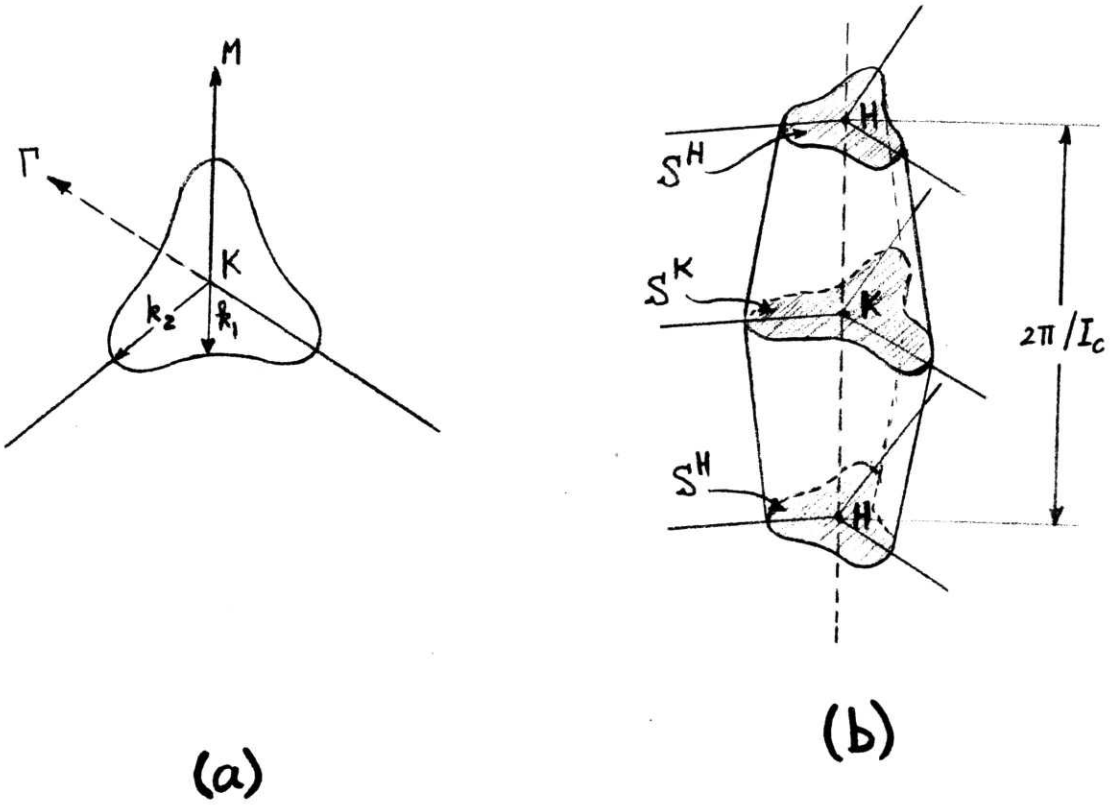


Figure 6.2

Schematic figures showing the trigonally warped Fermi surface (b) and its cross section (a).

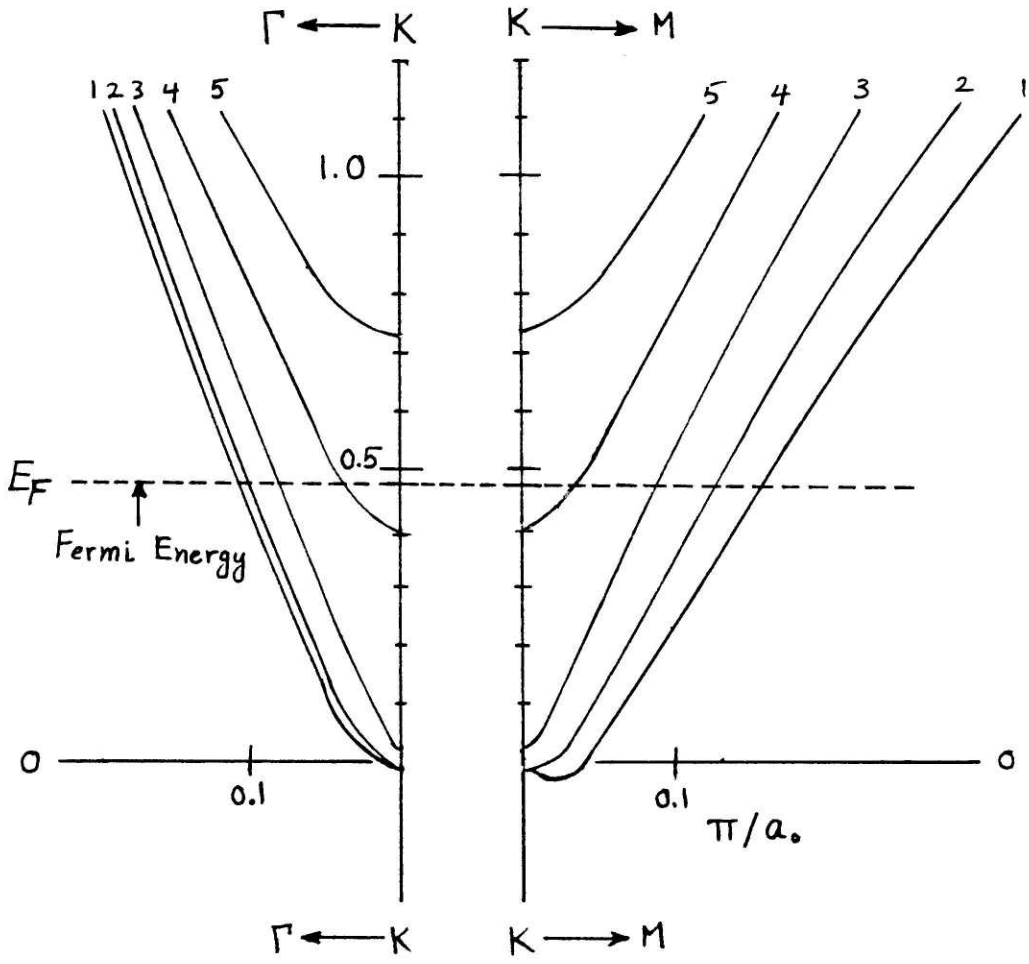


Figure 6.3

$E(\vec{k})$ for a stage-5 compound according to Model II. Only the upper (partially occupied) bands are drawn. To emphasize the presence of trigonal warping, k is swept away from the K-point toward the Γ and M points. The position of the Fermilevel $E_F$ is chosen to fit the experimental data (the origin of energy scale is chosen for lowest-lying conduction band at K-point).

conduction bands give the best fit to the experimental data. $E_F$ is chosen here to be equal to 0.475eV and the calculated cross-sectional areas (or, equivalently, the SdH frequencies) at the K and H points are given in Table 6.3 for the four electron pockets. The area of the FS cross sections is approximated by

$$S = \pi k_1 k_2 \tag{6.5}$$

where $k_1$ and $k_2$ are shown in Fig. 6.2. It has been shown that the area given by Eq. 6.5 approximates the actual area of the warped surface of graphite very well [37]. Note that in Table 6.3 the ratio $k_1/k_2$ indicates that trigonal warping is more significant for the larger cross-sectional areas than for the samaller ones.

We can also find the electron density for each pocket by assuming that the FS has the shape of a trigonally warped cone with the head cut off [Fig. 6.2(b)]. The volume of the carrier pocket j is then given by:

$$V_j = \frac{1}{3}\left(S_j^K + S_j^H + \sqrt{S_j^K S_j^H}\right)\frac{2\pi}{I_c} \cong \frac{1}{2}\left(S_j^K + S_j^H\right)\frac{2\pi}{I_c} \tag{6.6}$$

where the approximation is valid for the cases in which $S_j^K \cong S_j^H$ (nearly cylindrical FS). Since each hexagonal zone contains two full carrier pockets, then $n_j$, the carrier density for band j, is given by:

$$n_j = (2)(2)\,[V_j/(2\pi)^3] = 2\left(S_j^K + S_j^H\right)\frac{1}{(2\pi)^2 I_c} \tag{6.7}$$

where a factor of 2 has been included for spin degeneracy. The total number of carriers is obtained by summing $n_j$'s for the four occupied pockets, yielding $n = 4.60 \times 10^{20}\,cm^{-3}$ and thus a fractional charge transfer of $f = 0.24$ is obtained, which is in fair agreement with the value predicted by model I (0.30).

| Band Index | $K_1$ | $H_1$ | $K_2$ | $H_2$ | $K_3$ | $H_3$ | $K_4$ | $H_4$ |
|---|---|---|---|---|---|---|---|---|
| Trigonal Warping ($k_1/k_2$) | 0.68 | 0.68 | 0.77 | 0.78 | 0.91 | 0.91 | 1.00 | 1.00 |
| Electron Density for Pocket ($cm^{-3}$) | $2.07 \times 10^{20}$ | | $1.55 \times 10^{20}$ | | $0.854 \times 10^{20}$ | | $0.121 \times 10^{20}$ | |
| Calculated SdH Frequency (T) | 401 | 401 | 300 | 299 | 163 | 168 | 26.7 | 20.2 |
| Observed SdH Frequency (T) | 453; 430 | | 290; 267; 243 | | 191; 152; 135 | | 24 ; 18 | |

Table 6.3

Fermi surface parameters associated with K-stage-5 graphite-potassium as calculated by Model II.

As in Table 6.1, the observed SdH frequencies are grouped to show their relevance to the calculated values. We note the very good agreement between the experimental and theoretical data. Because of the small dispersion of the bands along the KH axis, the K and H point cross sections have nearly equal areas. In order to make a better fit to the observed data modifications to the bands, such as the introduction of intercalate-graphite and intercalate-intercalate interactions , is necessary to yield such dispersion along the KH axis.

Once again we can draw curves analogous to Fig. 6.1 showing the dependence of the SdH frequencies on $E_F$. In Fig. 6.4, such curves are shown for the bands 1-5 (Fig. 6.3) for the K-point cross sections. We immediately note the striking, but indeed expected, similarity between the cross section curves $S_2$ - $S_6$ in Fig. 6.1 and 1-5 in Fig. 6.4. This similarity is expected because, as discussed in section 2.4, both models I and II are based on graphite $\pi$-bands and c-axis zone-folding. In fact, it is true that model I is a special case of model II, the correspondence here being that, instead of replacing every sixth layer (for stage 5) of graphite with an intercalate layer (here in Figs. 6.3 and 6.4 actually with "vacuum"), we have replaced it back with a graphite layer! There is, however, the additional $S_1$ curve in Fig. 6.1 This is a amanifestation of the fact that in model II, when we replace the intercalate layer by "vacuum", we effectively make the intercalate level disappear from the $E(\vec{k})$ picture by taking its energy to be $-\infty$ . Doing this prevents this level from interacting with the other levels.

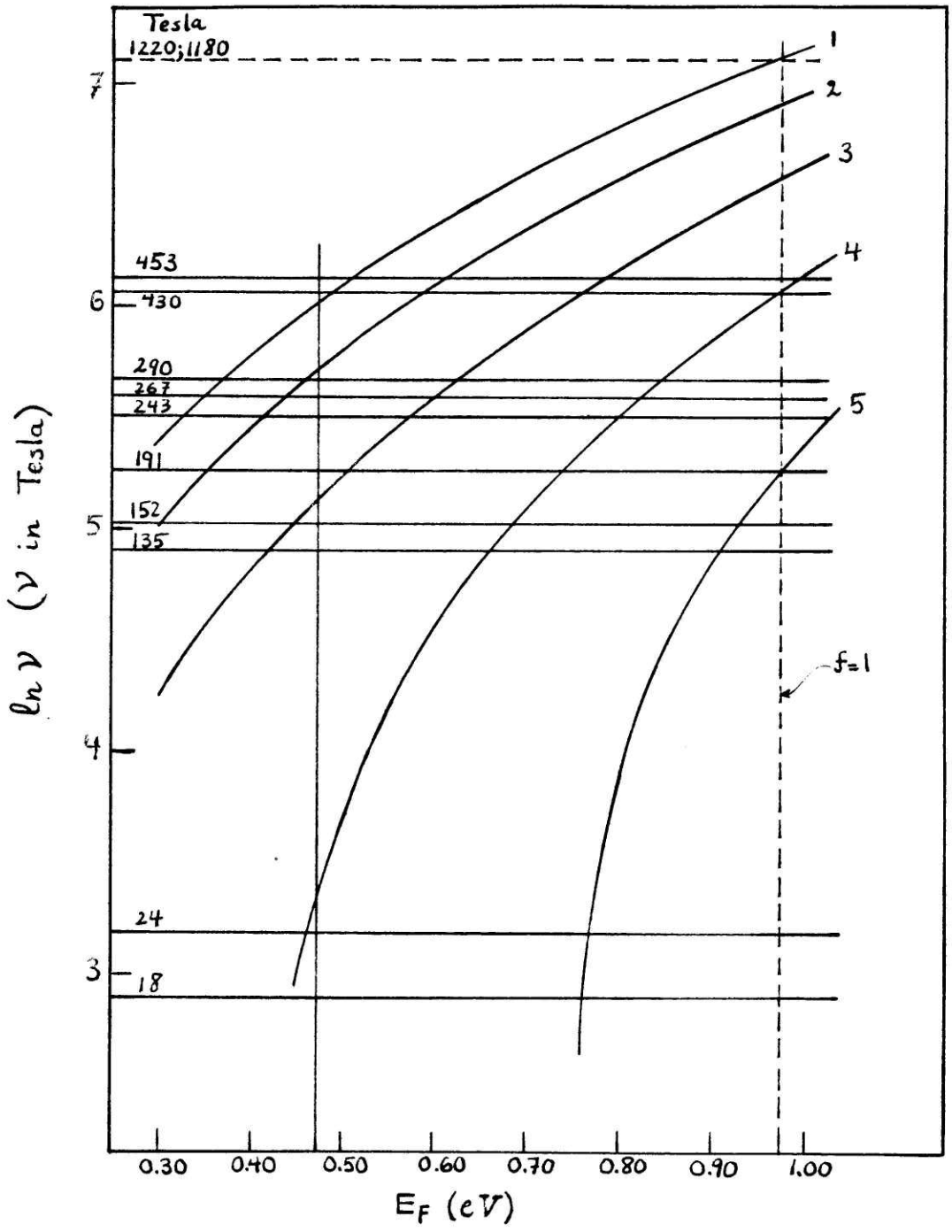


Figure 6.4

Plot of $\ell n\nu$ vs $E_F$ for the K-point FS cross sections $\nu$ of a stage-5 compound. The energy bands of Fig. 6.3 (Model II) are used to obtain the different branches (1-5). Horizontal lines represent the observed SdH frequencies for a K-stage-5 compound. The vertical line at $E_F$ = 0.475eV is determined to match the observed and predicted frequencies; the dashed line at $E_F$ = 0.975eV corresponds to f = 1.0.

In Fig. 6.4, $E_F$ = 0.475eV is shown by a vertical solid line, and again as in Fig. 6.1, the Fermi level resulting in f = 1 is shown by a dashed line at $E_F$ = 0.975eV. Once again we see that, with $E_F$ = 0.975eV and f = 1, the largest predicted cross section is ∿1224T, a value which is in unexpectedly good agreement with the frequency observed in KTEMP.A! Before commenting on this agreement, let us tabulate the effective masses calculated at the Fermi level predicted by models I and II (using Eq. 6.4) and compare them with the observed values. This is done in Table 6.4. The observed and calculated frequencies ($\nu$) for the K-stage-5 sample (Tables 6.2 and 6.3) and the calculated $m^*/m_0$ are given in Table 6.4. The observed $m^*/m_0$ are those measured for samples KTEMP.A and KTEMP.B, as reported in Table 5.2. The $m^*/m_0$ observed values are written here for the "like" frequencies, i.e., those which are roughly the same as the ones for which was measured (see Table 5.2). The values of $m^*/m_0$ = .079 calculated for the ∿ 24T frequency for model I is written in parentheses for the following reason. Figure 6.1 shows that, with $E_F$ = 0.505eV, there is no predicted frequency of ∿ 24T. But, if we just raise $E_F$ to ∿ 0.560eV, then $S_5$ will give a frequency of ∿24T and from the slope of $S_5$ at the point of interception, we find $m^*/m_0$ = 0.079 as an estimate for the effective mass.

The agreement between the calculated (especially for model II) and the observed $m^*/m_0$ is remarkably good, and clearly shows that the measured effective masses, and thus the bands whose curvature they depend on, are graphitic.* It should also be mentioned that these effective masses are in good agreement with those reported for K [62] and $FeCl_3$ [9] GIC by other authors.

---

* For pristine graphite, $E_F$ = -0.024eV and the electron effective mass at $E_F$ is $m^*/m_0 \cong 0.057$.

| $\nu$ (Tesla) | | | $m^*/m_o$ | | |
|---|---|---|---|---|---|
| Model I | Observed (KO5. Y03) | Model II | Model I | Observed (KTEMP. A,B) | Model II |
| 453 ←→ 453 | | 401 | 0.21 | 0.15 - 0.16 | 0.14 |
| 412 | 430 | | 0.20 | | |
| 304 | 290<br>267<br>243 | 300 | 0.17 | – | 0.12 |
| 157 | 191<br>152<br>135 | 163 | 0.11 | 0.10 - 0.11 | 0.083 |
| – | 24<br>18 | 26.7 | (0.079) | 0.045 | 0.051 |
| 0.505 | $E_F$ (eV) | 0.475 | 0.505 | $E_F$ (eV) | 0.475 |
| 0.30 | f | 0.24 | 0.30 | f | 0.24 |

Table 6.4

Comparison of the calculated and observed SdH frequencies and effective masses for the K-stage-5 compound.

Now let us see what happens if we insist that f = 1 and increase $E_F$ to 0.970eV in Fig. 6.1, and to 0.975eV in Fig. 6.4. In Table 6.5, the resulting SdH frequencies and effective masses are tabulated. Here, the observed values are those seen in sample KTEMP.A. The reader is reminded that, although Table 6.5 is based on the application of models I and II to a stage-5 compound, the nature of KTEMP.A is dubious (see previous remarks about this sample in Chapter V). There is some reasonable agreement between the observed and the calculated frequencies, especially for model II, although the observed ∿22T frequency is not predicted. Note in both Figs. 6.1 and 6.4 that there is not even a band (cross section curve) that would give a small cross section (~ 22T) if we change $E_F$ by a small amount. Also, both models predict frequencies of approximately 600 to 900T which are not observed experimentally.

In comparing the effective masses, we note an excellent agreement between the observed and calculated (again for model II) $m^*/m_o$ for the ~ 1200T freauency. Such an agreement is an indication that this cross section and the $m^*/m_o$ associated with it (0.36) are graphitic. This agreement is very curious and one may be tempted to regard the ~1200T frequency as the correct largest frequency observed in a K-stage-5 compound. Although such a possibility cannot be entirely eliminated, we will see in the following discussion that this is highly unlikely.

As a first, but not most convincing argument, note that the agreement between the calculated and the observed $m^*/m_o$ is better in Table 6.4 than in Table 6.5 (excluding the 0.36 effective mass). In Table 6.5 the calculated masses are too large, compared with the observed values. Both Figs. 6.1 and 6.4 show that lower $E_F$ values result in lower effective masses, and thus it can be concluded, although not conclusively,

| $\nu$ (Tesla) | | |
|---|---|---|
| Model I | Observed (KTEMP.A) | Model II |
| 1164 | 1220 | 1224 |
| 1086 | 1180 | 1002 |
| 903 | — | 715 |
| 626 | | |
| | 430 | 428 |
| 344 | 414 | |
| | 230 | |
| | 204 | |
| | 182 | 185 |
| 133 | | |
| — | 22 | — |
| 0.970 | $E_F$ (eV) | 0.975 |
| 1.0 | $f$ | 1.0 |

| $m^*/m_o$ | | |
|---|---|---|
| Model I | Observed (KTEMP.A) | Model II |
| 0.31 | 0.36 | 0.36 |
| 0.31 | | 0.36 |
| 0.29 | — | 0.26 |
| 0.24 | | |
| | 0.16 | 0.21 |
| 0.19 | | |
| | 0.13 | |
| | 0.15 | |
| | 0.11 | 0.18 |
| 0.17 | | |
| - | 0.045 | - |
| 0.970 | $E_F$ (eV) | 0.975 |
| 1.0 | $f$ | 1.0 |

Table 6.5

Comparison of the calculated and observed SdH frequencies and effective masses for KTEMP.A. In using the models it is assumed that the compound is stage-5 and that f = 1.0.

that an $E_F$ value of approximately 0.975eV is rather too large (the predicted effective masses are too large).

Secondly, if we do take the ~ 1200T frequency as the largest cross section, then $f \cong 1$ and since the value of f is not expected to change by much as we go from stage n to stage n+1, then the largest cross section for a K-stage-4 compound must also be fairly large (> 1200T, as we shall see shortly). But such a frequency has been observed neither by Tanuma et al [5] nor by us (Table 5.3). In fact, as the analysis of the next section will show if we assume an f value of about unity for the other compounds then we should expect much larger frequencies than those observed in the samples (except the stage-8 samples). Now it is true that in the SdH experiment it is generally difficult to observe high-frequency (large cross section) oscillations because of their small $\tau_c/m^*$ (see sections 2.5 and 4.2). However, if we can see a 1220T frequency in a maltreated (no encapsulation) sample, there is no reason why we should not see frequencies of this magnitude in other samples which were handled better.

The large frequencies observed in K and Rb stage-8 compounds (see Table 5.3) also support the view that these large frequencies cannot correspond to the largest FS cross sections of a single-stage-8 compound! This point will be made clear in the next section, where all the studied samples will be analyzed.

## VI-3. Results of Analysis of SdH Data for Potassium and Rubidium Compounds

The analyses of the last section can be applied to the other compounds (K-stages 4,8, and Rb-stages 2,3,5,8) in a similar way. In analyzing the rubidium compounds, we use the experimentally determined in-plane density $\chi$ = 14.0 [61]. The chemical formula for a stage n compound is thus $C_{14n}Rb$.

We first consider Rb-stage-8 compound (Table 5.3). In applying model I if we use the ∿1220T as the largest FS cross section, we find that $n = 2.06 \times 10^{21}\ cm^{-3}$. Using Eq. 6.3 with $I_c = 29.10\text{Å}$ (see Chapter III and $\chi = 14.0$, we also find $n' = 9.37 \times 10^{20} cm^{-3}$, meaning that f = 2.20* -- a very unpleasant situation! An f value of larger than unity is not physically possible: we cannot have more electrons in the sample than those available (from the intercalate layer). We have the same situation for the K-stage-8 sample. Application of model I to this sample, with $\nu_{max}$ = 1060T as the largest FS cross section, results in an f value equal to 1.43**, again too large a value to be acceptable.

An important observation can be made if we consider the close relation between the large frequency (∿ 1200T) peaks in sample KTEMP.A (Fig. 5.6) and Rb-stage-8 (Fig. 6.5). The fact that we have doublets at almost exactly the same positions for two K and Rb samples of different stages is very likely the evidence that these peaks come from certain graphitic regions of the sample - which evidently have a large electron concentration. These regions are graphitic because we see them in both potassium and rubidium compounds, and also because the effective mass associated with their FS cross section (Table 6.5) is graphtic, as opposed to metallic, i.e., $m^*/m_o \cong 1$. One can imagine islands of graphite surrounded by a high concentration of the alkali-metal. As a matter of fact, the electron microscope studies have shown that such islands (or clusters) of both graphite graphite or alkali metal do exist in the graphite intercalation

---

* Application of model II to a stage-8 compound ($\chi = 14.0$) with $\nu_{max}$ = 1220T results in f ≅ 1.91.

** Application of model II to a stage-8 compound ($\chi = 10.5$) with $\nu_{max}$ = 1122T results in f ≅ 1.35.

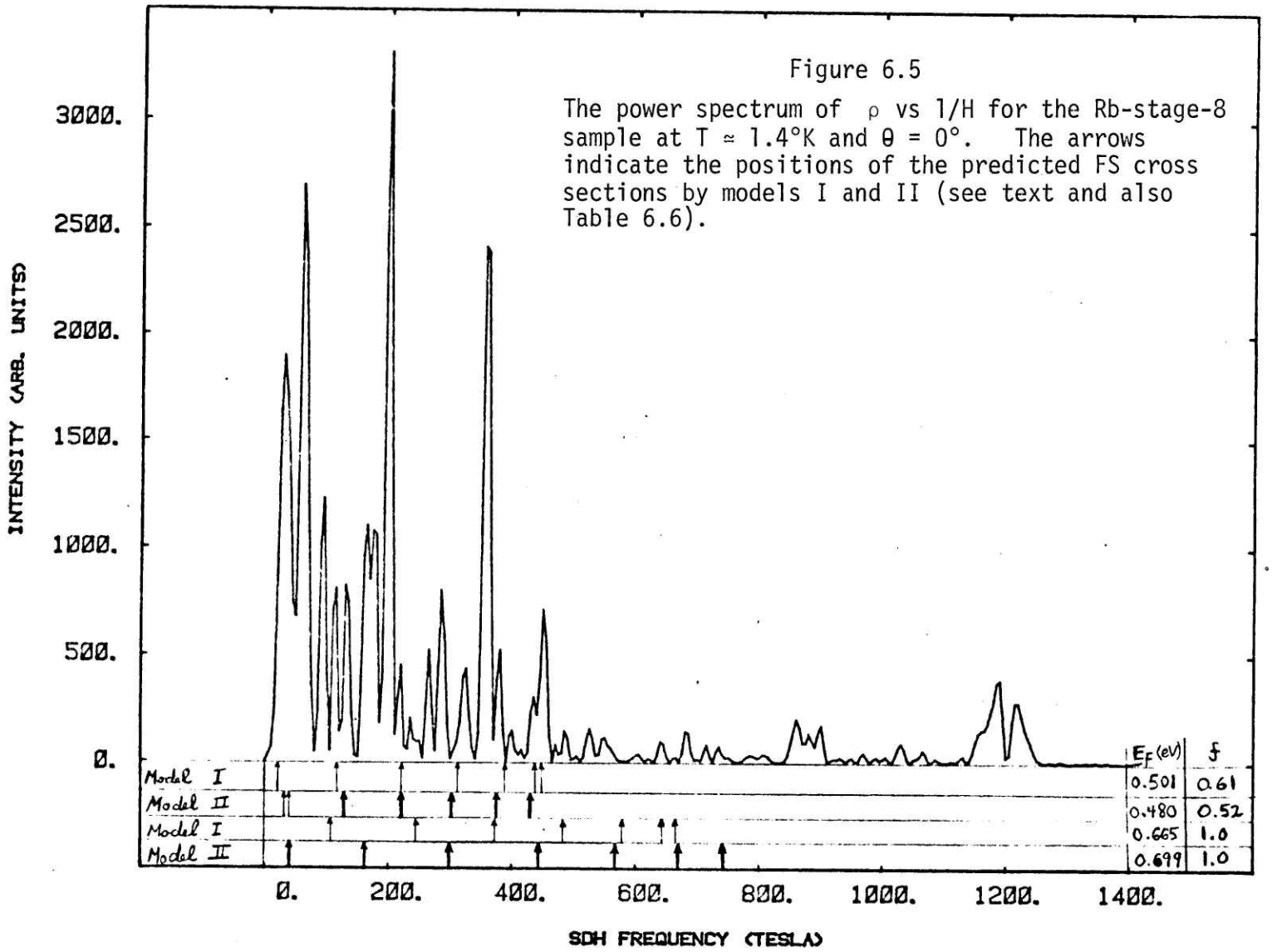


Figure 6.5

The power spectrum of $\rho$ vs 1/H for the Rb-stage-8 sample at T ≃ 1.4°K and θ = 0°. The arrows indicate the positions of the predicted FS cross sections by models I and II (see text and also Table 6.6).

| SdH Frequency (T) | | | | |
|---|---|---|---|---|
| $\nu_{calculated}$ (Model I) | | $\nu_{observed}$ | $\nu_{calculated}$ (Model II) | |
| | | 1220 | | |
| | | 1190 | | |
| 665 | | 900 | | 736 (2) |
| 644 | | | | 663 (2) |
| 581 | | 860 | | 561 (2) |
| 486 | | | | |
| | 450 | 450 | 428 (2) | 437 (2) |
| | 432 | | | |
| | 383 | 380 | 373 (2) | |
| 369 | | 355 | | |
| | | 325 | | |
| | 309 | | 300 (2) | 293 (2) |
| | | 285 | | |
| | | 265 | | |
| 238 | | | | |
| | 219 | 220 | 219 (2) | |
| | | 200 | | |
| | | 175 | | |
| | | 165 | | 157 (2) |
| | | 130 | 124 (2) | |
| 106 | 119 | 115 | | |
| | | 95 | | |
| | | 60 | | |
| | | 30 | 29 (2) | 38 (2) |
| | 17 | | | |
| 0.665 | 0.501 | $E_F$ (eV) | 0.480 | 0.699 |
| 1.0 | 0.61 | f | 0.52 | 1.0 |
| (b) | (a) | | (a) | (b) |

Table 6.6

The observed and calculated SdH frequencies $\nu$ for the Rb-stage-8 compound for two cases:

a) Considering $\nu_{obs.}$ = 450T to be the largest FS cross section (see text)

b) Assuming f = 1.0.

The frequencies with the largest Fourier intensity are underlined.

compounds [63,64]. We may even estimate the minimum size of such graphite islands from the field-dependence of the SdH oscillations. The critical (minimum) radius $R_c$ for such domains should be at least as large as the radius of classical circular motion ($r_c$) of an electron with Fermi energy, so that the electron can cover complete orbits. Thus, we must have:

$$R_c > r_c = \frac{v_F}{\omega_o} = \frac{\hbar k_F}{m\omega_o}\left(\frac{\hbar c}{eH_c}\right)k_F = \left(\frac{\hbar c}{eH_c}\right)\left(\frac{A_F}{\pi}\right)^{1/2} = \frac{\hbar c}{eH_c}\left(\frac{\nu_F 2\pi e}{\hbar c \pi}\right)^{1/2}$$

$$= \frac{1}{H_c}\left(\frac{2\hbar c \nu_F}{e}\right)^{1/2} \qquad (6.8)$$

where $v_F$ is the Fermi velocity, $\omega_o = eH/mc$ is the cyclotron frequency, $A_F$ is the FS cross section, $\nu_F$ is the SdH frequency (see Eq. 2.31 for the relation between $A_F$ and $\nu_F$ ), and $H_c$ is the lowest (critical) field value at which quantum oscillations can be observed.

Using $\nu_F$ = 1200T and $H_c$ = 8T [$\sim$ the lowest field in Fig. 5.8(c) at which the oscillations at $\sim$1200T can be observed], we find $r_c \cong 0.15\,\mu m$, a value which is of the right order of magnitude when compared to the island sizes observed in the electron microscopy studies [64,64,65].

Now, let us return to the Rb-stage-8 sample. Excluding the $\sim$1200T frequencies, we do not know what to use as the largest FS cross section. We may, however, work backward and arbitrarily choose f = 1.0 and calculate the predicted frequencies. The results are shown in Fig. 6.5 and Table 6.6 for model I and model II. The arrows in Fig. 6.5 show the positions of the predicted frequencies. For model II, only the K-point cross sections are shown, while the H-point cross sections are very close to those at the K point. Thick arrows in Fig. 6.5 indicate that actually

two nearly equal cross sections are predicted (this is because of the near-degeneracy of bands for even-stage compounds; see section 2.4.2). The numbers in parentheses in Table 6.5 also indicate the degeneracy of the predicted K-point cross sections.

Well, from Fig. 6.5 we note that there is not much of an agreement between the calculated and observed frequencies when f = 1.0. Besides, in view of the results for K-stage-5 sample ($f \cong 0.3$), and also the small f values for the other compounds, as we shall see later, the f value is likely to be smaller than unity. Thus, let us choose the largest (dominant) frequency of ~450T in Fig. 6.5 and apply our models. Results are shown in Fig. 6.5, again by arrows, and Table 6.6. We note that, although there is not a one-to-one correspondence between the observed and predicted cross sections, the numerous and closely spaced frequencies observed are compatible with the many frequencies predicted. This is especially the case for mode II, if we recall that by introducing proper interaction, we can lift some of the degeneracies and have up to a total of 24 (for K- and H-point) cross sections.

In a similar fashion we may try to analyze the K-stage-8 compound in two ways: with f = 1 and with $\nu_{max} \approx 400$T. The latter results in an f value of $\sim 0.40$ (model I) or $\sim 0.35$ (model II), in reasonable agreement with the results for K-stage-5; the results are summarized in Table 6.7.

It is worthwhile mentioning here that compounds of high stage index are complicated, both structurally and electronically. Besides, it is hard to grow single-stage samples with n larger than 5. The high-stage samples usually contain mixtures of stage $n \pm 1$ with them. The energy band structure as well as the FS for these compounds, is also complicated.

| SdH Frequency (T) | | | | |
|---|---|---|---|---|
| $\nu_{calculated}$ (Model I) | | $\nu_{observed}$ | $\nu_{calculated}$ (Model II) | |
| | | 1060 | | |
| | | 1015 | | 944 (2) |
| 842 | | 865 | | 865 (2) |
| 817 | | 825 | | 728 (2) |
| 744 | | 700 | | 582 (2) |
| 632 | | 660 | | 415 (2) |
| 494 | 400 | 400 | 397 (2) | |
| | 383 | 380 | | |
| 39 | 337 | 280 | 344 (2) | |
| | 267 | 240 | 268 (2) | 253 (2) |
| | | 210 | | |
| 185 | 183 | 190 | 197 (2) | |
| | 90 | 105 | 104 (2) | 117 (2) |
| | | 60 | | |
| 53 | | 45 | 20 (2) | 14 (2) |
| | | 20 | | |
| 0.782 | 0.459 | $E_F$ (eV) | 0.450 | 0.820 |
| 1.0 | 0.40 | f | 0.35 | 1.0 |
| (b) | (a) | | (a) | (b) |

Table 6.7

The observed and calculated SdH frequencies $\nu$ for the K-stage-8 compound for two cases:

a) Considering $\nu_{obs.}$ = 400T to be the largest FS cross section, and

b) Assuming f = 1.0.

The frequencies with the largest Fourier intensity are underlined.

This is evident from the energy bands shown in Fig. 2.10 for a stage-8 compound, the validity of which is supported by the quite complicated SdH spectrum of Fig. 6.5. The conclusion to make from the analyses of stage-8 compounds (Tables 6.6, 6.7), thus, is to note the good "qualitative" correlation between the experimental and theoretical results. No "quantitative" conclusions should be drawn at this point. The situation is not so desperate for lower-stage compounds. In what follows, we will see that, since both the experimental spectra and the models are simpler for lower-stage compounds, we can draw some quantitative conclusions, as we did for K-stage-5 sample.

In Tables 6.8 - 6.11, we have listed the results for the rest of the samples that were studied. Although here the largest observed frequency ($\nu_{max}^{obs}$) is well defined, we have also included the calculated frequencies assuming f = 1 for each compound (Tables 6.8-6.10). This has been done, firstly for completeness, and secondly to show that, with f = 1 the predicted frequencies are quite large and that almost none of the observed frequencies can be explained.

On the other hand, using $\nu_{max}^{obs.}$ to match $\nu_{max}^{calc.}$ we have very good agreement between observed and predicted frequencies. The agreement for Rb-stage-5, especially model II with $E_F$ = 0.475eV, is excellent (Table 6.9). We also note the very good correlation between experimental and theoretical results in K-stage-4 (Table 6.8). This table should be compared to Table 6.1(a), which shows Tanuma's analysis, mode I, for the same compound (K-stage-4).

For sample Rb-stage-2 (Table 6.11), once again the agreement between $\nu_{obs.}$ and $\nu_{calc.}$ is remarkable for model II with $E_F$ = 0.420eV. However,

| SdH Frequency (T) | | | | |
|---|---|---|---|---|
| $\nu_{calculated}$ (Model I) | | $\nu_{observed}$ | $\nu_{calculated}$ (Model II) | |
| 1337<br>1226<br>932<br>551 | | | | 1495 (2)<br>1137 (2)<br>732 (2) |
| | | | 385 (2) | 378 (2) |
| | 354 | 354 | | |
| | 300 | | | |
| | | 276 | | |
| | | 264 | 260 (1) | |
| | | | 246 (1) | |
| 241 | | | | |
| | 176 | | | |
| | | 150 | | |
| | | 132 | | |
| | | | 89 (1) | |
| | | | 76 (1) | |
| 1.06 | 0.420 | $E_F$ (eV) | 0.480 | 1.12 |
| 1.0 | 0.19 | $f$ | 0.19 | 1.0 |
| (b) | (a) | | (a) | (b) |

Table 6.8

The observed and calculated SdH frequencies $\nu$ for the K-stage-4 compound for two cases:

a) Considering $\nu_{obs.}$ = 354T to be the largest FS cross section, and

b) Assuming f = 1.0.

| SdH Frequency (T) | | | | |
|---|---|---|---|---|
| $\nu_{calculated}$ (Model I) | | $\nu_{observed}$ | $\nu_{calculated}$ (Model II) | |
| 928 | | | | 1013 |
| 868 | | | | 807 |
| 703 | | | | |
| | | | | 562 |
| | 420 | 420 | 401 | |
| | 382 | | | |
| | 280 | 294 | 300 | 310 |
| 224 | | | | |
| | 144 | 148 | 163 | |
| | | | | 101 |
| 35 | - | 24 | 27 | |
| 0.835 | 0.476 | $E_F$ (eV) | 0.475 | 0.870 |
| 1.0 | 0.37 | f | 0.32 | 1.0 |
| (b) | (a) | | (a) | (b) |

Table 6.9

The observed and calculated SdH frequencies $\nu$ for the Rb-stage-5 compound for two cases:

a) Considering $\nu_{obs.}$ = 420T to be the largest FS cross section, and

b) Assuming f = 1.0.

| SdH Frequency (T) | | | | |
|---|---|---|---|---|
| $\nu_{calculated}$ (Model I) | | $\nu_{observed}$ | $\nu_{calculated}$ (Model II) | |
| 1221 | | | | 1330 |
| 1060 | | | | 1215 |
| 660 | | | | |
| | 405 | 405 | 405 | |
| | 319 | | | |
| 238 | | 260 | | 272 |
| | | 170 | 222 | |
| | 124 | | | |
| | | 35 | | |
| 1.00 | 0.463 | $E_F$ (eV) | 0.500 | 1.17 |
| 1.0 | 0.23 | f | 0.22 | 1.0 |
| (b) | (a) | | (a) | (b) |

Table 6.10

The observed and calculated SdH frequencies for the Rb-stage-3 compound for two cases:

a) Considering $\nu_{obs.}$ = 405T as the largest FS cross section, and

b) Assuming f = 1.0.

| SdH Frequency (T) | | | | | | |
|---|---|---|---|---|---|---|
| $\nu_{calculated}$ (Model I) | | | $\nu_{observed}$ | $\nu_{calculated}$ (Model II) | | |
| | | | | | | 1820 (2) |
| 1627 | | | | | | |
| 1286 | | | | | 691 (2) | 937 (2) |
| 579 | | | | | | |
| | 401 | | | | | |
| | 252 | 255 | 255 | 255 (1) | 253 (1) | |
| | | | 213 | 230 (1) | 229 (1) | |
| | | 145 | | | | |
| | | - | 28 | 19 (1) | | |
| 1.20 | 0.460 | 0.320 | $E_F$(eV) | 0.420 | 0.800 | 1.30 |
| 1.0 | 0.17 | 0.07 | f | 0.07 | 0.33 | 1.0 |
| (c) | (b) | (a) | | (a) | (b) | (c) |

Table 6.11

The observed and calculated SdH frequencies $\nu$ for the Rb-stage-2 compound for three cases:

a) Considering $\nu_{obs.}$ = 255T to be the largest FS cross section,

b) Assuming $\nu_{obs.}$ = 255T to be the second largest cross section, and

c) Assuming f = 1.0.

as a result of the small value of $\nu_{max}^{obs.}$ = 255T, and thus the small value of $E_F$, the f value is very small (0.07). So, despite the fine agreement for the frequencies, we may wish to raise $E_F$ and attempt to match the second largest predicted frequency, with $\nu^{obs.}$ = 255T and see what f value results. The outcome of such an attempt is given in Table 6.1? for model II, with $E_F$ = 0.460eV, f = 0.17, and for model II ($E_F$ = 0.800eV and f = 0.33 ). Note that in this case, model II fails to predict the very dominant 19T frequency -- see Fig. 5.15(a). The same is true for model I, with $E_F$ = 0.460eV, Table 6.1?. The conclusion, then, is that although f = 0.07 is very small, it does correspond to the best fit of the experimental data with the theoretical models. Once again, it must be emphasized that small values of f result from the assumption that all the carrier pockets present in the zone are probed by the SdH experiments. In reality, there may exist other carrier pockets, possibly elsewhere in the zone (away from the KHaxis) whose cross sections are not observed in our experiment (because of their large $m^*/m_o$ or small scattering time $\tau_c$). Such carrier pockets would contribute to increase the above f values.

In closing this section, it must be mentioned that, when we consider the observed frequencies for all the compounds (Table 5.3), we note that there are certain frequencies which are common to two different -- but usually close -- stages of a given intercalate (e.g., the 150T frequency for potassium compounds with n = 4,5). It must be admitted that models I and II, which are based on the stage-dependence of the electronic structure, do not explain this observation explicitly. However, with adjusting $E_F$ and even assuming some functional dependence of f on stage

(see next section), similar frequencies for compounds of two different stages can be obtained. This has been done, in an implicit way, in the above analyses.

## IV-4. Summary and Conclusions

Most of the conclusions and comments stated here in this section concern the experimental results and the application of the theoretical models for their interpretation. However, there is one other very important conclusion about the experimental work (physical measurements) that must be emphasized -- and that is the absolute necessity of encapsulation, i.e., protection from exposure to air and moisture, when working with the alkali-metal GIC. Samples which are not encapsulated (especially for $n \leq 4$) rarely give stable SdH signals, and even when they do, their results should be interpreted very carefully.

We will enumerate several general conclusions about the analyses of the previous sections:

1. Our analyses of the experimental data have verified that the electronic structure of these (alkali-metal) intercalation compounds is closely related to that of the host graphite. The overall good agreement between the experimental FS cross sections and those calculated by the models (which are closely based on graphite $\pi$-bands) provides evidence for this relation. Also, the effective masses observed in these compounds are in excellent agreement with the calculated values. The graphitic nature of these masses also strongly supports the above views.

2. The observed SdH frequencies are stage-dependent. Although there are certain frequencies which are common between two compounds of different stage (with their stage usually differing by one), our results show that the frequencies are stage-dependent and that they can be interpreted by stage-dependent models. This stage-dependence is compatible with the reported results for other potassium compounds [5-7]. There is also good agreement between our results for the K-stage-4 compound and Tanuma's results for the same compound [5-7].
3. In comparing the observed and calculated FS cross sections, we note that for the high stage compounds (n = 8), there is fairly good qualitative agreement. Because of the complicated shape of the Fermi surfaces due to the multitude of the energy levels for these high-stage compounds, it is difficult to get good quantitative agreement between the experimental and calculated cross sections. In the case of the lower-stage compounds ($n \leq 5$), good quantitative agreement is obtained.
4. The f values are small for all the compounds that were studied (the stage dependence of f will be discussed shortly). As mentioned before, such small values of f result from making the assumption that our SdH measurements probed all the carrier pockets present in the zone; however, there may well exist other pockets, possibly away from the KH axis, which were not observed in our experiments (which require large $\omega_o \tau_\ell$ ). If such pockets are taken into account, then f may have a larger value . The band models, as used, do not predict any other carrier pockets except those near the KH axis; however, with proper

modification, model II can predict such pockets.

When we consider the f values for different stage compounds (except stage 8) of each system, K or Rb, we note that f tends to be larger for compounds of higher stage. This may sound unreasonable at first sight. However, recall that f is a measure of the fractional charge transfer from the intercalate to the graphite layers. In other words, f is an indication of how fully the (donor) intercalant, K or Rb, is ionized (f = 1.0 corresponds to complete ionization). Taking this view, it is not surprising that the more dilue (higher stage) the compound, the more complete is the ionization (larger f). The intercalant, here a donor "donates" more electrons when immersed in a sea of "takers" -- graphite layers! The fact that f is larger for the higher stage compounds has also been reported, although not emphasized, by Iye et al [11] for the graphite-$AsF_5$ system. They report f values of 0.22, 0.26, and 0.28 for graphite-$AsF_5$ compounds of stages 3, 4 and a dilute compound [11].

In studying the GIC to see the general dependence of some physical parameter on stage (for a given intercalant), it is customary to plot the parameter as a function of reciprocal stage (1/n). In our case, we have plotted in Fig. 6.6 the f values calculated by model II as a function of 1/n for K (n = 4,5) and Rb (n = 2,3,5) compounds. The straight lines drawn through the points for each system show the decreasing trend of f with decreasing stage index n. For both the K and Rb systems, we note that the stage-8 f values fall above these lines, although for the K-stage-8 compound, f = 0.35 (Table 6.7), lies failrly close to the value expected from the straight line for K. This discrepancy can hardly be disheartening in view of the fact that the results of the analyses for stage-8

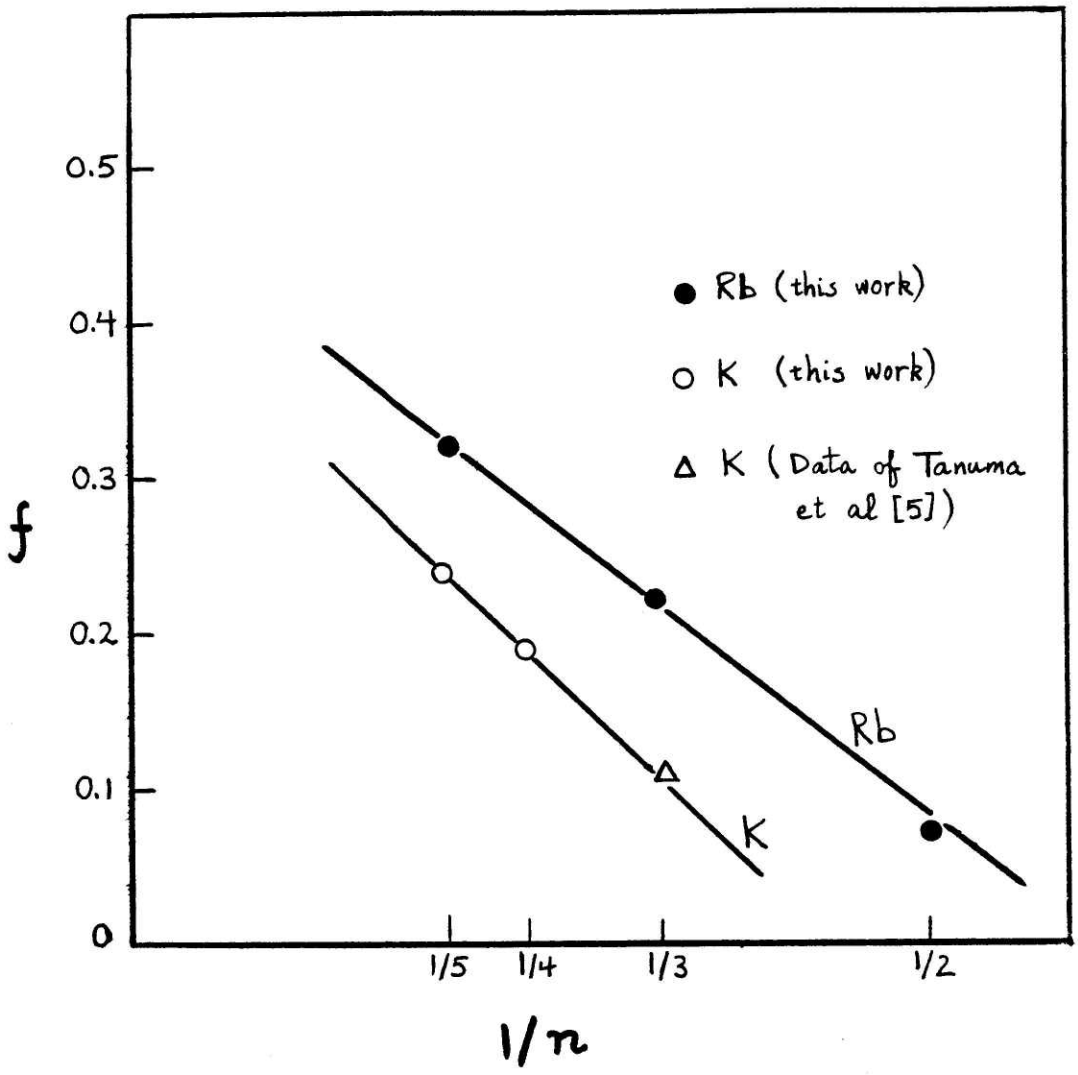


Figure 6.6

Plot of the fractional charge transfer f (as calculated by model II) vs 1/n (n = stage) for K(n = 3,4,5) and Rb(n = 2,3 5) - GIC. The straight lines are drawn through the points for each intercalate system.

compounds should be considered to be only qualitative (see previous sections).

In Fig. 6.6, there is one extra point (Δ) for a K-stage-3 compound which lies right on the line for the K-system. Tanuma et al [5] have reported two SdH frequencies (262T and 194T) for a K-stage-3 compound. Table 6.12 lists the results of the application of model I and model II to this compound.* Once again, the agreement between the calculated frequencies, model II, and $\nu_{obs.}$ is very good. We also find that f = 0.11 (model II) is very consistent with the value expected from the line in Fig. 6.6.

It must be emphasized that the lines in Fig. 6.6 should be viewed only as an indication of a qualitative trend (increasing f as n increases). For example, the fact that f = 0.11 for K-stage-3 falls right on the line through n = 4,5 points, the author believes, is only accidental. The best evidence for this argument is that, if we take such lines too seriously and believe in a linear behavior of f vs 1/n for all stages, we will reach the absurd conclusion that f < 0 for a K-stage-2 compound. Also, stage-1 compounds cannot be expected to follow the trends of Fig. 6.6 (because our above models apply only to dilute compounds), and indeed experimental [5] and theoretical work [16] have verified that they do behave differently and that there are pieces of Fermi surface other than those along the HK axis.

---

* We must mention that, in their analysis for this compound, Tanuma et al [5,6] used a higher value for $E_F$ so that the 262T frequency matches the second largest predicted frequency. They did this in order to get better agreement between their calculated and observed frequencies, and also so that the f value (0.17 in their case) be closer to their f-value for K-stage-4 (f = 0.21, see Table 6.1) compound.

| SdH Frequency (T) | | |
|---|---|---|
| $\nu_{calculated}$ (Model I) | $\nu_{observed}$ | $\nu_{calculated}$ (Model II) |
| 262 ←→ | 262 | 262 |
| 147 | 194 | 160 |
| 48 | | |
| 0.328 | $E_F$ (eV) | 0.450 |
| 0.10 | f | 0.11 |

Table 6.12

The observed (Tanuma et al [5]) and calculated SdH frequencies for a K-stage-3 compound.

5. Our final comment concerns the quantitative explanation of the observed frequencies. It has been mentioned before that model II was used here in its simplest form. No parameters besides those of pristine graphite were used (except for the choice of $E_F$ for the SdH data). By introducing proper intercalate-intercalate and intercalate-graphite interactions, model II can be modified to explain the experimental data more quantitatively. As the simplest example of such a modification, consider the introduction of an intercalate-graphite bounding layer interaction via a single parameter $\mu_o$[40,22]. In Fig. 6.7 the "cross section vs $E_F$" curves (similar to Fig. 6.4) for a stage-5 compound are shown if $\mu_o$ = -0.30eV is used. A comparison of Fig. 6.4 and 6.7 shows that the main effect of this new parameter is to shift the positions of the energy bands relative to each other, without changing their curvatures. Also, the bands still remain mainly flat along the HKH axis, so that we do not yet have the needed dispersion (along the $k_z$-direction) to explain the numerous observed frequencies. This example shows that using model II, a detailed explanation of the FS cross sections may be possible, but that more $k_z$-dependent terms are needed. Furthermore, considerable time will be needed to develop such a fit.

## VI-5 Suggestions for Future Study

It is evident from the analyses of the previous sections that to get a more definitive evaluation of the models, one should concentrate on low-stage compounds (n = 2,3). The energy bands for these compounds are fairly simple; see Fig. 2.10. This is in agreement with the simple power spectra we have observed for the rubidium compounds (Fig. 5.15). To obtain more quantitative agreement between the models and experimental results, it is necessary to introduce $k_z$-dispersion into the band structure via

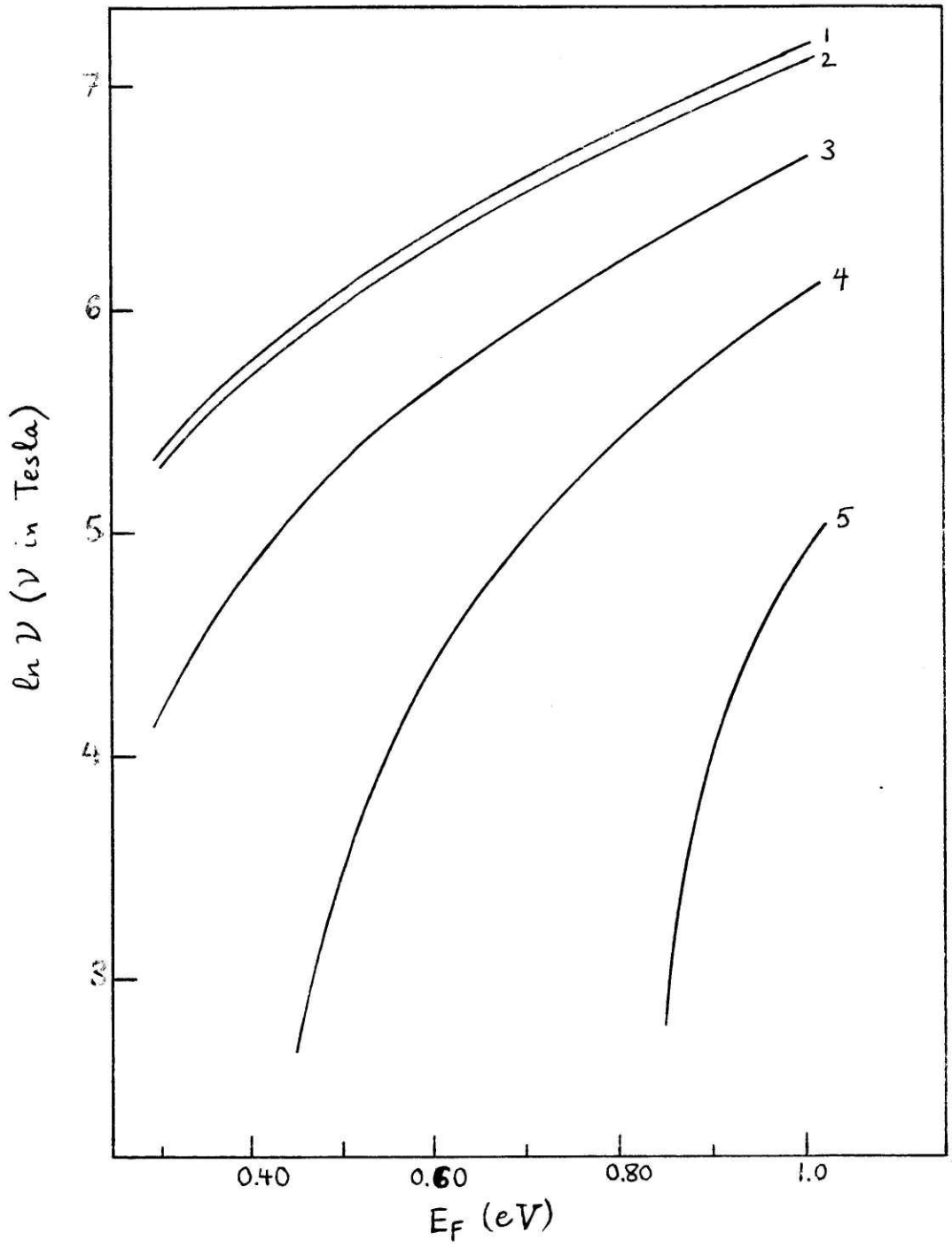


Figure 6.7

Plot of $\ell n\nu$ vs $E_F$ for the K-point FS cross sections $\nu$ of a stage-5 compound. An interaction term $\mu_o$ = -0.30eV is used to modify the bands. This figure should be compared to Fig. 6.4, which is a plot for the case $\mu_o$ = 0.

intercalate-graphite and intercalate-intercalate interactions.

Since the dominant contribution to the $k_z$-dispersion would come from the intercalate-graphite interactions, and since such interactions are relatively stage-independent, then an evaluation of model II can be done as follows. For a given intercalant, say Rb, one would apply model II to a stage 3 compound, and introduce interaction parameters to match the experimental results as accurately as possible. Then, without changing these parameters significantly the model should be applicable to a Rb-stage-4 compound and it should predict the experimental SdH results.

From an experimental viewpoint, it is harder to work with low-stage alkali-metal compounds than with those with higher stages. This is because the low-stage compounds are more unstable in the presence of oxygen and moisture. So better techniques for sample-handling and preservation will be useful in future studies. The conclusion is that more careful work, both experimental and theoretical, needs to be done on these materials, especially on the low-stage compounds, in order to obtain quantitative models for their Fermi surfaces and electronic dispersion relations.

## REFERENCES


1. Proceedings of the Franco-American Conference on Intercalation Compounds of Graphite, May 1977, La Napoule, France; also published as Mat. Sci. and Eng., vol. 31.

2. M. S. Dresselhaus and G. Dresselhaus, Advances in Physics (1981).

3. A. S. Bender and D. A. Young, Phys. Stat. Sol. B47, K95 (1971)

4. A. S. Bender and D. A. Young, J. Phys. C. Solid State Phys. 5, 2163 (1972).

5. S. Tanuma, H. Suematsu, K. Higuchi, R. Inada and Y. Onuki, Proc. of the Conference on the Application of High Magnetic Fields in Semiconductor Physics (ed. J. F. Ryan), Clarendon Press, Oxford (1978), p. 85.

6. H. Suematsu, K. Higuchi, and S. Tanuma, J. Phys. Soc. Japan 48, 1532 (1980).

7. K. Higuchi, H. Suematsu and S. Tanuam, J. Phys. Soc. Japan 48, 1541 (1980).

8. G. Dresselhaus, S. Y. Leung, M. Shayegan, and T. C. Chieu, Synthetic Metals 2, 321 (1980). Also, see Chapter V of this thesis report.

9. J. A. Woolam, E. Haugland, M. B. Dowell, N. Kambe, E. Mendez, F. Hakimi, G. Dresselhaus and M. S. Dresselhaus, Extended Abstracts of the 14th Biennial Conference on Carbon, Pennsylvania State University (1979), p. 320.

10. G. Batallan, J. Bok, I. Rosenman and J. Melin, Phys. Rev. Lett. 41, 330 (1978).

11. Y. Iye, O. Takahashi, and S. Tanuma, Solid State Commun. 33, 1071 (1980).

12. R. S. Markiewicz, H. R. Hart, L. V. Interrante and J. S. Kasper, Synthetic Metals 2, 331 (1980).

13. G. Batallan, I. Rosenman, C. Simon, G. Furdin and H. Fuzellier, Physica 99B, 411 (1980).

14. I. Rosenman, G. Batallan, and G. Furdin, Phys. Rev. B20, 2373 (1979).

15. C. Underhill, T. Krapchev, and M. S. Dresselhaus, Syn. Metals 2, 47 (1980).

References, continued

16. T. Ohno, K. Nakao and H. Kamimura, J. Phys. Soc. Japan 47, 1125 (1979).

17. N. A. W. Holzwurth, S. Rabii and L. A. Girifalco, Phys. Rev. B18, 5190 (1978).

18. T. Inoshita, K. Nakae and H. Kamimura, J. Phys. Soc. Japan 43, 1237 (1977).

19. J. C. Slonczewski and P. R. Weiss, Phys. Rev. 109, 272 (1958).

20. J. W. McClure, Phys. Rev. 108, 612 (1957).

21. J. W. McClure, Phys. Rev. 119, 606 (1960).

22. G. Dresselhaus and S. Y Leung, Solid State Commun. 35, 819 (1980).

23. C. Schafhautl, J. Prakt. Chem. 21, 129 (1841).

24. G.M.T. Foley, C. Zeller, E. R. Falardeau and F. L. Vogel, Solid State Commun. 24, 371 (1977).

25. Y. Koike, H. Suematsu, K. Higuchi and S. Tanuma, Physica 99B, 503 (1980).

26. R.W. G. Wyckoff, Crystal Structures, Interscience Publishers (1963), vol. I, p. 25.

27. The HOPG was kindly furnished by Dr. A. W. Moore of Union Carbide.

28. M. K. Halpin and G. M. Jenkins, 3rd Conf. on Ind. Carbons and Graphite, Soc. Chem. Ind., 1970, London, p. 53.

29. P. R. Wallace, Phys. Rev. 71, 622 (1947).

30. F. J. Corbato, Proc. of the 3rd Conf. on Carbon, Pergamon Press, 1959, New York, p. 173.

31. F. Bassani and G. Pastori Parravicini, Il Nuovo Cimento B50, 95 (1967).

32. G. S. Painter and D. E. Ellis, Phys. Rev. B1, 4747 (1970).

33. G. Dresselhaus and M. S. Dresselhaus, Phys. Rev. 140, A401 (1965).

34. L. G. Johnson, PhD. Thesis, Department of Electrical Eng'g. and Computer Science, M.I.T., 1973 (unpublished).

35. L. G. Johnson and G. Dresselhaus, Phys. Rev. B7, 2275 (1973).

36. E. Mendez, T. C. Chieu, N. Kambe and M. S. Dresselhaus, Solid State Commun. 33, 837 (1980).

References, continued


37. G. Dresselhaus, Phys. Rev. B10, 3602 (1974).

38. M. S. Dresselhaus, G. Dresselhaus and J. E. Fischer, Phys. Rev. B15, 3180 (1977).

39. J. Blinowski, H. H. Nguyen, C. Rigaux, J. P. Vieren, LeToullec, G. Furdin, A. Herold and J. Mellin, J. Physique 41, 47 (1980).

40. S. Y. Leung, PhD. Thesis, Dept. of Electrical Engineering and Computer Science, M.I.T., 1980 (unpublished).

41. A. H. Kahn and H. P.R. Frederikse, Solid State Phys., vol. 9 (ed. F. Seitz and D. Turnbull), Academic Press, N.Y. (1959), p. 257.

42. P. N. Argyres, J. Phys. Chem. Solids 4, 19 (1958).

43. E. M. Lifshits and A. M. Kosevich, J. Phys. Chem. Solids 4, 1(1958).

44. E. M. Lifshits, J. Phys. Chem. Solids 4, 11 (1958).

45. E.N. Adams and T.D. Holstein, J. Phys. Chem Solids 10, 254 (1959).

46. G. Landwehr, Physics of Solids in Intense Magnetic Fields (ed. E.D. Haidemenakis), Plenum Press, N.Y. (1969), pp.415-443.

47. L. Onsager, Phil. Mag. 43, 1006 (1952).

48. D.E. Nixon and G. S. Parry, J. Phys. D1, 291 (1968).

49. A. Hérold, Physics and Chemistry of Materials with Layered Structures, (ed. F. Lévy), Reidel, Dordrecht, Holland (1979), v. 6, p. 323.

50. C. Underhill, S. Y. Leung, G. Dresselhaus and M.S. Dresselhaus, Solid State Commun. 29, 769 (1979).

51. C. Underhill, T. Krapchev and M.S. Dresselhaus, Synthetic Metals 2, 47 (1980).

52. G. R. Hennig, Prog. Inorg. Chem. 1 (ed. F.A. Cotton), Interscience Publishers Inc., N.Y. (1959), p. 125.

53. B.D. Cullity, Elements of X-ray Diffraction, 2nd ed., Addison-Wesley Publ Co., Inc., Reading, MA (1978), p. 511.

54. S. Y. Leung, C. Underhill, G. Dresselhaus, T. Krapchev, R. Ogilvie and M. S. Dresselhaus, Phys. Lett. 76A, 89 (1980).

References (continued)

55. H. C. Montgomery, J. Appl. Phys. 42, 2971 (1971).

56. L. J. van der Pauw, Philips Res. Repts. 16, 187 (1961).

57. L. G. Rubin and B. Brandt, private communication.

58. D. E. Soule, J. W. McClure, and L. B. Smith, Phys. Rev. 134A, A453 (1964).

59. J. Bok, F. Batallan, and I. Rosenman, Proc. of the International Conf. on the Application of High Magnetic Fields to Semiconductor Physics (ed. J. R. Ryan), Clarendon Press, Oxford, U.K. (1978), p48.

60. O. Takahashi, Y. Iye, and S. Tanuma, Technical Report of the Institute for Solid-State Physics at the University of Tokyo, Ser. A., #1097, (1980).

61. S. Y. Leung, C. Underhill, G. Dresselhaus, T. Krapchev, R. Ogilvie and M. S. Dresselhaus, Solid State Commun. 32, 635 (1979).

62. H. Suematsu, S. Tanuma and K. Higuchi, Phsica 99B, 420 (1980).

63. N. Kambe, G. Dresselhaus and M. S. Dresselhaus, Phys. Rev. B21, 3491 (1980).

64. A. N. Berker, N. Kambe, G. Dresselhaus and M.S. Dresselhaus, Phys. Rev. Lett. 45, 1452 (1980).

65. J. M. Thomas, G. R. Millward, N. C. Davies and E. L. Evans, Dalton Trans. J. Chem. Soc. 2443 (1976).

Appendix A: THE DISCRETE FOURIER TRANSFORM (DFT) AND ZERO-PADDING

Consider a real continuous-time function f(t) and its Fourier transform [1,2]:

$$F(j\Omega) = \int_{-\infty}^{\infty} f(t)e^{-j\Omega t}\,dt \qquad (A.1)$$

as shown in Fig. A.1(a,b). Assume that f(t) is time-limited to $(t_f - t_o)$ and band-limited to $\Omega_c$. Although no continuous-time signal can be exactly time-limited and band-limited, many are approximately so. In fact, this is what we count on when we represent a signal by a finite number of its samples. Now, suppose that f(t) is sampled with a sampling period of $T_1$ [Fig. A.1(c)]:

$$x_1[n] = f(t_o + nT_1) \quad . \qquad (A.2)$$

The Fourier transform of $x_1[n]$, defined by

$$X_1(e^{j\omega}) = \sum_{n=-\infty}^{+\infty} x_1[n]e^{-j\omega n} = \frac{1}{T}\sum_{r=-\infty}^{+\infty}\left(F\, j\Omega + j\,\frac{2\pi r}{T_1}\right)\Bigg|_{\Omega = \omega/T_1} \qquad (A.3)$$

is shown in Fig. A.1(d). Note that $X_1(e^{j\omega})$ is a <u>continuous</u> periodic function of $\omega$. As can be seen from Fig. A.1(c) aliasing occurs if we are "undersampling". The largest value of $T_1$ which avoids aliasing is $\pi/\Omega_c$, the Nyquist rate.

Now when we use a digital computer to obtain the Fourier transform of a (discrete-time) signal such as $x_1[n]$, it is necessary to define the notation of the Discrete Fourier Transform (DFT). DFT is a Fourier representation for a finite-duration sequence, and is formally defined by the Fourier transform pair:

$$X[k] = \begin{cases} \sum_{n=0}^{N-1} x[n]e^{-j\frac{2\pi nk}{N}} & 0 \le k \le N-1 \\ 0 & \text{Otherwise} \end{cases} \qquad (A.4a)$$

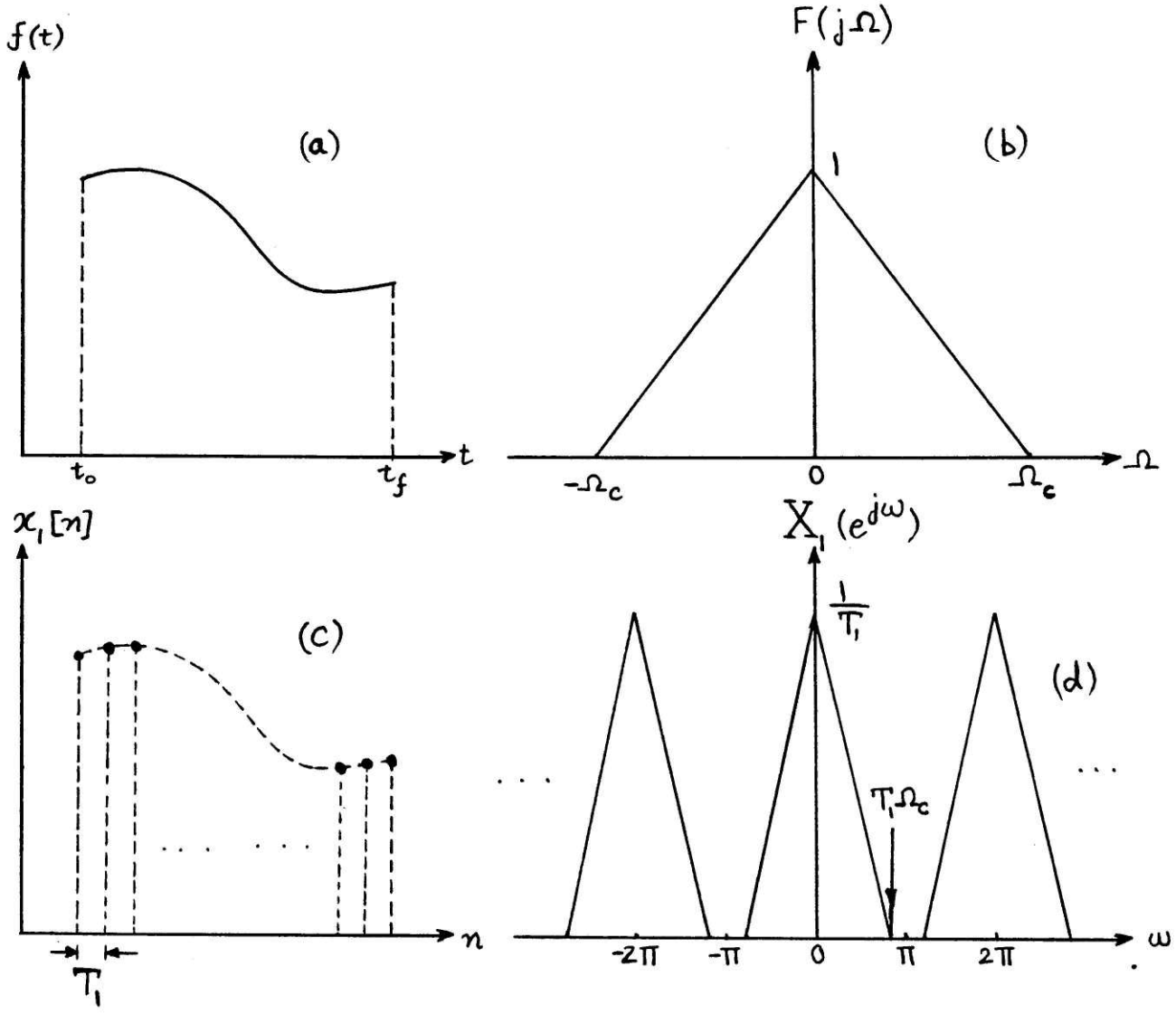


Figure A.1

(a) A real continuous-time function f(t) of finite duration; f(t) is assumed to be approximately bandlimited.

(b) Fourier transform of f(t) in (a).

(c) Sequence $x_1[n]$ whose values are samples of f(t) with a sampling period $T_1$.

(d) Fourier transform of $x_1[n]$ as defined by Eq. A.3.

$$x[n] = \begin{cases} \frac{1}{N} \sum_{k=0}^{N-1} X[k] e^{j\left(\frac{2\pi nk}{N}\right)} & 0 \leq n \leq N-1 \\ 0 & \text{Otherwise} \end{cases} \qquad \text{(A.4b)}$$

where both x[n] and X[k] are sequences of finite duration N. Equation A.4a is the analysis transform, while A.4b gives the synthesis transform. Let us assume that we have sampled f(t) at N points [Fig. A.2(a)], with a sampling period of $T_1$ to obtain the sequence $x_1[n]$. Then, the DFT of this sequence $X_1[k]$ is also an N-point sequence. Comparison of Eqs. A.4a and A.3 shows that $X_1[k]$ actually represents N equally spaced samples of $X_1(e^{j\omega})$ over one period ($-\pi < \omega \leq \pi$). This is shown in Fig. A.2(b,c). More rigorously, we have:

$$X_1[k] = X_1(e^{j\omega})\Big|_{\omega = \frac{2\pi k}{N}} \qquad k = 0, \pm 1, \pm 2, \ldots \pm\left(\frac{N}{2}-1\right), +\frac{N}{2}$$

$$= \left\{\left[\frac{1}{T} F(j\Omega)\right]_{\omega = \frac{\omega}{T_1}}\right\}_{\omega = \frac{2\pi k}{N}}$$

$$= \frac{1}{T_1} F\left(j \frac{2\pi}{NT_1} k\right) \qquad k = 0, \pm 1, \pm 2, \ldots \pm\left(\frac{N}{2}-1\right), \frac{N}{2} \qquad \text{(A.5)}$$

According to Eq. A.5, the resolution in the DFT $X_1[k]$ is:

$$\delta\Omega = \frac{2\pi}{NT_1} \cong \frac{2\pi}{t_f - t_o} \qquad \text{(A.6)}$$

Figures A.2(b,c) show that we have made inefficient use of our DFT channels (points). We have an artificially large resolution because we have left many of the DFT channels( $|k| \gtrsim \Omega_c/\delta\Omega$ ) for zero values of $X_1[k]$! Zero-padding is a method commonly used in digital signal processing to

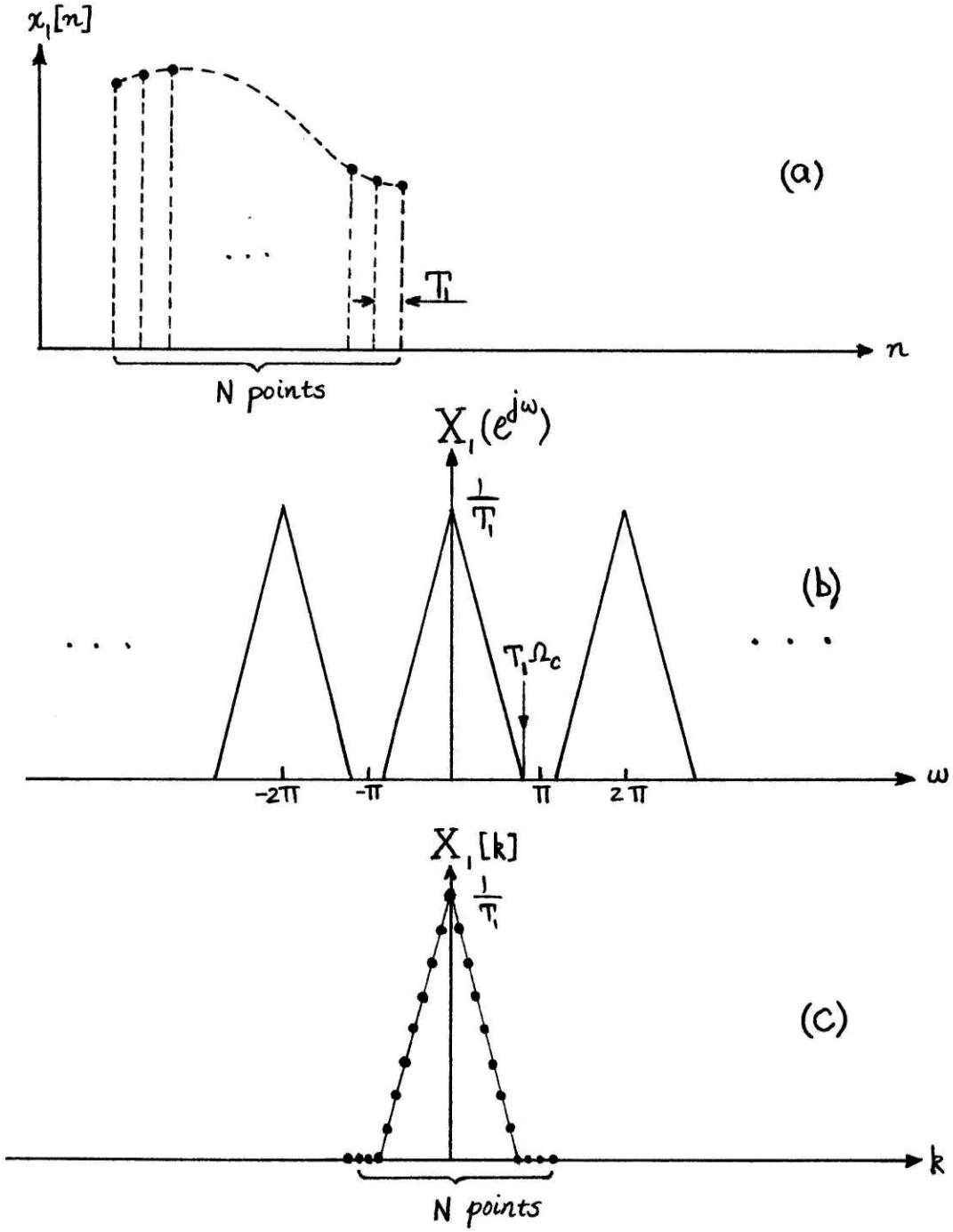


Figure A.2

(a) Sequence $x_1[n]$ representing N equally spaced samples of f(t).

(b) Fourier transform of $x_1[n]$. $T\,\Omega_c < \pi$ and we are actually 'oversampling'.

(c) DFT of $x_1[n]$. We have N equally spaced samples of $X_1(e^{j\omega})$ over one period ($-\pi < \omega < \pi$).

overcome this inefficiency [3]. Basically, what we would like to do is this. Given a fixed value of N, say 2048, we want to choose $\delta\Omega$ so that $N\delta\Omega = 2\Omega_c$, i.e., we want the non-zero values of the DFT to be spread over the entire available chanels (without aliasing). To do this, consider Fig. A.3(a). Here we have chosen a new sampling period $T_2$ equal to the Nyquist rate, i.e.,

$$T_2 = \frac{\pi}{\Omega_c} \tag{A.7}$$

Obviously, $T_2 > T_1$ and hence in less than N samples we can cover the non-zero values of f(t) ($t_o < t < t_f$). In zero-padding, we set the rest of the points in the N-point sequence equal to zero before doing the DFT, i.e., sequence $x_2[n]$ is defined as:

$$x_2[n] = \begin{cases} f(t_o + nT_2) & t_o + nT_2 \leq t_f \\ 0 & t_o + nT_2 > t_f \end{cases} \tag{A.8}$$

An evaluation of the N-point DFT of $x_2[n]$ shows that;

$$X_2[k] = \frac{1}{T_2} F\left(j \frac{2\pi}{NT_2} k\right) \qquad k = 0,\pm1,\pm2, \ldots \pm\left(\frac{N}{2}-1\right), \frac{+N}{2} \tag{A.9}$$

meaning that we have more closely spaced samples of $F(j\Omega)$ and hence a better resolution is achieved [see Figs. A.3(b,c)].

As an explicity example, let $t \triangleq X \triangleq H^{-1}$ (Chapter V) and $\Omega = 2\pi\nu$ where $\nu$ is the Shubnikov-de Haas (SdH) frequency. Consider a typical case where $\nu_{max} \cong 1000T$, $t_o = X_h = H_h^{-1} = \frac{1}{15} T^{-1}$, and $t_f = X_\ell = H_\ell^{-1} = \frac{1}{1} T^{-1}$. Then, $\delta\nu = \frac{1}{X_\ell - X_h} \cong 1.1\ T$. This is a reasonably good resolution.

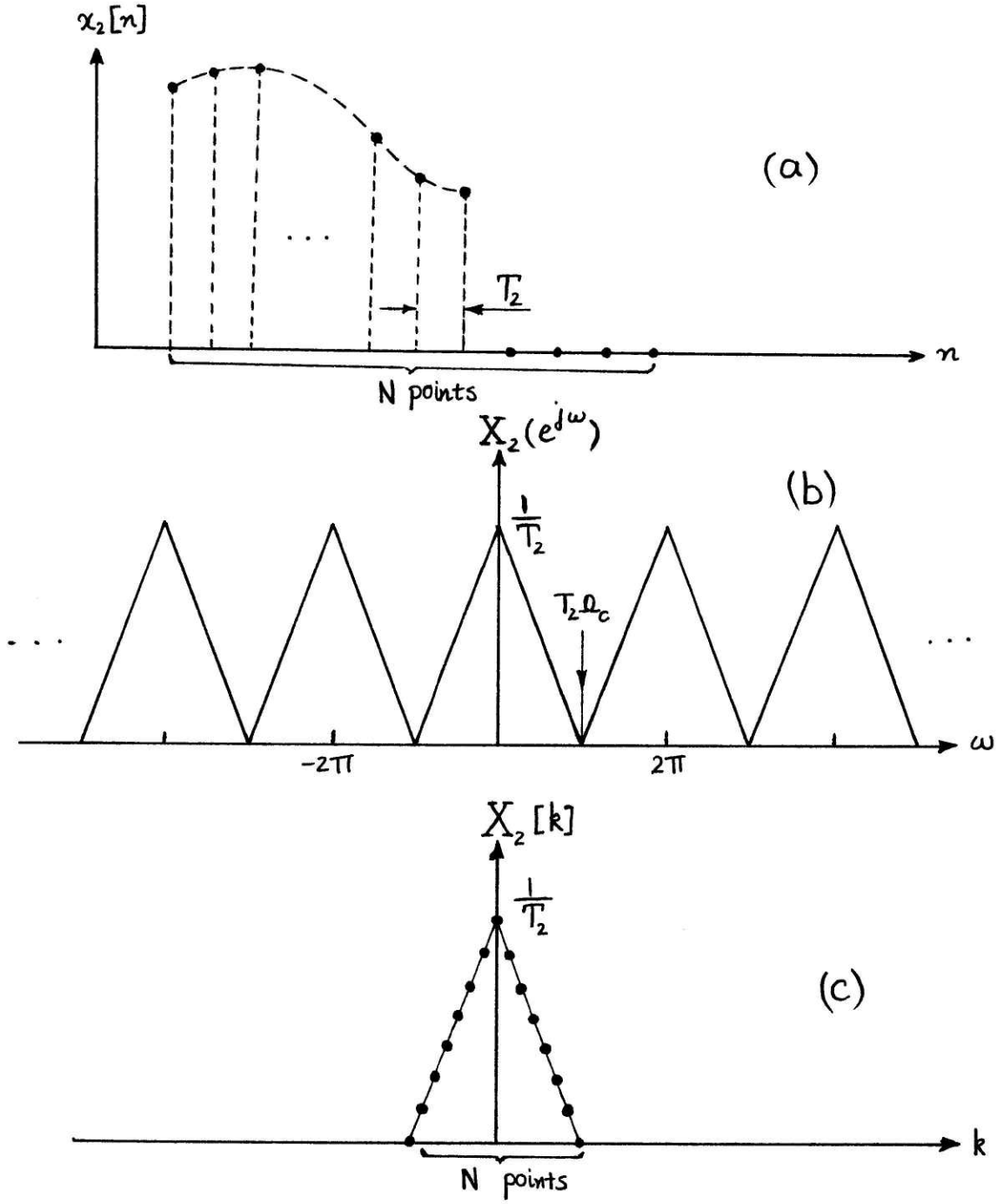


Figure A.3

(a) Sequence $x_2[n]$ representing N samples of zero-padded signal.

(b) Fourier transform of $x_2[n]$. Since we are sampling at the Nyquist rate, then $T_2\Omega_c = \pi$.

(c) DFT of $x_2[n]$. Again we have N equally spaced samples of $X_2(e^{j\omega})$ over one period ($-\pi < \omega < \pi$), but here, nonzero values of $X_2[k]$ range over the entire N channels (points) of DFT. A better resolution is obtained.

Note that, if we are taking a 2048-point DFT, no aliasing occurs, since $\nu_{max} = 1000T < \frac{N}{2}\,\delta\nu = 1097T$. Now, suppose that for some reason we would like to do a high field analysis, i.e., we want to choose our (inverse) field range as $\frac{1}{5}\,T^{-1}$ to $\frac{1}{15}\,T^{-1}$, and take a 2048-point DFT. Then, according to Eq. A.6, $\delta\nu = \frac{1}{\frac{1}{5} - \frac{1}{15}} = 7.5T$, which is not a good resolution.

But, if we zero-pad our signal from $\frac{1}{5}\,T^{-1}$ to $\frac{1}{1}\,T^{-1}$ and take 2048 uniformly spaced samples of the zero-padded signal ($\frac{1}{15}\,T^{-1}$ to $\frac{1}{1}\,T^{-1}$) we have a resolution of 1.1 T as before. Note that there is no aliasing introduced and that we have simply improved our resolution by the use of the zero-padding technique.

## REFERENCES FOR APPENDIX A


1. A. V. Oppenheim and R.W. Schafer, Digital Signal Processing, Prentice-Hall Inc., New Jersey (1975), chapters 1, 3, 5.

2. The notation used follows exactly that of Ref. [1]. Time and frequency are used as these are more familiar. Later in this Appendix, examples will be given using H-field and inverse H-field.

3. The zero-padding technique presented here follows Prof. A. V. Oppenheim's lectures and problem sets in the MIT course "Digital Signal Processing" (6.341) offered by the Department of Electrical Engineering and Computer Science.

## Appendix B: ELLIPSOIDAL FERMI SURFACE

Consider the ellipsoidal Fermi surface (FS) of Fig. 5.3(b). For such a FS, calculation based on simple geometry shows that:

$$\frac{A_o}{A_\theta} = \left(\cos^2\theta + \frac{a^2}{b^2}\sin^2\theta\right)^{1/2} \quad . \tag{B.1}$$

To determine the anisotropy ratio b/a by least-square fitting of the experimental data, we minimize:

$$F = \sum_{\theta_i}\left[\cos^2\theta_i + \frac{a^2}{b^2}\sin^2\theta_i - \frac{A_o^2}{A_{\theta_i}^2}\right]^2 \tag{B.2}$$

with respect to $a^2/b^2$, i.e., we set $\partial F/\partial(a^2/b^2) = 0$. This minimization results in:

$$\frac{a^2}{b^2} = \frac{\sum_i\left[\left(\frac{A_o}{A_{\theta_i}}\sin\theta_i\right)^2 - \cos^2\theta_i\right]}{\sum_i \sin^4\theta_i} \tag{B.3}$$

or:

$$\frac{b}{a} = \left\{\frac{\sum_i \sin^4\theta_i}{\sum_i\left[\left(\frac{A_o}{A_{\theta_i}}\sin\theta_i\right)^2 - \cos^2\theta_i\right]}\right\}^{1/2} \tag{B.4}$$

Equation B.4 is used to obtain the anisotropy ratios listed at the bottom of Table 5.1 (Chapter V).